SAMSO-TR-71-60

EFFECTS OF MASS ADDITION ON VISCOUS FLOW PARAMETERS

A. Martellucci
H. Rie

GENERAL ELECTRIC
Re-entry & Environmental Systems Division
3198 Chestnut St., Philadelphia, Pa. 19101

Security Classification

DOCUMENT CONTROL DATA - R&D

(Security classification of title, body of abstract and indexing annotation must be entered when the overall report is classified.)

1 ORIGINATING ACTIVITY (Corporate author) General Electric Re-entry and Environmental Systems Division	2a REPORT SECURITY CLASSIFICATION Unclassified 2b GROUP

3 REPORT TITLE

Effects of Mass Addition on Viscous Flow Parameters

4 DESCRIPTIVE NOTES (Type of report and inclusive dates)
Final Report Task 4.8 STREET 'G' Re-entry Aerodynamic Technology - June 1970 to Jan 1971

5 AUTHOR(S) (Last name, first name, initial)

Martellucci, A.
Rie, H.

6 REPORT DATE January 1971	7a TOTAL NO. OF PAGES 129	7b NO OF REFS 41
8a CONTRACT OR GRANT NO F04701-70-C-0179 b PROJECT NO. c d	9a ORIGINATOR'S REPORT NUMBER(S) TR-71-60 9b OTHER REPORT NO(S) (Any other numbers that may be assigned this report) GE TIS No. 71SD205	

10 AVAILABILITY/LIMITATION NOTICES
DISTRIBUTION STATEMENT "A"
Approved for public release;
distribution unlimited

11 SUPPLEMENTARY NOTES None	12 SPONSORING MILITARY ACTIVITY SAMSO

13 ABSTRACT

Boundary layer measurements on a 7.25 degree cone at Mach 8 in a Reynolds number range of 0.65×10^6 to 3.7×10^6 per foot have been analyzed and correlated. Boundary layer displacement and momentum thicknesses computed from the measured data are compared with values given by currently used empirical correlations for turbulent as well as laminar flows. An improvement to the correlations for boundary layer thicknesses in turbulent flows at zero mass addition rate is proposed. A new set of equations expressing the dependence of turbulent boundary layer thicknesses on mass addition rate is also proposed. The changes are shown to result in improved agreement between empirical predictions and flight data as well as ground test data.

DD FORM 1 JAN 64 1473

Security Classification

14 KEY WORDS	LINK A		LINK B		LINK C	
	ROLE	WT	ROLE	WT	ROLE	WT
Hypersonic Flow Boundary Layer Profiles Mass Addition Turbulent Flow Laminar Flow						

INSTRUCTIONS

1. ORIGINATING ACTIVITY. Enter the name and address of the contractor, subcontractor, grantee, Department of Defense activity or other organization *(corporate author)* issuing the report.

2a REPORT SECURITY CLASSIFICATION Enter the overall security classification of the report. Indicate whether "Restricted Data" is included. Marking is to be in accordance with appropriate security regulations.

2b GROUP. Automatic downgrading is specified in DoD Directive 5200.10 and Armed Forces Industrial Manual. Enter the group number. Also when applicable, show that optional markings have been used for Group 3 and Group 4 as authorized.

3. REPORT TITLE Enter the complete report title in all capital letters. Titles in all cases should be unclassified. If a meaningful title cannot be selected without classification, show title classification in all capitals in parenthesis immediately following the title.

4. DESCRIPTIVE NOTES. If appropriate, enter the type of report, e.g., interim, progress, summary, annual, or final. Give the inclusive dates when a specific reporting period is covered.

5. AUTHOR(S) Enter the name(s) of author(s) as shown on or in the report. Enter last name, first name, middle initial. If military, show rank and branch of service. The name of the principal author is an absolute minimum requirement.

6. REPORT DATE Enter the date of the report as day, month, year, or month, year. If more than one date appears on the report, use date of publication.

7a TOTAL NUMBER OF PAGES The total page count should follow normal pagination procedures, i.e., enter the number of pages containing information.

7b NUMBER OF REFERENCES. Enter the total number of references cited in the report.

8a CONTRACT OR GRANT NUMBER: If appropriate, enter the applicable number of the contract or grant under which the report was written.

8b, &, & 8d. PROJECT NUMBER: Enter the appropriate military department identification, such as project number, subproject number, system numbers, task number, etc.

9a. ORIGINATOR'S REPORT NUMBER(S): Enter the official report number by which the document will be identified and controlled by the originating activity. This number must be unique to this report.

9b OTHER REPORT NUMBER(S) If the report has been assigned any other report numbers *(either by the originator or by the sponsor)*, also enter this number(s).

10. AVAILABILITY/LIMITATION NOTICES: Enter any limitations on further dissemination of the report, other than those imposed by security classification, using standard statements such as:

(1) "Qualified requesters may obtain copies of this report from DDC."

(2) "Foreign announcement and dissemination of this report by DDC is not authorized."

(3) "U. S. Government agencies may obtain copies of this report directly from DDC. Other qualified DDC users shall request through _____."

(4) "U. S. military agencies may obtain copies of this report directly from DDC. Other qualified users shall request through _____."

(5) "All distribution of this report is controlled. Qualified DDC users shall request through _____."

If the report has been furnished to the Office of Technical Services, Department of Commerce, for sale to the public, indicate this fact and enter the price, if known.

11. SUPPLEMENTARY NOTES: Use for additional explanatory notes.

12. SPONSORING MILITARY ACTIVITY: Enter the name of the departmental project office or laboratory sponsoring *(paying for)* the research and development. Include address.

13 ABSTRACT: Enter an abstract giving a brief and factual summary of the document indicative of the report, even though it may also appear elsewhere in the body of the technical report. If additional space is required, a continuation sheet shall be attached.

It is highly desirable that the abstract of classified reports be unclassified. Each paragraph of the abstract shall end with an indication of the military security classification of the information in the paragraph represented as *(TS) (S) (C) or (U)*

There is no limitation on the length of the abstract. However, the suggested length is from 150 to 225 words.

14 KEY WORDS: Key words are technically meaningful terms or short phrases that characterize a report and may be used as index entries for cataloging the report. Key words must be selected so that no security classification is required. Identifiers, such as equipment model designation, trade name, military project code name, geographic location, may be used as key words but will be followed by an indication of technical context. The assignment of links, rules, and weights is optional.

FOREWORD

This report presents the results of work performed by the General Electric Re-entry and Environmental Systems Division during the second half of CY 1970 under Contract F04701-70-C-0179 which is jointly supported by SAMSO and ARPA. The work was accomplished under Task 4.8 (Reentry Aerodynamic Technology) of the STREET G Program and was monitored by Capt. R. Padfield (U.S. Air Force, SAMSO) and R. Moore (ARPA).

This report has been reviewed and is approved.

R. Padfield, Capt., USAF
Space and Missile System Organization
(SMYSE)
Air Force Systems Command
Norton Air Force Base, California

ABSTRACT

Boundary layer measurements on a 7.25 degree cone at Mach 8 in a Reynolds number range of 0.65×10^6 to 3.7×10^6 per foot have been analyzed and correlated. Boundary layer displacement and momentum thicknesses computed from the measured data are compared with values given by currently used empirical correlations for turbulent as well as laminar flows. An improvement to the correlations for boundary layer thicknesses in turbulent flows at zero mass addition rate is proposed. A new set of equations expressing the dependence of turbulent boundary layer thicknesses on mass addition rate is also proposed. The changes are shown to result in improved agreement between empirical predictions and flight data as well as ground test data.

STREET G - FINAL REPORT

LIST OF ILLUSTRATIONS

LIST OF ILLUSTRATIONS (CONT.)

LIST OF ILLUSTRATIONS (CONT.)

LIST OF TABLES

LIST OF SYMBOLS

A	area
A_b	model base area
c	Chapman-Rubesin constant: $C \equiv (\mu^* T_e)/(\mu_e T^*)$
C_D	drag coefficient
C_f	skin friction coefficient
C_F	mean skin friction coefficient: $C_F \equiv \iint_{A_s} C_f \, dA/As$
C_M	pitching moment coefficient
C_N	normal force coefficient
D_b	base diameter
h	enthalpy
H	stagnation enthalpy, also form factor: $H \equiv \delta^*/\theta$
L	model length
$\dot{m}$	mass addition rate
$\bar{\dot{m}}$	integrated mass addition rate: $\bar{\dot{m}} \equiv (\iint (\rho v)_w \, dA)/(\rho_\infty V_\infty A_b)$
M	Mach number
M_W	molecular weight
$\tilde{M}_W$	molecular weight ratio: $\tilde{M}_W \simeq (M_W)_{b.l.}/(M_W)_{inj.}$
MF	Mangler factor
n	power law velocity profile exponent
p	pressure
p_o'	pitot pressure
q	dynamic pressure, $\frac{1}{2} \rho V^2$
$\dot{q}$	heat transfer rate
r_b	radial coordinate to model surface (in cyclindrical coordinate system)
R_b	base radius

R_e	Reynolds number
R_{e_s}	Reynolds number based on wetted length
R_N	model nose radius
R_s	radial coordinate to bow shock wave (in cylindrical coordinate system)
S	wetted length
T	Temperature
$\tilde{u}$	u_L/u_e
u, v	velocity components parallel and normal to model surface
V	velocity magnitude
W	$\gamma_{inj}/\gamma_{b.l.}$
X	axial distance from cone vertex
y	normal distance from model surface
α	angle of attack
δ	boundary layer thickness
δ^*	displacement thickness
ΔX_{tr}	distance downstream of end of transition
γ	ratio of specific heats
ϵ	exponent used with profiles in Crocco coordinates (eqn. 18)
ζ	mass addition parameter: $\zeta \equiv 2\lambda/C_{f_o}$
θ	momentum thickness
θ_b	model surface inclination from axial
θ_c	value of θ_b on conic portion of model
λ	mass addition parameter: $\lambda \equiv (\rho v)_w/(\rho u)_{e_o}$
μ	dynamic viscosity

ν	kinematic viscosity
ρ	density
ϕ	meridional angle

SUBSCRIPTS

b	model base
b.l.	boundary layer
c	conic value
e	boundary layer edge
i	initial value
inj.	injectant
l	local value
L	model length
m	mean value
P	pressure contribution
r	recovery condition
s	model surface
t	stagnation condition
tr	at transition
w	model wall
0	at zero mass addition rate
∞	free stream (upstream of bow shock)

SUPERSCRIPTS

*	Eckert reference condition

SECTION I

INTRODUCTION

Despite the considerable analytic and experimental work on compressible turbulent boundary layers which has been performed in recent years, a satisfactory and general description is still lacking. The basic complexity of turbulent flow has led those seeking to describe the compressible case to hypothesize similarities between the compressible boundary layer and the constant density boundary layer, where at least a larger body of experimental measurements is available.

No attempt will be made here to review the numerous analytic investigations of compressible turbulent flow which have been made in recent years; however, mention of some recent references for background is in order. The work by Spalding and Chi[1] included a rather comprehensive review of current theoretical methods as well as a semi-empirical theory. The transformation approach developed by Coles[2] has been modified by Crocco[3] and extended and applied by Baronti and Libby[4]. Economos[5] recently developed a phenomenological treatment for solving the compressible turbulent boundary layer with mass addition which is a generalization of the work of Baronti and Libby[4].

Another approach to this complex problem is to adapt methods which have proven successful in solving the laminar boundary layer. In this approach, investigators have used an eddy viscosity concept to express the Reynolds stress terms which occur in equations governing turbulent boundary layer flow. The result is a set of equations for the turbulent boundary layer which differ from the equations governing laminar boundary layer flow solely in that molecular viscosity and Prandtl number are replaced by an "effective" viscosity and Prandtl number. If one can determine empirically what values to assign the effective viscosity and Prandtl number, it becomes possible to solve the mean characteristics of the turbulent boundary layer using well established methods for the solution of the laminar boundary layer. Eddy viscosity models for wall boundary layers have been developed by Kleinstein[6], Smith and Cebeci[7], Patankar and Spalding[8], and Sontowski[9] to name some of the more recent contributors. Each of these models was developed for the zero pressure gradient, zero mass injection case. All were shown by Martellucci, Rie, and Sontowski[10] to present reasonable agreement with data even when moderate rates of mass injection were considered. Cebeci, Smith, and Mosinkis[11] recently modified the viscosity model of Ref. 7 to include the effect of pressure gradient.

Attempts to compare the theoretical work with compressible turbulent flow experiments have been limited not only by the paucity of detailed data but also by the incomplete experimental definition of the mean profiles across the boundary layer in high speed compressible flow. This is especially true for the hypersonic case and where mass injection and other effects such as temperature jumps, which cause non similar profiles, are present.

Because of the complexity of the more rigorous analytic formulations, the numerical difficulties encountered in the solution of ablating vehicle boundary layers (due to the ablation rates, discontinuities, etc.), and the excessive computer times required to generate a solution, vehicle designers are forced to use engineering analyses which are formulated to solve the boundary layer equations. Due to the uncertainties introduced by these empirical relations, a high degree of rigor in the mathematical solution of the equation is not warranted. As a consequence, for the analysis of a turbulent boundary layer with mass injection, most authors[12-16] have utilized additional assumptions which have greatly simplified the mathematical solution of the equations. However agreement between existing theory and experimental data for a wide range of conditions is poor[17-19]. A need exists for an analysis that minimizes the dependency on the assumptions usually employed to simplify the solution of the equations, but which retains the essence of the more rigorous formulations. These engineering analyses were generated by the various aerospace companies[20-25] for the prime purpose of computing the vehicle loads and drag (which implies an accurate definition of the local properties). Since these empirical analyses were formulated, additional data have become available which can be used to validate and/or update some of the empiricism that is inherent in these methods.

The objective of the current effort is to re-evaluate the influential mechanisms of interaction between re-entry body heat shield ablation and aerodynamic parameters, based upon data obtained under the preceding STREET-G contract, other ground test data, with analytic results, and with applicable flight test data. The specific objectives of this research are to improve (1) the empirical correlations which account for mass injection effects on the viscous layer thicknesses, (2) the basic turbulent relations for predicting the viscous properties, and (3) the validity of the Crocco integral for turbulent flows with mass injection. The influence of the improved correlations on the vehicle drag for some typical flight vehicles is also ascertained.

SECTION II

EXPERIMENT DESCRIPTION

Since the primary data that are to be used in the current research were obtained and reported under the preceding STREET-G program[26], only a brief description of the test facility, the test model, and the boundary layer probes is in order.

2.1 TEST FACILITY

The test program was conducted in the Arnold Engineering Development Center (AEDC) Tunnel B at Mach 8. This facility is a continuous flow, hypersonic wind tunnel with a 50-inch diameter test section. Interchangeable axisymmetric contoured nozzles provide flow at either Mach 6 or 8. The tunnel is a closed circuit type which operates over a range of pressures with air supplied by a central compressor system. A model injection system provides the capability for quick model changes without interrupting tunnel operation. The tunnel flow conditions provide free stream Reynolds numbers from 0.30×10^6 to 3.8×10^6 per foot at Mach 8 with a maximum total temperature of $1350^\circ R$. A sketch of the tunnel layout and a summary chart of the performance characteristics of the facility are shown in Figure 1.

Model support and sting assemblies provide a 30-degree pitch range capability. A number of conventional internal strain gage balances is available at the facility to measure data in many ranges of forces and moments, and proper balance selections may be made for accuracy at small angles of attack or for a range to cover the larger angles of attack. Model support in the tunnel is positioned so that dual windows can provide complete flow visualization and photography. Each window is equipped with either a conventional single pass Schlieren system or a parallel beam refocused shadowgraph system. Model attitude in the tunnel was measured by the data readout system and verified optically with a scope in both the pitch and yaw planes. The angle of attack was maintained to within $\pm$ 0.1° for this entire investigation.

2.2 TEST MODEL

The model used in this investigations was a 7.25° half angle cone with a tangent full dome afterbody. The cone base diameter is 10.6 inches. A sketch of the model is presented in Figure 2. Three thermocouples are installed in the model one in each porous chamber. Additional pressure taps are located inside the model for use in calibration prior to the test.

The model is longitudinally divided into four separate sections. The nose section is fabricated from stainless steel. Sections one and two are fabricated from a porous sintered nickel-stainless steel alloy which is approximately 60 percent dense. The rear plate of the last conical section is adapted to accommodate the hollow compression-strut support system used for the pressure measurement phase. The last section is the impervious

tangent aft-dome. It is made of stainless steel and was spin formed. This section has cutouts in it to accommodate the legs of the strut support system. A second dome section had a hole in the center to accommodate the sting mount system, which was used for force measurements.

The internal structure of the model is fabricated to house the balance water jacket and sting arrangement to be used during the force measurement phase. The internal plumbing of the model is designed to exhaust gas into a common plenum at the rear of the model inside the last section. The gas is dispersed forward through sonic orifices into the two porous sections of the model. The mass addition rate is controlled by the plenum pressure and the distribution of the mass addition is controlled by the relative areas of the sonic orifices to the individual chambers.

The blowing or porosity uniformity of the model was established prior to the test with a venturi calibrating device. The calibration was performed with the external surface of the model at atmospheric conditions. It was performed with a conical venturi which had a twenty to one contraction ratio with a throat area of 0.05 square inches. The differential pressures between throat and plenum were recorded with a $\pm$ 1 PSID transducer. The gas samples were obtained by attaching a contoured rubber adaptor which was fitted to the cone surface. The capture area of the adaptor was roughly 0.5 square inches. The venturi was calibrated with the AEDC faciltiy reference sonic orifices. Localized mass flux readings, $(\rho v)_w$, were obtained along several rays of the model which were 45 degrees apart. The calibration indicated that the model porosity was symmetric to within $\pm$ 25%. A sample of the calibration data is given in Figure 3.

2.3 BOUNDARY LAYER PROBE

A pitot pressure and a total temperature probe were used to determine the details of the boundary layer during the course of this investigation. The probing apparatus was designed to present both probes to the flow with a separation distance of approximately 1/2 inch. The probing was performed with each probe 1/4 inch off of the vertical meridian of the model at all angles of attack. This offset was accounted for in the data tabulations and plots. The probes and their supporting structure were included 7.25 degrees to the centerline to minimize interference with the flow over the cone. The temperature probe was a singly shielded thermocouple with a diameter of 0.060 inch. The total head probe was a .040 inch diameter hyperdermic tube.

SECTION III

EFFECT OF BLOWING RATE NON-UNIFORMITIES ON BOUNDARY LAYER PROPERTIES

Prior to discussing the analysis of the data obtained with the porous cone described in Section 2, some words are in order with regard to the sensitivity of experimental data to the nonuniformities in porosity which are indigeneous to each particular model.

Aerodynamic test models fabricated from porous materials have commonly been used to simulate ablation in wind tunnel experiments. These models have been constructed from a variety of porous materials that are currently available commerically. For impulse facilities, such as AEDC tunnel F (hotshot) LTV, and at GE, thin skinned models (.030" to .060") were generally fabricated (rolled and welded) from material supplied by Union Carbide, Keendan Associates, from the Pall Corporation. For the more severe heating loads and environment imposed on models tested in the continuous flow facilities at AEDC tunnels B and C, these thin skin models are unsuitable. In these facilities, models fabricated from a porous material with a thicker wall ($\sim$.25") are necessary. Materials such as the sintered metal of Mott Metallurgical Corporation or the Foametal material of GE Metallurgical Products Division are therefore required from a thermal stress viewpoint.

Regardless of the porous material selected, the porosity distribution - that is the blowing rate distribution over the model - must be known for each experimental investigation. For all the materials, the forming process in making the bulk material into a test model creates certain nonuniformities in the blowing rate. If a porous model is to be used to investigate the boundary layer details in a turbulent mixing investigation for example, one must ascertain what nonuniformities are tolerable from a data accuracy point of view.

The purpose of this section is to demonstrate with experimental data and also with a theoretical calculation conducted with the Equilibrium Nonsimilar Boundary Layer Program (ENSBL)[27], the insensitivity of the mean boundary layer properties to the deviations from the average blowing rate.

3.1 NUMERICAL VERIFICATION

The Equilibrium Non-Similar Boundary Layer Program (ENSBL) was used to investigate the effect of the distribution of mass addition rate on the character of the boundary layer. Calculations were carried out on a sharp 7.25 degree cone for Mach number 8. It is evident (Figure 3) that the blowing distribution for this model is not constant but varies some $\pm$ 50% about the mean value, with $\pm$ 25% variations in axisymmetry.

Numerical results were computed for both the uniform and the nonuniform (sawtooth) axisymmetric blowing distributions shown in Figure 4. In one case, a uniform mass addition rate was applied over the porous portion of the cone ($0.19 \leq X/L \leq 0.90$). Outside of this range the mass addition rate was zero.

In a second case, the "sawtooth" distribution of mass addition rate was used. This distribution corresponds to a fairing of the data of Figure 3. Total mass added was the same in the two cases. Representative results are plotted in Figures 4 through 6.

Qualitatively, the displacement thickness responds as expected to the mass addition rate. Initially ($0.66 \leq X \leq 1.18$ ft.) the mass addition rate is greater in the uniform $\dot{m}$ case, as is the displacement thickness. For 1.18 ft. $\leq X \leq$ 2.24 ft. the sawtooth $\dot{m}$ exceeds the uniform value, and δ^* for the sawtooth case grows faster than for the uniform case. At $X \approx 2.59$ ft and $X > 3.14$ ft. the mass added to the boundary layer forward of that station is the same in the two cases, as is the value of displacement thickness.

Quantitatively, the response of the δ^* curves is less than proportional to the variations in mass addition. At $X \approx 1.9$ ft., where the mass addition rate for the sawtooth case is 53% greater than that of the uniform case, the difference in displacement thickness is only 6%. At $X = 2.2$, where mass added to the boundary layer in the sawtooth case is 15% greater, the difference in δ^* is only 8%.

Figures 5 and 6 present velocity and stagnation temperature profiles at $X = 2.2$ ft. (where the maximum difference in mass added occurs) and at $X = 3.065$ ft. (where total mass added in the two cases is the same). As might be expected, the difference between the two cases is greater in Figure 5. However, the differences between the two cases is insignificant*. The maximum difference in temperature profiles is less than 1%, whereas the maximum difference in velocity profiles is less than 2%.

The conclusions which can be drawn from this comparison are: because of the increased mixing characteristics in a turbulent boundary layer, a difference in the mass addition rate distribution about a mean value does not appear to significantly affect the character of the boundary layer; and that the boundary layer depends primarily on average mass addition rate, and appears to be relatively insensitive to fluctuations in the upstream history of the mass injection.

3.2 EXPERIMENTAL VERIFICATION

Force and moment data were obtained with the porous model mounted on a strain gage balance. Data were obtained for several blowing rates. If the blowing nonuniformities cause an asymmetric configuration to result, then a residual moment and normal force would appear at $\alpha = 0^\circ$. However, data obtained with this model, as shown in Figure 7, show no such influence.

It can be concluded that useful and meaningful experiments can be conducted to investigate the turbulent boundary layer characteristics of an ablating cone, simulated by blowing, with a model which exhibits blowing nonuniformities of $\pm$ 50% about the mean.

---

* It should be noted that a highly expanded temperature scale was used, i.e., only the range $0.8 \leq T_o/T_{o_\infty} \leq 1.0$ is shown.

SECTION IV

ANALYSIS AND CORRELATION OF TURBULENT BOUNDARY LAYER DATA

The experimental results obtained from the boundary layer profile measurements, which include the effects of mass injection, are presented and discussed in the following sections. The data analyzed are for both turbulent and laminar boundary layer flows, although emphasis is placed on the turbulent data. For the turbulent data, the effect of mass injection on such properties as the boundary layer thickness, displacement and momentum thicknesses, velocity profile exponent and the applicability of the Crocco theory are discussed. The data analyzed are presented in graphical form in the body of the report; tabulations of the profile properties deduced from the measured data are contained in the Appendix A. Also included in this report are the free stream and local properties (i.e. wall temperature, pressure, transition location, etc.) that are associated with the profile measurements.

4.1 DATA ANALYSIS AND PRESENTATION

The boundary layer profile data that were obtained with the porous cone shown in Fig. 2 for both the 1969 STREET-G program[26] and also for the 1968 Mark 12 Penetration Aids program[28] will be presented in this section. For convenience and clarity of presentation, the data were coded to denote the free stream environment, blowing rate and distribution, the injectant, and the state of the boundary layer at the profile measurement station. Each case is assigned a letter index which denotes the free stream condition, the average blowing rate and distribution, and the state of the boundary layer at the measured profile station (see Table I). A single letter denotes the data acquired on the 1969 STREET G Program[26]. A double letter denotes data acquired on the 1968 Mark 12 P/A effort[28]; moreover, the second letter L denotes laminar data. Each case is assigned a data symbol which will be used consistently throughout the report (see Table I). For each case surface pressure, force data, and boundary layer profile data at several stations were obtained from Reference 26. The AEDC data group numbers corresponding to each case are shown in Table 2. Average free stream test conditions for each case may be found in Table 3.

4.1.1 WALL TEMPERATURE DISTRIBUTION

The model wall temperature distributions were determined for each blowing condition, at each Reynolds number. The temperature distributions as determined from the three thermocouples located in the porous sections are shown in Figure 8. These values correspond to the equilibrium wall temperature that is achieved prior to and maintained during the acquisition of the profile data. For each Reynolds number, the wall temperature as deduced from each thermocouple correlates with the local average blowing rate, and as shown in Figure 8 is reduced as the blowing rate increases. This was also true for the non-uniform blowing cases (M and N).

4.1.2 TRANSITION ZONE DEFINITION

Measurements to deduce the state of the boundary layer were not made during the 1969 STREET-G tests, primarily because these measurements were available from the prior test entry[28]. The state of the boundary layer was determined from the impact pressures measured by traversing a pitot probe along the model surface. Data to assess the effect of mass addition on boundary layer transition were obtained for one test condition (i.e. Re_∞ /ft = 2.7 x 10^6) and are shown in Figure 9. Variation of onset and end of transition with mass addition rate were deduced from Figure 9, and are plotted (solid lines) in Figure 10. The location of the transition zone for the second test condition (i.e. Re_∞/Ft. = 3.7 x 10^6) was obtained for the non blowing case only. The $\dot{m}$ effects at the higher Reynolds number condition (dotted lines) were then scaled from the data available at the lower Reynolds number. It is apparent from the dip (near $\bar{m}$ = .01) in the data shown in Figure 10, that a slight transition reversal occurred. The initial forward movement can be attributed to the destabilizing influence of mass addition on transition. However, as the blowing rate increases, the wall temperature decreases. In this temperature range, the latter effect is stabilizing, and apparently is dominant, so that as the blowing rate increases beyond 0.01 transition moves aft. Furthermore, the data indicate that the local wetted length Reynolds number (Re_s) at the end of transition is roughly 8-9 x 10^6. In a later discussion concerning the data of Danberg[29] the above information will be used to indicate that some of the data presented therein are not turbulent but are transitional.

4.1.3 MASS ADDITION RATE DISTRIBUTION

Consistent with the calibrations performed with the porous model at AEDC, the mass addition rate distributions were scaled to conform with the basic calibration and the integrated (metered) mass rate to the model. Listed in Table 4 are the mass addition rate schedules for Cases A through N.

4.1.4 BOUNDARY LAYER PROFILE MEASUREMENTS

As indicated in Section 2.3, boundary layer profile measurements (i.e. pitot pressure and total temperature) were made at several axial stations (see Figure 2). The Rayleigh formula[30] was used to compute the Mach number from the measured pitot pressure and the static pressure which was assumed constant in the boundary layer and equal to the wall static pressure. The wall static pressure was measured by orifices in the model surface in the absence of the profile probes. The velocity in the boundary layer was computed from the local value of the Mach number and the measured total temperature. Using adiabatic relations[30] in this manner boundary layer properties such as density, temperature, and velocity which are required to compute the displacement and momentum thicknesses were defined. The displacement and momentum thicknesses were determined from the following relations:

$$\delta^* = -\frac{r_b}{\cos\theta_b} + \left[\left(\frac{r_b}{\cos\theta_b}\right)^2 + 2\int_0^\delta \left(\frac{r_b}{\cos\theta_b} + y\right)\left(1 - \frac{\rho u}{\rho_e u_e}\right) dy\right]^{1/2} \quad (1)$$

$$\theta = -\frac{r_b}{\cos\theta_b} + \left[\left(\frac{r_b}{\cos\theta_b}\right)^2 + 2\int_0^{\delta}\left(\frac{r_b}{\cos\theta_b}+y\right)\frac{\rho u}{\rho_e u_e}\left(1-\frac{u}{u_e}\right)dy\right]^{1/2} \qquad (2)$$

Inherent in the above relations are the corrections which account for transverse curvature. The boundary layer thickness was established consistently from the total temperature profile, which for the sharp cone also agrees with that obtained from the pitot pressure profile. Tabulations of the local conditions and profile parameters may be found in Appendix A. For Re_∞ /ft = 3.7×10^6 (cases A through E) the axial distribution of δ, δ^*, and θ may be found in Figures 11 through 13, and for Re_∞/ft = 2.7×10^6 (cases F through J) in Figures 14 through 16. The increase in the viscous thickness due to mass injection is rather evident from these figures. It will be shown that mass transfer increases each thickness roughly linearly with the blowing parameter $J = \frac{2}{C_{f_o}} \frac{(\rho v)_w}{(\rho u)_{e_o}}$. Also shown in these figures is the boundary layer transition zone for $\dot{m} = 0$. As noted, the forward profile station (X/L = 0.35) is in the transition zone. Also shown on these figures is the zero mass addition, all turbulent boundary layer prediction of Walker[31], as computed by VIZAAD[20]. For the sharp cone, Walker's relations are simply defined as

$$\theta = 0.037\,(MF)\,\frac{(\rho_*)^{0.8}}{\rho_e}\left(\frac{\mu^*}{u_e}\right)^{0.2} S^{0.8} \qquad (3)$$

where MF is the Mangler factor

$$\frac{\delta}{\theta} = 8 + \left(1.29\frac{h_w}{h_r}+1\right)\left(1+3.02\sqrt{\frac{H_e}{h_e}-1}\right) \qquad (4)$$

$$\frac{\delta^*}{\theta} = -1 + \left(1.29\frac{h_w}{h_r}+1\right)\left(1+2.08\sqrt{\frac{H_e}{h_e}-1}\right) \qquad (5)$$

where equations 4 and 5 are valid for Me $\geq$ 4.5. It is evident that modifications must be made to these simple engineering relations for the zero mass addition case in order to account for the influence of mass injection. This will be discussed in Section 5.1.

Turbulent boundary layer velocity profiles are customarily characterized by the power-law relation

$$\frac{u}{u_e} = \left(\frac{Y}{\delta}\right)^{\frac{1}{n}} \qquad (6)$$

The exponent, n, was obtained by measuring the slope of the velocity profile plotted on log-log paper. The axial distribution of n for Cases A to E is shown in Figure 17, and for Cases F through J in Figure 18. For the zero injection case at Re_∞ /ft = 3.7 x 10^6, the axial distribution is characterized by a value of $n \approx 9$ at the forward transitional station, an increase to some unknown value ($n \gtrsim 12$) at the end of transition, then by a decrease to values of the order of 7 at points sufficiently far removed from the end of transition. This is in concert with the study performed by Johnson and Bushnell[32] wherein a data summary concerning the power law sensitivity to Reynolds number, Mach number, and wall cooling was made (Figure 19). The Johnson-Bushnell[32] data survey indicated that the velocity exponent actually experiences an overshoot beyond the classical turbulent value of $n \approx 7$ at points immediately downstream of transition. It was postulated that n correlates with the incremental distance downstream of the end of transition normalized by the boundary layer thickness ($\Delta X_{tr}/\delta$). However, the present data do not appear to support this hypothesis. Nonetheless, values of the velocity exponent in excess of seven were experienced in the region immediately downstream of transition.

The effect of mass transfer on the turbulent velocity profile shape is to make it less full and as a result the exponent n is reduced as shown in Figures 17 and 18. A decrease of n to some 30% of its no blowing value is noted for a blowing rate $\zeta = 9$.

4.2 DATA CORRELATIONS AND COMPARISONS

To assess the influence of mass addition on the viscous layer thicknesses, the turbulent data available in Refs. 26 and 28 were presented in a form where the normalized thickness ratio (blowing value to the no blowing value) were plotted against the blowing parameter, ζ. The values of C_{f_o} and $(\rho u)_{eo}$ represent local properties at the profile station for the non-blowing case. The thickness growth with blowing for δ/δ_o, δ^*/δ^*_o and θ/θ_o are shown in Figs. 20 to 22, respectively. Also included in these figures are the turbulent flat plate data of Danberg[29] where the ζ value was corrected by the Mangler factor. Good agreement and correlation is noted for all the data. As mentioned earlier, the data presented by Danberg correspond to data obtained for two separate ranges of wetted length Reynolds number, R_{e_s}; one covering the range Re_s of 3 x 10^6 to 6 x 10^6, and the second covering the range 8.5 x 10^6 to 11 x 10^6. It is postulated, that based upon the available boundary layer transition results, that the data obtained for the lower Reynolds number range correspond to transitional boundary layer data. When these data are included in the correlation, although agreement is achieved with the mean levels of the "turbulent" data, considerably more scatter is evident. Consequently, in the correlations shown in Figs. 20 to 22 only data for $Re_s \geq 9 \times 10^6$ are included. Best fit curves were established for each of the ratio's in the form of simple algebraic relations. That is:

$$\delta/\delta_o = 1 + 0.262\,\zeta - 0.00627\,\zeta^2 \tag{7}$$

$$\delta^*/\delta^*_o = 1 + 0.333\,\zeta \tag{8}$$

$$\theta/\theta_o = 1 + 0.410\,\zeta \tag{9}$$

As a result of these curve fits, the effect of mass addition on the form factor $H \equiv \delta^*/\theta$ becomes

$$\frac{H}{H_o} = \frac{1 + 0.333\,\zeta}{1 + 0.410\,\zeta} \tag{10}$$

A comparison of this relation and the data is shown in Fig. 23. It is evident from these data that mass addition tends to lower the form factor so that at $\zeta \approx 9$, there is roughly a 15% reduction. This is in contrast to all of the existing turbulent correlations[20,21,22] which assume that blowing has no effect on the form factor (i.e. $H = H_o$).

Also shown in Figs. 20 to 22 are the curves corresponding to the current empirical prediction techniques of General Electric[20] McDonnell Douglas[22], and Philco Ford[21]. The analytic form for each of these relations is expressed below:

General Electric[20]

$$\delta/\delta_o = \frac{1}{2}\left[\frac{4+\zeta}{2+\zeta}\right]\frac{\theta}{\theta_o} \tag{11}$$

$$\delta^*/\delta^*_o = \theta/\theta_o = 1 + 0.752\,\zeta + 0.0189\,\zeta^2 \qquad (0 \le \zeta \le 6.55) \tag{12}$$

$$\delta^*/\delta^*_o = \theta/\theta_o = 0.185 + \zeta \qquad (\zeta > 6.55)$$

McDonnell Douglas[22]

$$\delta/\delta_o = \frac{1}{1 + 0.143\,\zeta}\left(\frac{\theta}{\theta_o}\right) \tag{13}$$

$$\delta^*/\delta^*_o = \theta/\theta_o = \frac{W^{0.8}\,\zeta}{(1 + W^{0.8}\,\zeta/4)^4 - 1} \tag{14}$$

where $W = \gamma_{inj}/\gamma_{b.l.}$

and γ is the ratio of specific heats

Philco Ford[34]

$$\delta^*/\delta^*_o = \theta/\theta_o = \left(\frac{T^*}{T^*_o}\right)^{-0.6}\left(\frac{C}{C_o}\right)^{0.2}\left(\zeta + \frac{C_f}{C_{f_o}}\right) \tag{15}$$

$$\frac{C_f}{C_{f_o}} = 1 + \frac{1}{2}\left(\tilde{M}_w^{0.46}\,\tilde{u}\,\zeta\right)^2 - \frac{1}{2}\left(\tilde{M}_w^{0.46}\,\tilde{u}\,\zeta\right)\left[\left(\tilde{M}_w^{0.46}\,\tilde{u}\,\zeta\right)^2 + 4\right]^{1/2}$$

where $c \equiv \frac{\mu^*}{u_e} \frac{T_e}{T^*}$ (Chapman-Rubesin Const.)

$$\tilde{M}_w = \frac{(M_w)_{b.l.}}{(M_w)_{inj}}$$

(M_w = molecular weight)

and

$$\tilde{u} \equiv \frac{u_L}{u_e} = 10.5 \left[\frac{T_w}{T_e} \frac{C_{f_o}}{2}\right]^{1/2} \quad (17)$$

It is evident from the data comparisons that each of the techniques described above overpredicts the effect of mass addition on the viscous layer thicknesses.

The effect of mass addition on the velocity profile exponent is shown in Fig. 24. It can be seen from this figure that a considerable distortion of the velocity profile results from mass addition. Furthermore, the scatter of the results suggests that parameters in addition to ζ are necessary to better correlate the data.

4.2.1 SENSITIVITY OF RESULTS TO ANGLE OF ATTACK

It is desirable to assess the sensitivity of the data used in the correlations to various sources of error, for example to the model angle of attack. This is particularly true of the results presented in Figures 20 through 24, since experimental error is magnified in obtaining ratios of two measured quantities. Although deliberate care was taken to align the model precisely with respect to the oncoming stream (i.e. $\Delta\alpha = \pm 0.1^o$) some misalignment is always present. Boundary layer profiles were obtained on the windward and leeward rays of the model at selected stations for $\alpha = \pm 1^o$ (see Ref. 26). A data reduction procedure similar to that used for the $\alpha = 0^o$ cases was used with the $\alpha = \pm 1^o$ zero mass addition data at x = 41.51 inches (that is, cross flow effects were neglected). Shown in Fig. 25 are the results of this calculation. An error of $\pm$ 2% in thickness would result for a $\pm 0.1^o$ angle of attack. However the effect of angle of attack on the velocity profile exponent is negligible, to within the accuracy of the data. Consequently the data scatter, evident in Figure 24, must be attributed to other causes.

4.2.2 COMPARISONS OF DATA WITH THE CROCCO RELATION

Theoretical and semi-empirical approaches to the solution of a turbulent boundary layer rely upon several approximations, one of which is the Crocco relation for unit Prandtl number, $\frac{H - h_w}{H_e - h_w} = u/u_e$. The bulk of available experimental data indicate that only for the adiabatic wall case does the

unit-Prandtl number Crocco relation agree with the data. In terms of the total enthalpy profile, the summary of experimental results reported by Bertram and Neal[33] indicates consistently lower values of total enthalpy in the turbulent boundary layer than the Crocco relation (see Fig. 26). Purely as an empiricism, a curve for $\frac{H - h_w}{H_e - h_w} = \left(\frac{u}{u_e}\right)^2$ also drawn in

Fig. 26, and is seen to describe much more adequately the experimental results than the classical linear Crocco relation. Included in this figure are the results of the present investigation[26]. For the present data, the absence of data at $u/u_e < .7$ is due to the difficulty of obtaining accurate measurements in the relatively thin boundary layers present on slender cones in hypersonic flows. Nonetheless, the present data for the non-blowing case agree with the data summary of Bertram and Neal[33].

The effect of blowing on the total enthalpy profile for all stations in case E may be seen in Fig. 27. In this case, due to the boundary layer thickening resulting from mass addition, data were obtained down to u/u_e = 0.27. Furthermore, the accuracy of the measurement (reduction of scatter) is also shown to increase. It is evident from this figure that for a given value of u/u_e mass injection tends to increase the total enthalpy in the boundary layer over the zero $\dot{m}$ value. A consistent trend was noted for all of the data obtained, wherein, an increase in blowing affected the level of the total enthalpy in the boundary layer (Fig. 28). Thus, if one represents the enthalpy profile by the relation

$$\frac{H - h_w}{H_e - h_w} = \left(\frac{u}{u_e}\right)^{\epsilon} \tag{18}$$

the value of ϵ (shown in Fig. 29) tends to decay with increased mass addition. It was tacitly assumed that $\epsilon = 2$ best represents the zero mass addition data.

4.3 DATA COMPARISONS WITH THEORY

Comparisons of the boundary layer thickness data with the General Electric Theories, such as the Viscous Interaction Zero Angle of Attack Drag (VIZAAD), and the Equilibrium Non Similar Boundary Layer (ENSBL) Programs, will be made in this section. The techniques employed in the current versions of each of these programs[10,27,20] are nominally equivalent to those employed industry wide and, consequently, the comparisons serve to show where deficiencies in the current state of the art exist. In addition, the implication of the recommended changes to the VIZAAD program on flight data predictions will be assessed.

4.3.1 COMPARISONS OF DATA WITH VIZAAD PROGRAM

Predictions of the viscous layer thickness as generated by the VIZAAD program were compared with data cases A through E as shown in Figs. 30 to 34.

In these VIZAAD computations, the flow was treated as laminar up to the point of transition onset. Downstream of this point, the flow was treated as turbulent. The effective origin of the turbulent solution was established by matching the zero blowing laminar momentum thickness to the zero blowing turbulent momentum thickness, that is $(\theta)_{LAMINAR} = (\theta)_{TURBULENT}$. As a consequence the values of the boundary layer thickness, δ, and the displacement thickness, δ^* are discontinuous at the transition point even for the zero mass addition case. For the cases with mass injection, all three thicknesses suffer the discontinuity since the thickness correlations differ at this point. For the cases under consideration, transition onset was sufficiently far forward so that the influence of this discontinuity on the downstream values is small. It is evident from Figure 30 that the original correlations grossly underpredict the viscous layer thicknesses. Implicit in the constant of equation 3 for computing the momentum thickness, is the assumption that the velocity profile exponent n in the entire turbulent regime is 7. For a flat plate, the origin of the constant may be found in Schlichting[34] which can be summarized as follows:

For the general case of the power law $u/u_e = (y/\delta)^{1/n}$ we have

$$\frac{\theta}{\delta} = \frac{n}{(1+n)(2+n)} \tag{19}$$

and

$$\delta = 0.0575 \left(\frac{\nu}{u_\infty}\right)^{0.2} \left[\int_0^x \frac{(1+n)(2+n)}{n}\, dx\right]^{0.8} \tag{20}$$

which for n = 7 becomes:

$$\delta = 0.37\, x \left(\frac{u_\infty x}{\nu}\right)^{-0.2} \tag{21}$$

and

$$\theta = 0.036\, x \left(\frac{u_\infty x}{\nu}\right)^{-0.2} \tag{22}$$

However, the experimental value of n is larger than the theoretical value predicted by Equation 3. This implies that n should be greater than 7, which is what the values deduced from the profiles indicate. If a functional relation n (x) were known, the constant could be revised accordingly, through the use of equation 20. However, this is not generally known. From the data of Cases A and F (that is for $\dot{m} = 0$) one can deduce that the constant in the momentum thickness relation should be increased from 0.037 to 0.059. The displacement and the boundary layer thickness will increase proportionately as is evident from equations 4 and 5. The revised relations show good agreement with the data as seen in Fig. 30.

Since the effects of mass addition on the thickness are currently being overpredicted, the existing program tends to over compensate for the poor agreement at the lower blowing rates as is evidenced by Figs. 31 to 34. The relations defining the effects of mass addition in the program (that is equations 11 and 12) were replaced by the modified relations (equations 7 through 9). Shown in Figs. 31 to 34 are comparisons of the revised program with the data. It is noted in all cases, that good agreement was achieved by all three thicknesses.

For blunt bodies, the properties at the edge of the boundary layer are determined (in VIZAAD) from the mass balance relation

$$\dot{m}_\infty = \dot{m}_{inj.} + \dot{m}_{b.l.}$$

or

$$(\rho u)_\infty \pi R_s^2 = \iint_{A_s} (\rho v)_w \, dA + 2\pi r_b (\rho u)_e (\delta - \delta^*) \qquad (23)$$

It is evident that gross modifications to the thickness values will affect this balance and accordingly will affect the local properties and consequently vehicle drag. Flight data comparisons for two classes of slender vehicles were made and some of the results are summarized below. Vehicle 1, is a small-mass-loss ablator (i.e. has a high temperature heat shield), Vehicle 2, is a large-mass-loss ablator (i.e. has a low temperature heat shield). The initial bluntness ratio for both these vehicles is $R_{N_i}/R_B = .04$.

Comparison of Revised Program with Flight Data

Vehicle No.	Altitude Kft	Vehicle Station	Parameter	Original Version of VIZAAD	Revised Version of VIZAAD	Flight Data
1 High Temp. Ablator $\dot{m}$ = .001	25	X = .5L	δ (ft)	.0264	.0288	
			δ^* (ft)	.00813	.00958	
			Me	3.50	3.97	
			$Re_s \times 10^{-6}$	12.66	16.57	
			$\dot{q}$ btu/ft^{2}sec	273.9	283.2	
		X = L	δ (ft)	.0169	.0223	
			δ^* (ft)	.00746	.0101	
			Me	5.67	6.73	
			$Re_s \times 10^{-6}$	124.5	210.6	
			$\dot{q}$ Btu/ft^{2}sec	373.	382.7	
			Total Vehicle Drag	.0724	.0743	.082
2 Low Temp. Ablator $\dot{m}$ = .049	80	X = .5L	δ (ft)	.0124	.0164	
			δ^* (ft)	.00753	.00857	
			Me	13.78	14.30	
			$Re_s \times 10^{-6}$	17.7	20.2	
			$\dot{q}$ Btu/ft^2 sec	598	579	
		X = L	δ (ft)	.0431	.0487	
			δ^* (ft)	.0320	.0287	
			Me	14.5	14.14	
			$Re_s \times 10^{-6}$	41.5	38.1	
			$\dot{q}$ Btu/ft^{2}sec	195	189	
			Total Vehicle Drag	.0600	.0570	.043

For these comparisons the local boundary layer edge properties such as the Mach number and Reynolds number show significant variations where the bluntness effects are felt. Furthermore, in all comparisons with flight data, the revised version of the program predicted drag values closer to the data irrespective of whether the predictions were lower than or higher than the flight values.

Independent of the drag comparisons, large changes in the viscous layer predictions result from the modification. It will be shown in the next section that the results of the revised VIZAAD program agree better with the more exact ENSBL program predictions.

In addition to, and more important than the effect of the thickness perturbation on local properties, is the effect this change has on plasma attenuation. Here, there is interest in transmitting at higher frequencies, which implies shorter wave lengths. These wave lengths are of the order of the boundary layer thickness and, consequently, the thickness of the layer and the shape of the profile (i.e. the local value of n) have a gross effect on the plasma behavior. Shown in Figure 35 is the S band plasma attenuation profile with altitude for a slightly blunted slender re-entry vehicle. Also shown on this figure, at altitude h, is the plasma attentuation as computed by the method of Ref. 35 for two values of the boundary layer thickness. One was deduced from Walker's original relations[31] and the second was computed from the relations as modified in this report. The profile shape was similar for the two computations. One will note that the computation is sensitive to the thickness of the boundary layer, and furthermore the comparison with data is better with the modified thickness relations.

4.3.2 COMPARISONS OF DATA WITH THE ENSBL PROGRAM

Comparisons of the ENSBL program were made with the data of Case A ($\bar{m} = 0$) and Case C ($\bar{m} = .01$). In the former comparison, three different eddy viscosity models were employed in a manner similar to that discussed in Reference 10. For the latter, comparisons of the theory with one eddy viscosity model were made with the measured thicknesses.

Shown in Fig. 36 are the results of the ENSBL calculation compared to the data of Case A. The three eddy viscosity models employed are those proposed by Smith and Cebeci[7], Patankar and Spalding[8] and by Sontowski[9]. In general the agreement of all three calculations with the measured total and displacement thicknesses is reasonable. However, one will note that the momentum thickness is underpredicted by the program irrespective of the viscosity model used. Examination of the velocity profile prediction in the physical coordinates (Fig. 37), and in the Crocco coordinates (Fig. 38) indicates that the total enthalpy in the viscous layer is being overpredicted. Of the three viscosity models, that proposed by Sontowski (which employs the lowest value of turbulent Prandtl number) most closely resembles the data (Fig. 38). However, additional modifications are required to effect acceptable agreement. The implications are that alterations to the turbulent Prandtl number, among other things, are required.

Comparisons of the ENSBL program, using Sontowski's eddy viscosity model, were made with data representing a case with mass injection as shown in Fig. 39. Once again, reasonable agreement is noted for the total and displacement thickness distributions. However, the momentum thickness is underpredicted as in the zero mass injection case. One can speculate that although mass injection increases the enthalpy in the viscous layer, the theory predicts larger values than those determined in the experiment.

SECTION V

ANALYSIS AND CORRELATION OF LAMINAR BOUNDARY LAYER DATA

The turbulent data reported in references (26) and (28) were discussed in the preceding section. Nine cases in which the boundary layer flow remained laminar (see Table 1) are also reported in Reference (28). The purpose of the present section is to compare the laminar data obtained in these cases, with currently used empirical correlations.

5.1 DATA ANALYSIS AND PRESENTATION

The boundary layer data in the laminar cases were obtained and reduced by the same methods as described in Section 4.1 for the turbulent cases. Displacement and momentum thicknesses were computed using equations (1) and (2). For this laminar data, they, as well as boundary layer thickness , δ , are plotted versus axial position in Figures 40 through 42.

To show their dependence on mass addition rate, the ratios δ / δ_o, δ^* / δ_o^* and θ / θ_o are plotted vs ζ (Figures 43 through 45). Although cases QL and SL provided data for values of ζ near 30.0, too few points were available at these high mass addition rates to warrant presentation. Figures 40 through 45, were, therefore, limited to $\zeta \leq 3.0$. As might be expected, the data show a general thickening of the boundary layer with an increase in mass addition rate.

5.2 DATA COMPARISONS WITH CURRENT THEORY

Laminar thickness predictions of Walker[36] as computed in VIZAAD[20] are compared with experimental values in Figures 40 through 42. Walker's relations for laminar flow are:

$$\delta = \frac{5.3\, s}{MF \sqrt{Re_s}\ (h^*/h_e)^{0.18}} \left[\frac{\mu^*/\mu_e}{\rho^*/\rho_e}\right]^{1/2} \tag{24}$$

and

$$\frac{\delta^*}{\delta} = \frac{u_e^2/2h_e + 3.36\ h_w/h_e - 0.376}{u_e^2/2h_e + 3.36\ h_w/h_e + 5.79} \tag{25}$$

and θ is obtained from an integration of the following equation, which is the result of combining the integral momentum and continuity equations:

$$\frac{d}{ds}\left(\rho_e u_e^2 \theta\right) = \frac{C_f}{2} + \lambda - \frac{\delta^*}{u_e}\ \frac{du_e}{ds} + \delta \left[\frac{1}{u_e}\ \frac{du_e}{ds} + \frac{1}{\rho_e u_e^2}\ \frac{dP}{ds}\right] \tag{26}$$

The value of C_f, which is required in equation (26), is obtained (in the absence of mass addition) through the Reynolds analogy from Lee's relations for heat transfer rate, modified by the reference enthalpy method[20]:

$$\dot{q} = \frac{0.354\, \rho^* \mu^*\, u_e\, r_b\, (h_r - h_w)}{P_r^{2/3} \left[\int_0^s \rho^* \mu^*\, u_e\, r_b\, dS \right]^{1/2}} \qquad (27)$$

At the higher of the two Reynolds numbers for which laminar data were available ($Re_\infty = 2.7 \times 10^6$/ft), equations (24) and (25) consistently overpredict δ and δ^* (Figure 40). At the lower Reynolds number (0.67×10^6/ft) no consistent trend can be observed. Nor can one deduce any trend when comparing the momentum thickness given by equation (26) with values computed from measured data.

Because of the limited amount of experimental data available, no attempt is made to suggest improvements to the laminar correlations.

The effect of mass addition on momentum thickness is computed in VIZAAD by first solving equation (26) for the zero mass addition case; then repeating the solution for ϑ, inserting the appropriate of $(\rho v)_w$ in equation (26). The appropriate value of C_f for use in this solution is obtained from the relation (see Section 6):

$$\frac{C_f}{C_{fo}} = \frac{1}{1 + 0.663\, \zeta} \qquad (28)$$

The dependence of δ and δ^* on mass addition rate is deduced from the approximation:

$$\frac{\delta}{\delta_o} = \frac{\delta^*}{\delta^*_o} = \frac{\theta}{\theta_o} \qquad (29)$$

The VIZAAD results are compared with test data in Figures 43 through 45 (solid lines). The method introduces a dependence on bluntness ratio. Agreement with measured data appears to be better for the sharp cone than for $R_N/R_B = 0.077$.

The dependence on mass addition rate is introduced by McDonnell-Douglas[22] through the following relations:

$$\frac{\delta}{\delta_o} = \frac{\delta^*}{\delta^*_o} = \frac{\theta}{\theta_o} = \frac{C_f}{C_{fo}} + \zeta \qquad (30)$$

where

$$\frac{C_f}{C_{fc}} = 1 + 0.68\, W^{0.4}\, \zeta + 0.08\, W^{0.4}\, \zeta^2 \qquad (31)$$

and $$W = \gamma_{inj.} / \gamma_{b.l.}$$

In the present case the value of the ratio W was unity. Agreement with test data is good for the mass addition rates shown.

SECTION VI

SKIN FRICTION REDUCTION CORRELATION - LAMINAR FLOW

Sufficient data to assess the effect of mass injection on the skin friction reduction were not obtained in the experimental investigations[26,28] discussed in the body of this report. However, the laminar force data of Ref. 24 in conjunction with the large body of data of King[37] provide a suitable basis for reassessing the correlations which currently exist. Since the skin friction was not measured directly in the experiments, it was obtained indirectly by calculation as follows

$$C_{D_f} = C_{D_{TOTAL}} - \left[C_{D_p} + C_{D_b} + C_{D_{inj.}} \right] \tag{32}$$

All drag coefficients are referenced to the cone base area. The total drag is the experimental value registered by the drag balance.

The pressure drag is defined as the streamwise component of force due to the slant-face pressure in excess of free stream pressure. This can be expressed as:

$$C_{D_p} = \frac{D_p}{1/2\, \rho_\infty u_\infty^2 A_b} = \frac{2\pi \tan^2 \theta_b}{1/2\, \rho_\infty u_\infty^2 A_b} \int_0^L (P-P_\infty)\, x\, dx \tag{33}$$

The pressure, p, referred to here is the experimentally determined value.

The base drag corresponds to that which occurred in the experiment as a result of a particular method of mounting the models in the wind tunnel, and consequently has no significance beyond that of an experimental correction. Because the pressure existing on the base and inside the hollow afterbody was different from P_∞, a net force occurred on the model. The base drag coefficient can then be expressed as

$$C_{D_b} = - \frac{(P_b - P_\infty) A_b}{1/2\, \rho_\infty u_\infty^2 A_b} \tag{34}$$

The negative sign is inserted because pressure on the base actually produces a thrust on the model.

The passage of injected gas from the model surface into the boundary layer produces a drag force increment which is small, but not negligible. If we assume the validity of the no-slip boundary condition, then the injection velocity must be normal to the cone surface. The injection drag coefficient component may be computed from the flux of momentum across the porous surface as

$$C_{D_{inj.}} = \frac{\iint_A (\rho v)_w^2 / \rho_w) \sin \theta_b \, dA_s}{1/2 \, \rho_\infty \, u_\infty^2 \, A_b} \qquad (35)$$

It is evident that the correction becomes more important at the higher injection rates, amounting to roughly 5% of the total drag at $\zeta \approx 3.0$.

With the friction drag computed from equation (32), in conjunction with equations (33) to (35) the total skin friction coefficient C_F can then be evaluated from the following relation:

$$C_F = C_{D_f} \frac{A_b}{A_s \cos \theta_b} \frac{q_\infty}{q_e} \qquad (36)$$

or

$$C_F = C_{D_f} \frac{\tan \theta_b}{\left[1 - (\ell/L)^2\right]} \frac{q_\infty}{q_e}$$

where

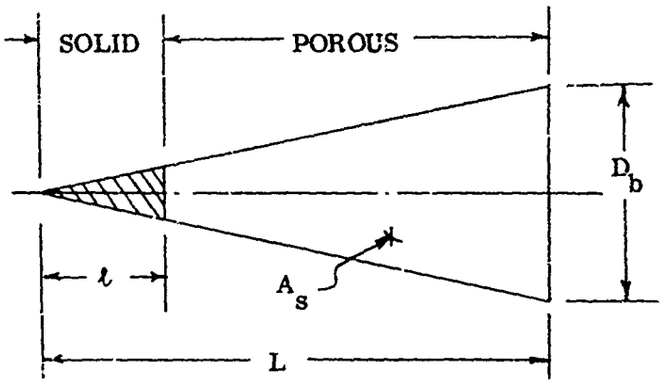

Although the skin friction coefficient as deduced from equation (36) corresponds to the total skin friction of the cone, C_F, the use of the data thereafter in correlation form are treated on a local basis, Cf (x), where

$$C_F = \frac{\iint_{A_s} C_f \, dA_s}{A_s} \qquad (37)$$

Shown in Figure 46 are the data of King[37] plotted versus the blowing parameter, ζ . Data were obtained for two values of the free stream Mach number (i.e. M_∞ = 3.93 and 5.64 or M_e = 3.75, 5.29) and for two injectant gases (i.e. Helium and air). The data for air injection show no apparent effect of free stream Mach number as is evident in the Helium data. In addition, it appears that Helium is not as effective as air in reducing the drag, which is in agreement with the conclusions of Little and Griffith[38]. Also shown in Figure 46 is the data summary of Leadon et al[39] Kent, et al[28] and some unpublished GE data. The experimental results have been empirically curve-fitted using the equation for C_f/C_{f_o} derived in Dorrance[40], where

$$\frac{C_f}{C_{fo}} = \frac{\zeta}{e^{K\zeta} - 1} \tag{38}$$

expanding and retaining only linear terms in ζ , there results:

$$\frac{C_f}{C_{fo}} = \frac{1}{1 + K\zeta} \tag{39}$$

where K is the empirical constant that achieves a best fit with the data. It was concluded that

$$\frac{C_f}{C_{fo}} = \frac{1}{1 + 0.663\zeta} \tag{40}$$

is a "best-fit" as shown in Figure 46.

The empirical techniques of Timmer et al[22] and Costello[41] are also shown in Fig. 46. It is evident that both of these methods tend to under-predict the skin friction drag of an ablating vehicle.

SUMMARY AND CONCLUSIONS

Measurements of pitot pressure and stagnation temperature profiles as well as surface pressures and temperatures obtained at AEDC under 1969 STREET-G and 1968 Mark 12 P/A contracts have been reduced and correlated. Values of boundary layer thickness, displacement and momentum thicknesses, form factor, profile exponents n and ϵ, and location of boundary layer transition have been deduced for turbulent boundary layers. In addition, the first three of these parameters have been deduced in several cases where boundary layer flow remained laminar.

The data treated in this study was obtained on a 7.25 degree sphere cone with bluntness ratios of zero, 0.077 and 0.180. Free stream Mach number was 8.0 and Reynolds number ranged from 0.65×10^6 to 3.7×10^6 per foot. Integrated mass addition ratio varied from zero to 0.05.

Results deduced from experiment are compared with empirical prediction methods used at General Electric, McDonnell-Douglas and Philco Ford. All three methods appear to overpredict the effect of mass addition on boundary layer thickness in turbulent flow. A new set of equations, accounting for the effect of mass addition on δ, δ^*, and θ is proposed for turbulent boundary layers. In addition, a correction is proposed to a constant used with the GE thickness predictions at zero mass addition. The proposed changes result in an improved drag and plasma attenuation prediction for flight vehicles.

In laminar boundary layers, currently used correlations appear adequate at low mass addition rates. The quantity of available measured data was not adequate to permit an evaluation of currently used correlations at high mass addition rates.

In several turbulent cases measurements were compared with results computed with the GE Equilibrium Non-Similar Boundary Layer Program (ENSBL), a finite difference solution of the boundary layer equations. Three eddy viscosity models were used with ENSBL, and results computed with each are presented. Good agreement is noted in δ and δ^*, but θ is slightly underpredicted by ENSBL.

REFERENCES

1. Spalding, D. B. and Chi, S. W., "The Drag of A Compressible Turbulent Boundary Layer on a Smooth Flat Plate with and without Heat Transfer", Journal of Fluid Mechanics, Vol. 18, Part I, 1964, pp. 117-143.
2. Coles, D. E., "The Turbulent Boundary Layer in a Compressible Fluid", RAND Corp. Rept. R-403-PR, September 1962.
3. Crocco, L., "Transformation of the Compressible Turbulent Boundary Layer with Heat Exchange", AIAA Journal, Vol. 1, No. 12, December 1963, pp. 2723-2731.
4. Baronti, P. O., and Libby, P. A., "Velocity Profiles in Turbulent Compressible Boundary Layers", AIAA Journal, Vol. 4, No. 2, February 1966, pp. 193-202.
5. Economos, C., "A Transformation Theory for the Compressible Turbulent Boundary Layer with Mass Transfer" AIAA Journal, Vol. 8, No. 4, April 1970, pp. 758-764.
6. Kleinstein, G., Generalized Law of the Wall and Eddy-Viscosity Model for Wall Boundary Layers" AIAA Journal Vol. 5, No. 8 August 1967, pp. 1402-1407.
7. Smith, A. M. O., and Cebeci, T., "Numerical Solution of the Turbulent Boundary Layer Equations", Douglas Aircraft Division Report 33735 (May 1967), ASTIA AD656430.
8. Patankar, S. V., and Spalding, D. B., Heat and Mass Transfer in Boundary Layers, Morgan-Grampian, London (1967).
9. Sontowski, J. F., "An Eddy Viscosity Model for Compressible Turbulent Boundary Layers", GE RS TIS 69SD241 (1969).
10. Martellucci, A., Rie, H., Sontowski, J. F., "Evaluation of Several Eddy Viscosity Models Through Comparison with Measurements in Hypersonic Flows" AIAA Paper No. 69-688, June ,1969.
11. Cebeci, T., Smith, A. M. O., Mosinskis, G., "Recent Progress in the Calculation of Turbulent Boundary Layers" Douglas Paper 5531, May, 1969.
12. Dorrance, W. H., and Dore, F. J., "The Effect of Mass Transfer on the Compressible Turbulent Boundary Layer Skin-Friction and Heat Transfer", JAS, June 1954.
13. Rubesin, M. W., "An Analytical Estimation of the Effect of Transpiration Cooling on the Heat-Transfer and Skin-Friction Characteristics of a Compressible Turbulent Boundary Layer", NACA TN 3341, December 1954.
14. Rubesin, M. W., and Pappas, C. C., "An Analysis of the Turbulent Boundary Layer Characteristics on a Flat Plate with Distributed Light-Gas Injection", NACA TN 4149, February 1958.
15. Ness, N., "Distributed Injection of Air into a High-Temperature, Equilibrium Air, Turbulent Boundary Layer", G.E. MSVD AOTM #141, August 1959.
16. Ness, N., "Foreign Gas Injection into a Compressible Turbulent Boundary Layer on a Flat Plate", G. E. TIS #R60SD410, August 1960.
17. Pappas, C. C., "Effect on Injection of Foreign Gases on the Skin-Friction and Heat-Transfer of the Turbulent Boundary Layer", IAS Report No. 59-78, January 1959.
18. Studerus, C. J., "Comparison of Theoretical and Experimental Induced Pressure Skin Friction Reduction and Zero Lift Total Drag for a Pointed 7.5^{o} Porous Cone in Presence of Turbulent Mass Transfer" GE-TIS No. 65SD325, April, 1965.

19. Martellucci, A., Neff, R. S., Rittenhouse, C., "Mass Additon Effects on Vehicle Forces and Moments - Comparison Between Theory and Experiment", SAMSO TR 69-384, September 1969.
20. Studerus, C. J., Dienna, E. A., "Viscous Interaction Zero Angle of Attack Drag (VIZAAD) Programa", GE TIS 64SD292, November 1964 (U).
21. Grabow, R. M., "Hypersonic Drag Coefficients for Cones with Mass Transfer and Bluntness Effects", Philco-Ford Report No. METN 112, January 1967 (U).
22. Timmer, H. G., Arne, C. L., Stokes, T. R., Jr., Tang, H. H., "Ablation Aerodynamics for Slender Re-entry Bodies Vol. I Theoretical Analyses and Results", McDonnell Douglas Astronautics Co., AFFDL-TR-70-27, March 1970.
23. Kohrs, R., Pannabecker, C., Patay, S., Wells, D., "The Determination of Hypersonic Drag Coefficients for Cones, Biconics, and Triconics", AVCO Report No. AVMSD-0136-67-CR March, 1967 (U).
24. Chrusciel, G. T., Hull, L. D., "Theoretical Method for Calculating Aerodynamic Characteristics of Spherically Blunted Cones", Lockheed TM 55-21-168, May 1968 (U).
25. Chrusciel, G. T., "Summary of Techniques for Viscous Drag Predictions", Lockheed TM 81-11/11 (U).
26. Martellucci, A., "Static Force, Surface Pressure, and Profile Measurements on a Porous Cone with Gas Injection Data Presentation", SAMSO TR-70-152, January, 1970.
27. Levine, J. N., "Finite Difference Solution of the Laminar Boundary Layer Equations Including the Effects of Transverse Curvature, Vorticity, and Displacement Thickness" GE TIS 66SD349, Dec. 1966 (Also presented as AIAA paper 68-739).
28. Kent, R., Martellucci, A., and George, F. C., "Static Force and Pressure Measurements on a Slender Porous Cone with Gas Injection", GE/RESD, ALDM 69-75, February, 1969.
29. Danberg, J. E., "Characteristics of the Turbulent Boundary Layer with Heat and Mass Transfer at M = 6.7", NOLTR 64-99 (Aerodynamics Research Report No. 228) Oct. 1964.
30. Ames Research Staff "Equations, Tables, and Charts for Compressible Flow", NACA TR 1135, 1953.
31. Walker, G. K., and Schumann, B. A., "The Growth of Turbulent Boundary Layers", GE-RESD R61SD123, July, 1961.
32. Johnson, C. B., Bushnell, D. M., "Power-Law Velocity Profile - Exponent Variations with Reynolds Number, Wall Cooling, and Mach Number in a Turbulent Boundary Layer" NASA TND-5753, April, 1970.
33. Bertram, M. H., and Neal L., Jr., "Recent Experiments in Hypersonic Turbulent Boundary Layers", NASA TMX-56335, May 1965.
34. Schlicting, H., "Boundary Layer Theory", McGraw Hill Book Co. Inc. New York, N.Y. Pgs. 432, 1955.
35. Scherer, P. M., "Antenna Performance Analysis in a Re-entry Plasma Sheath", GE-RESD TM 9143-1, December, 1970.

36. Walker, G. K., "The Growth of Laminar Boundary Layers with ZeroPressure Gradient", GE-RSD, TFM-8151-008, January 1963.
37. King, H. H., "Hypersonic Flow over a Slender Cone with Gas Injection" Univ. of Calif. Berkeley Technical Report HE-150-205, Nov. 1962.
38. Little, H. R., Griffith, B. J., "Mass Injection Studies on Slender Cones and a Flat Plate with Trailing Edge Ramp at Mach Numbers from 9 to 21" AEDC-TR-67-109, August 1967.
39. Leadon, J. et al, "Mass Transfer Cooling of a 20° Porous Cone at M = 5" University of Minnesota Rosemont Aerodynamics Lab., Research Report No. 143, July 1957.
40. Dorrance, W. H., "Viscous Hypersonic Flow McGraw Hill Book Co. Inc. New York, N. Y. Pgs 59 FF, 1962.
41. Costello, F. A., "Mass Transfer Cooling-Laminar Flat Plate Boundary Layer" GE-RESD TFM No. 012, May, 1963.

TABLE 1. KEY FOR BOUNDARY LAYER PROFILE DATA

A. TURBULENT

Sym.	Source			Model	M_∞	M_e	Re_∞/Ft. x 10^{-6}	$\frac{\dot{m}}{(\rho v)_\infty A_b}$	$\dot{m}(x)$	Injectant
	Ref.	Author	Case							
○ □ △ ◇ ◇	26	Martellucci	A B C D E	Cone	8	6.78	3.7	0 0.005 0.010 0.025 0.050	Uni-form	N_2
○ □ △ ◇	26	Martellucci	F G H J	Cone	8	6.78	2.7	0 0.005 0.010 0.025	Uni-form	N_2
○ ○	26	Martellucci	M N	Cone	8	6.78	2.7	0.010 0.025	Non-uni-form	N_2
★ ★ ★	28	Kent, Martellucci, George	BB CC EE	Cone	8	6.78	3.7	0.005 0.010 0.050	Uni-form	CO_2
◐ ■ ◆	28	Kent, Martellucci, George	FF GG KK	Cone	8	6.78	2.7	0 0.005 0.050	Uni-form	N_2
●	29	Danberg	-	F.P.	6.7	6.7	-	-	Uni-form	Air

B. LAMINAR

Sym.	Source			Model	M_∞	R_N/R_B	Re_∞/Ft. x 10^{-6}	$\dot{m}/(\rho v)_\infty A_b$	$\dot{m}(x)$	Injectant
	Ref.	Author	Case							
◐ ◐	28	Kent, Martellucci, George	PL QL	Cone	8	0.077	2.7	0 0.050	Uni-form	N_2
◐ ◐			RL SL			0.180		0 0.050		
■ ▲	28	Kent, Martellucci, George	TL UL	Cone	8	0	0.65	0.005 0.010	Uni-form	N_2
◐ ■ ▲			VL WL XL			0.077		0 0.005 0.010		

TABLE 2

DATA SUMMARY (REF. 26)
($\alpha = 0^{o}$)

Case	Code	Group No.	Re_{∞} /Ft x 10^{-6}	$\bar{m}$	$\dot{m}(x)$	Profile Sta. x (inches)	Data Acquired
	A0	33	3.7	0	-	-	Surface Pressure
	A1	3				-	Force
A	A2	58				41.51	Profiles
	A3	96				36.61	"
	A4	101				30.61	"
	A5	102				21.61	"
	A6	107				14.61	"
	B0	68	3.7	.005	1111	-	Surface Pressure
	B1	7				-	Force
	B2	59				41.51	Profiles
B	B3	97				36.61	"
	B4	100				30.61	"
	B5	103				21.61	"
	B6	106				14.61	"
	C0	61	3.7	.010	1111	-	Surface Pressure
	C1	6				-	Force
C	C2	60				41.51	Profiles
	C3	98				36.61	"
	C4	99				30.61	"
	C5	104				21.61	"
	C6	105				14.61	"
	D0	31	3.7	.025	1111	-	Surface Pressure
	D1	5				-	Force
D	D2	108				41.51	Profiles
	D3	111				36.61	"
	D4	112				30.61	"
	E0	27	3.7	.050	1111	-	Surface Pressure
	E1	4				-	Force
E	E2	109				41.51	Profiles
	E3	110				36.61	"
	E4	113				30.61	"
	F0	21	2.7	0	-	-	Surface Pressure
	F1	1				-	Force
F	F2	34				41.51	Profiles
	F3	38				36.61	"
	F4	40				30.61	"
	F5	44				21.61	"

TABLE 2 (Cont.)

Case	Code	Group No.	R_{e_∞}/Ft x 10^{-6}	$\bar{\dot{m}}$	$\dot{m}(x)$	Profile Sta. x (inches)	Data Acquired
G	G0	6	2.7	.005	1111	-	Surface Pressure
	G1	10				-	Force
	G2	35				41.51	Profiles
	G3	-				-	
	G4	41				30.61	"
H	H0	11	2.7	.010	1111	-	Surface Pressure
	H1	9				-	Force
	H2	36				41.51	Profiles
	H3	39				36.61	"
	H4	42				30.61	"
	H5	45				21.61	"
J	J0	16	2.7	.025	1111	-	Surface Pressure
	J1	8				-	Force
	J2	37				41.51	Profiles
	J3	-				-	"
	J4	43				30.61	"
K	K0	22	2.7	.050	1111	-	Surface Pressure
	K1	2				-	Force
L	L0	69	2.7	.005	1133	-	Surface Pressure
	L1	11				-	Force
	L2	85				41.51	Profiles
M	M0	74	2.7	.010	1133	-	Surface Pressure
	M1	12				-	
	M2	86				41.51	Surface Pressure
	M3	87				36.61	Force
	M4	88				30.61	Profiles
	M5	91				21.61	"
N	N0	82	2.7	.025	1133	-	Surface Pressure
	N1	13				-	Force
	N2	89				41.51	Profiles
	N3	-				-	
	N4	90				30.61	"

Table 3

Free Stream Conditions

$M_\infty = 8.0$

Case	$R_{e\infty} \times 10^{-6}$ per foot	Po psia	T_o °R	P_∞ psia	ρ_∞ lbs/ft^3	T_∞ °R	V_∞ FPS	$\bar{\dot{m}} = \frac{\dot{m}_{TOT}}{(\rho v)_\infty A_B}$
A	3.69	849	1346	.0870	.002408	97.54	3871.4	0
B	3.70	850	1346	.0872	.00242	97.3	3865.0	.0050
C	3.72	851	1337	.0872	.00242	97.2	3858.4	.0091
D	3.70	851	1344	.0871	.00242	97.4	3869.0	.0247
E	3.71	851	1344	.0872	.00242	97.4	3870.0	.049
F	2.74	600	1303	.062	.00176	94.7	3810.0	0
G	2.74	598	1301	.062	.00176	94.49	3805.8	.0043
H	2.75	601	1304	.062	.00177	94.71	3810.2	.0091
J	2.76	602	1300	.062	.00178	94.4	3804.0	.025
M	2.74	602	1308	.0622	.00177	95.0	3816.0	.0090
N	2.73	600	1308	.062	.00176	95.1	3818.0	.0249
No β profiles K	2.74	600	1306	.062	.00176	94.9	3813.0	.051
No β profiles L	2.76	599	1302	.062	.00177	94.57	3807.3	.0042

Table 4

Mass Addition Rate Schedule

X/L	Cases A	B	C	D	E	F	G	Cases H	J	M	N
	Mass Addition Rates $(\rho v)_w$ #/Ft^{2}Sec										
0	0	0	0	0	0	0	0	0	0	0	0
.19		0	0	0	0		0	0	0	0	0
.19		.00458	.00843	.02226	.0443		.00277	.00609	.0166	.00315	.00860
.545		.00814	.0150	.0401	.0787		.00493	.0108	.0295	.00561	.0153
.545		.00927	.0171	.0457	.0897		.00561	.0123	.0336	.00639	.0174
.747		.00283	.0052	.0139	.0273		.00171	.00376	.0102	.00195	.00531
.747		.00871	.0160	.0429	.0842		.00527	.0016	.0315	.0182	.0491
.905		.00339	.00625	.0167	.0328		.00205	.00451	.0123	.00708	.0191
.905		.00808	.0149	.0398	.0782		.00489	.0108	.0293	.0169	.0456
1.00		.00345	.00635	.0170	.0334		.00209	.00459	.0125	.00720	.0194
Average Values $(\rho v)_w$ Fwd	0	.00608	.0112	.0300	.0588	0	.00368	.00809	.0220	.00419	.0114
Average Values (ρv) Aft	0	.00608	.0112	.0300	.0588	0	.00368	.00809	.0220	.0127	.0343
$\dot{m}$	0	.0050	.0091	.0247	.049	0	.0043	.0091	.0250	.0090	.049

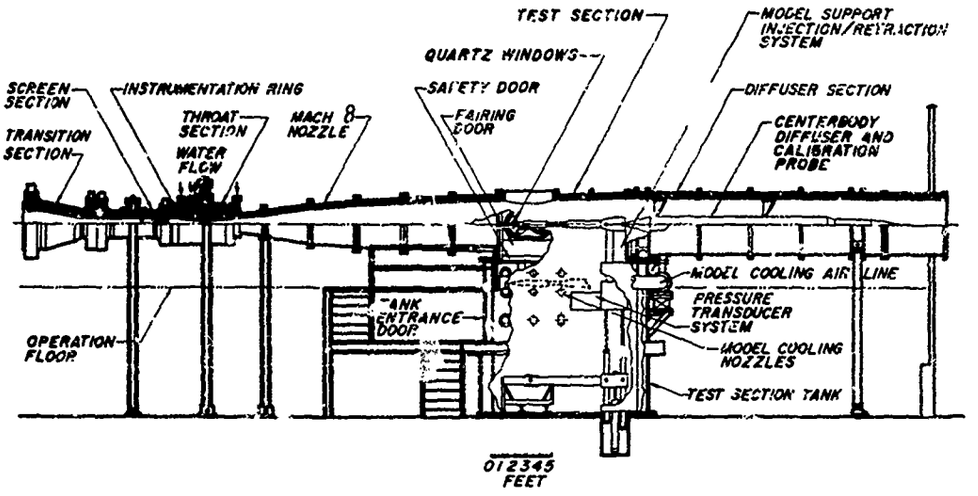

a. Tunnel Assembly

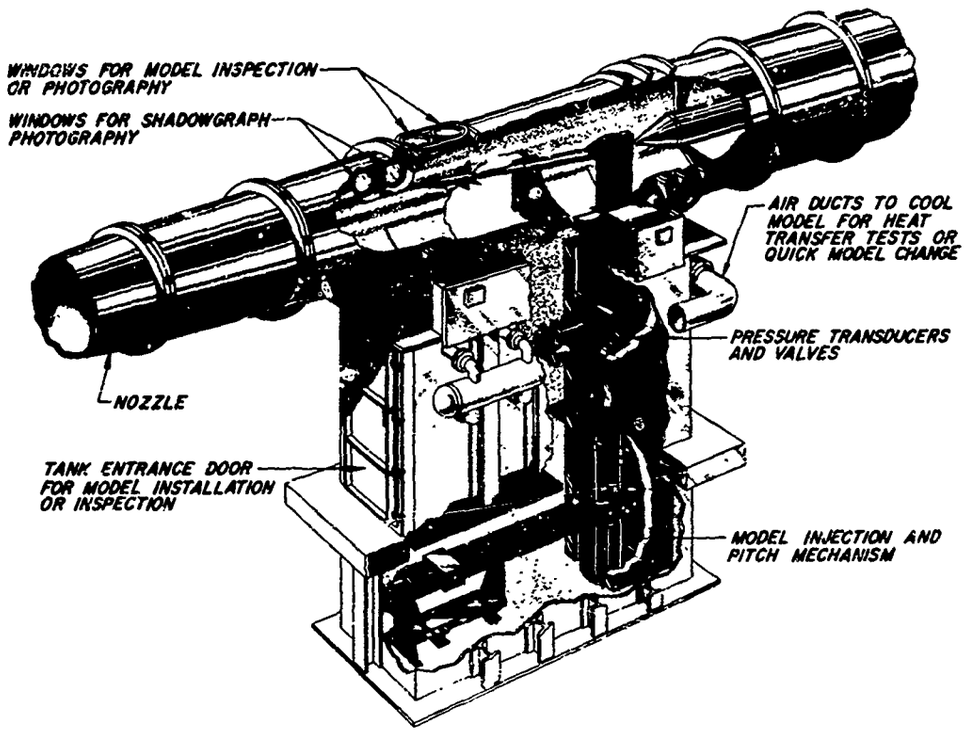

b. Tunnel Test Section

TUNNEL PERFORMANCE								
Tunnel	Nominal Mach Number	P_o (Psia)		T_o (^oR)	q (Psia)		Re/ft. $x10^{-6}$	
		Min	Max	Max	Min	Max	Min	Max
B	6	20	300	1350	0.3	4.6	0.3	5.3
	8	50	900	1350	0.3	4.1	0.3	3.8

Figure 1. Tunnel Layout and Performance Characteristics

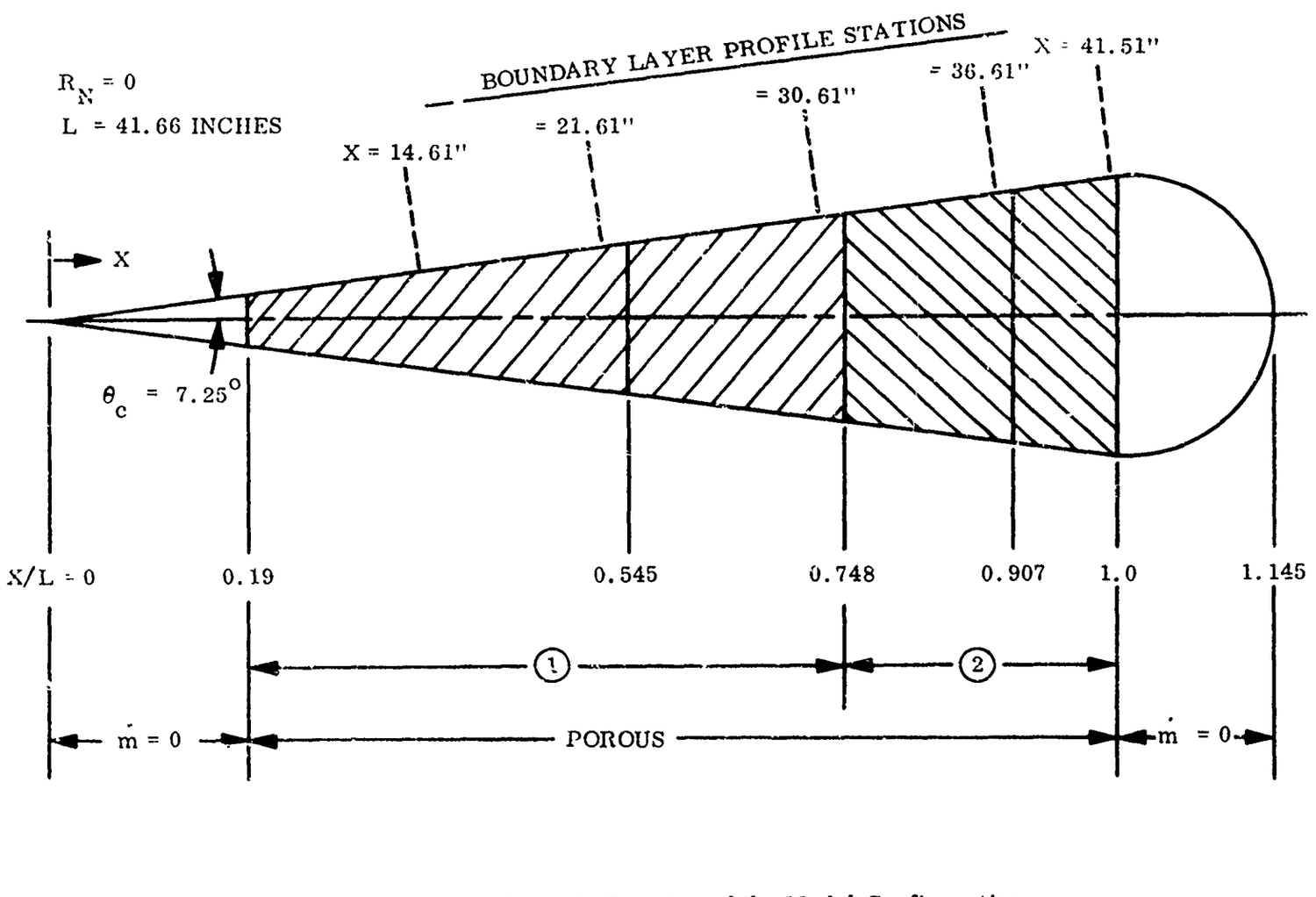

Figure 2. Schematic Drawing of the Model Configuration

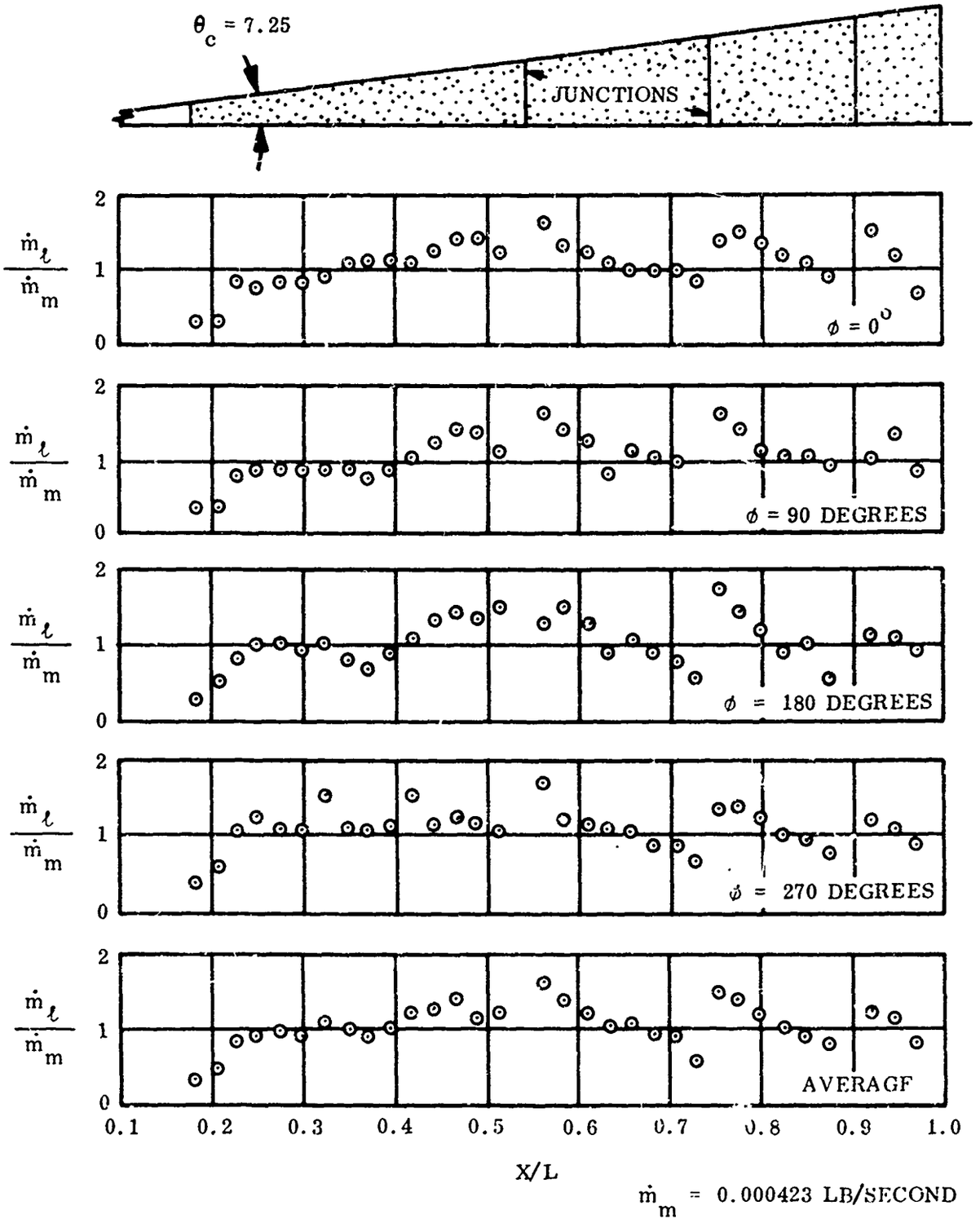

Figure 3. Surveys of the Local Mass Flow Rates - Axial Variation

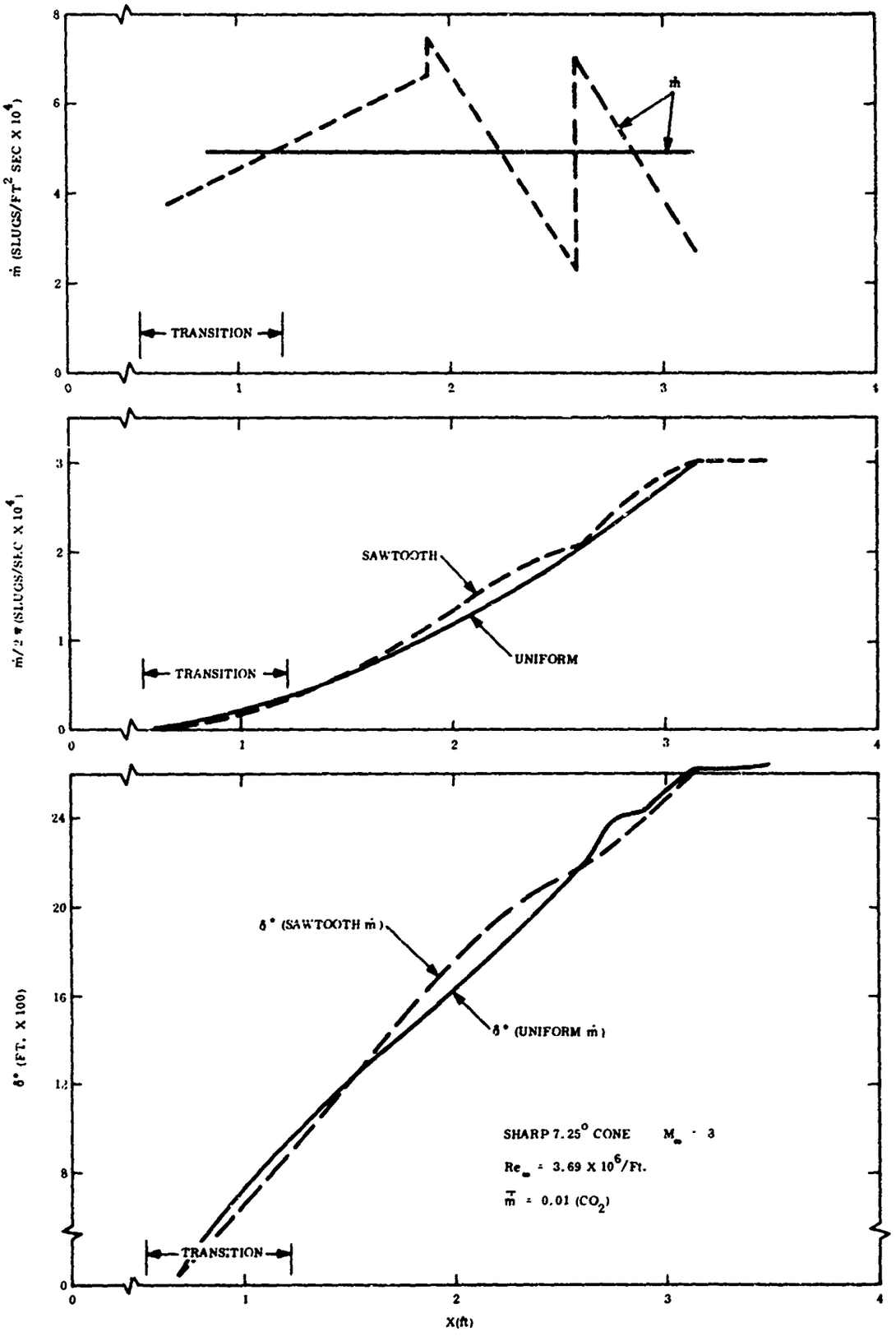

Figure 4. Displacement Thickness and Mass Addition Rate (ENSBL Calculation)

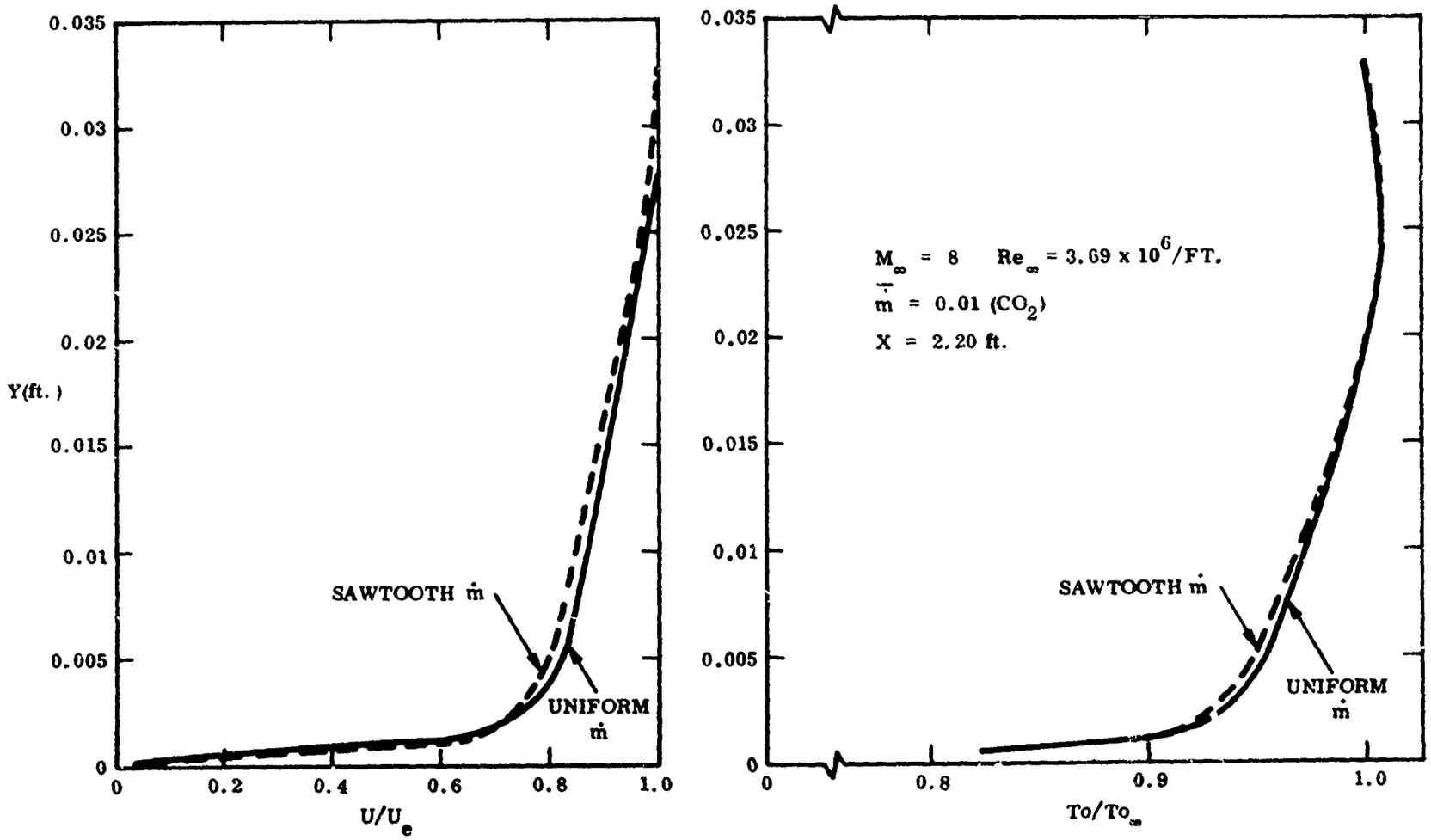

Figure 5. Profile Comparison at Station Where Difference in ṁ Rate is Greatest (ENSBL Calculation)

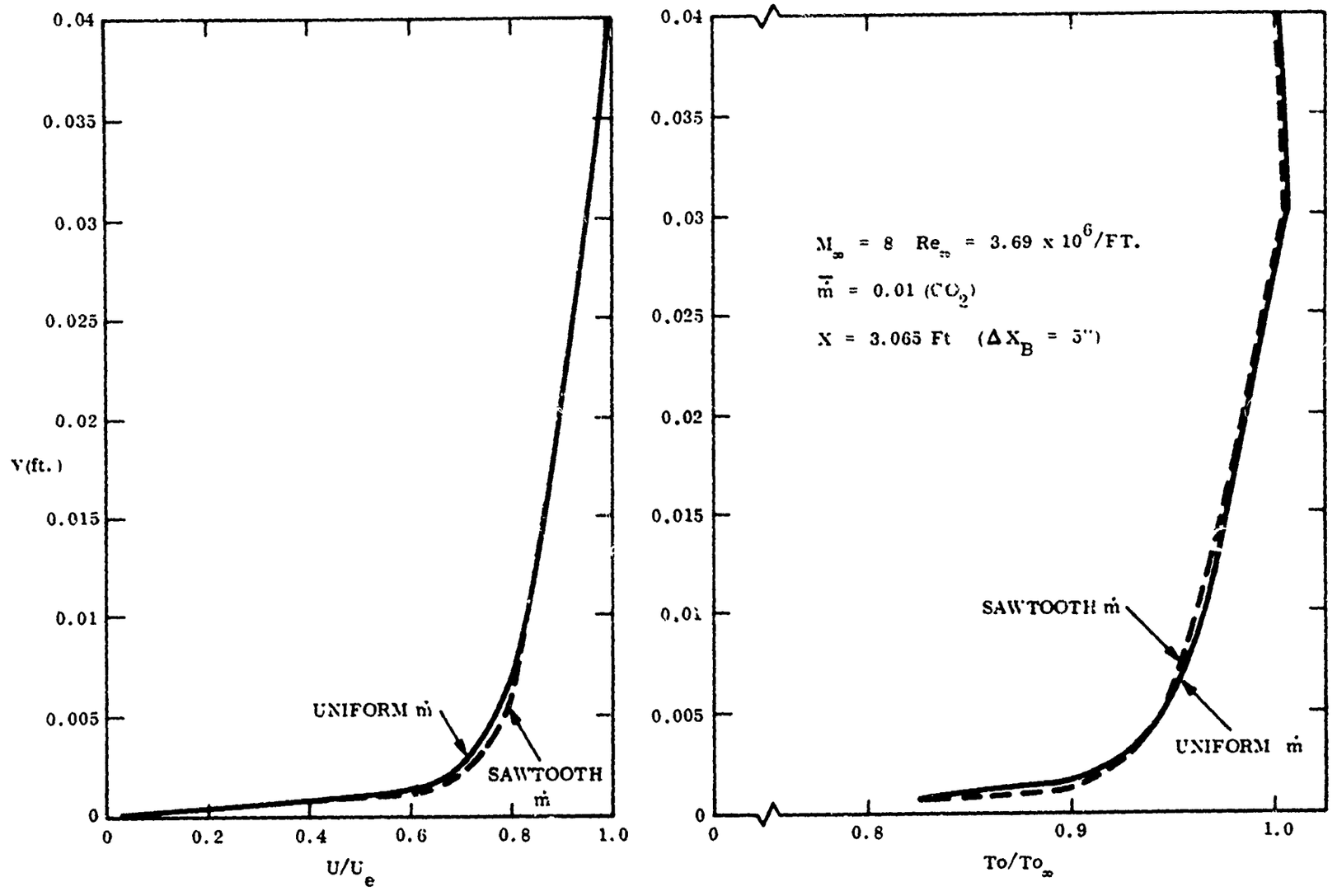

Figure 6. Profile Comparison at a Station Where Total Mass Added is Identical (ENSBL Calculation)

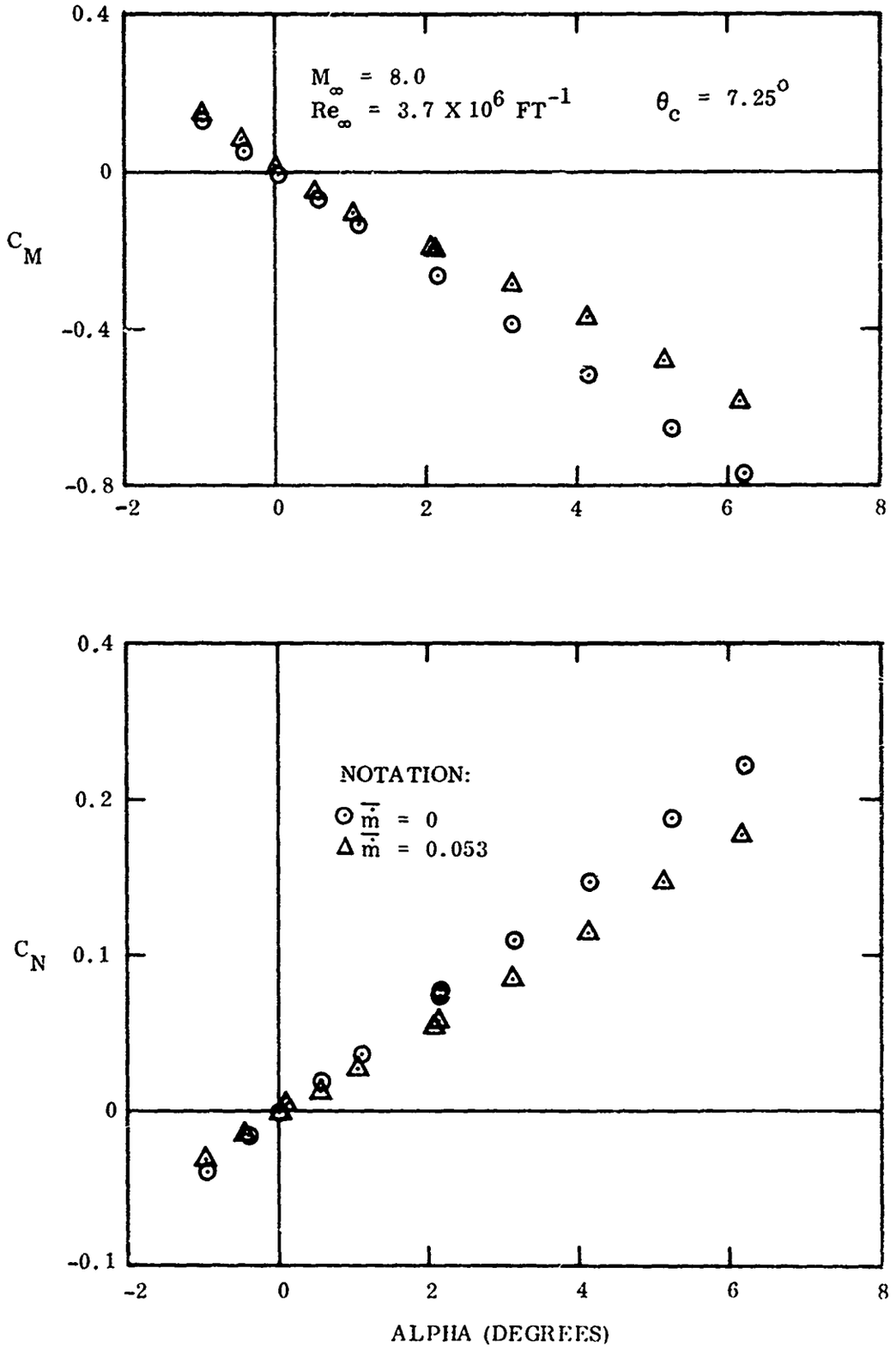

Figure 7. Pitching Moment and Normal Force Coefficients

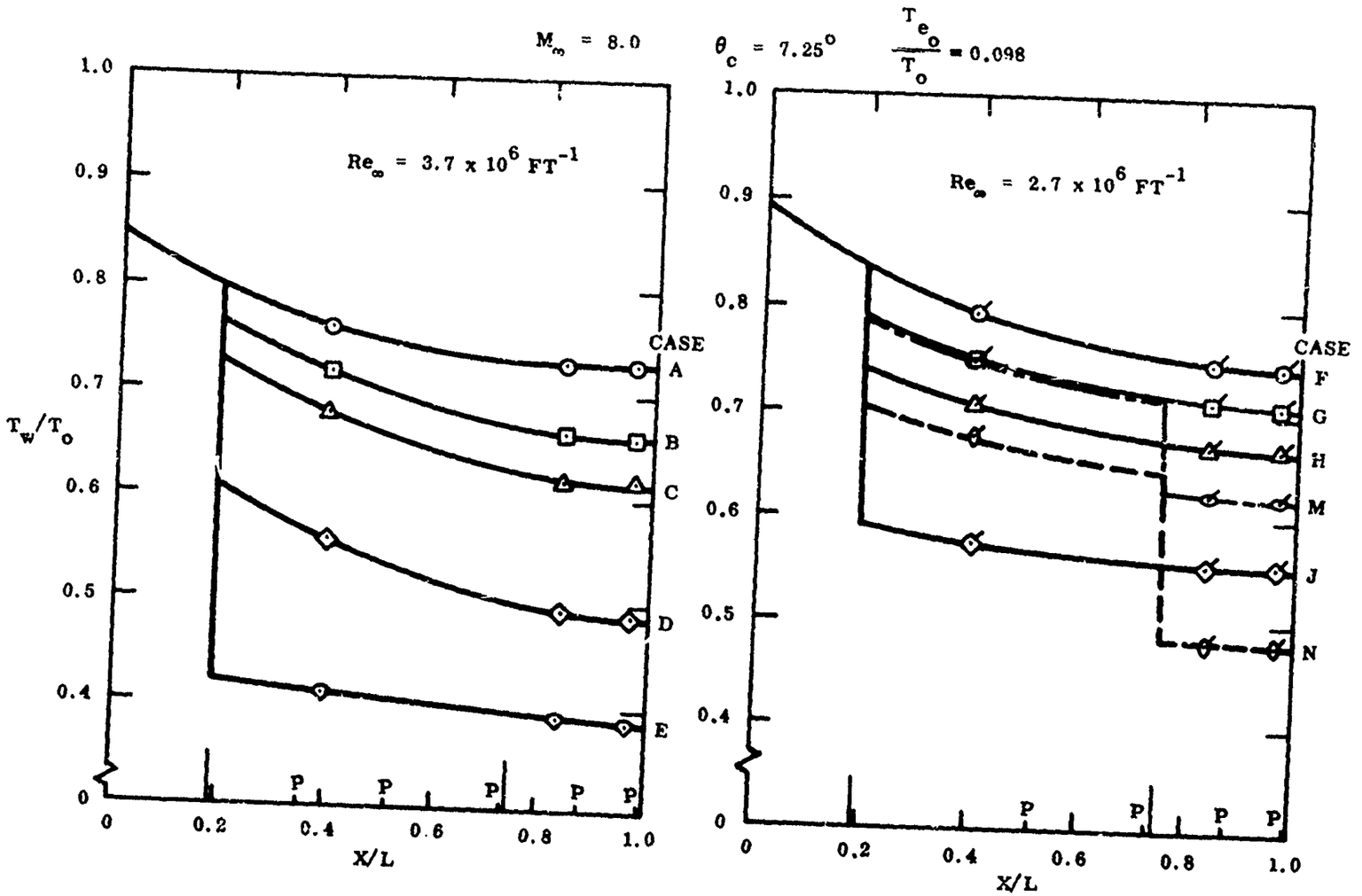

Figure 8. Wall Temperature Distribution

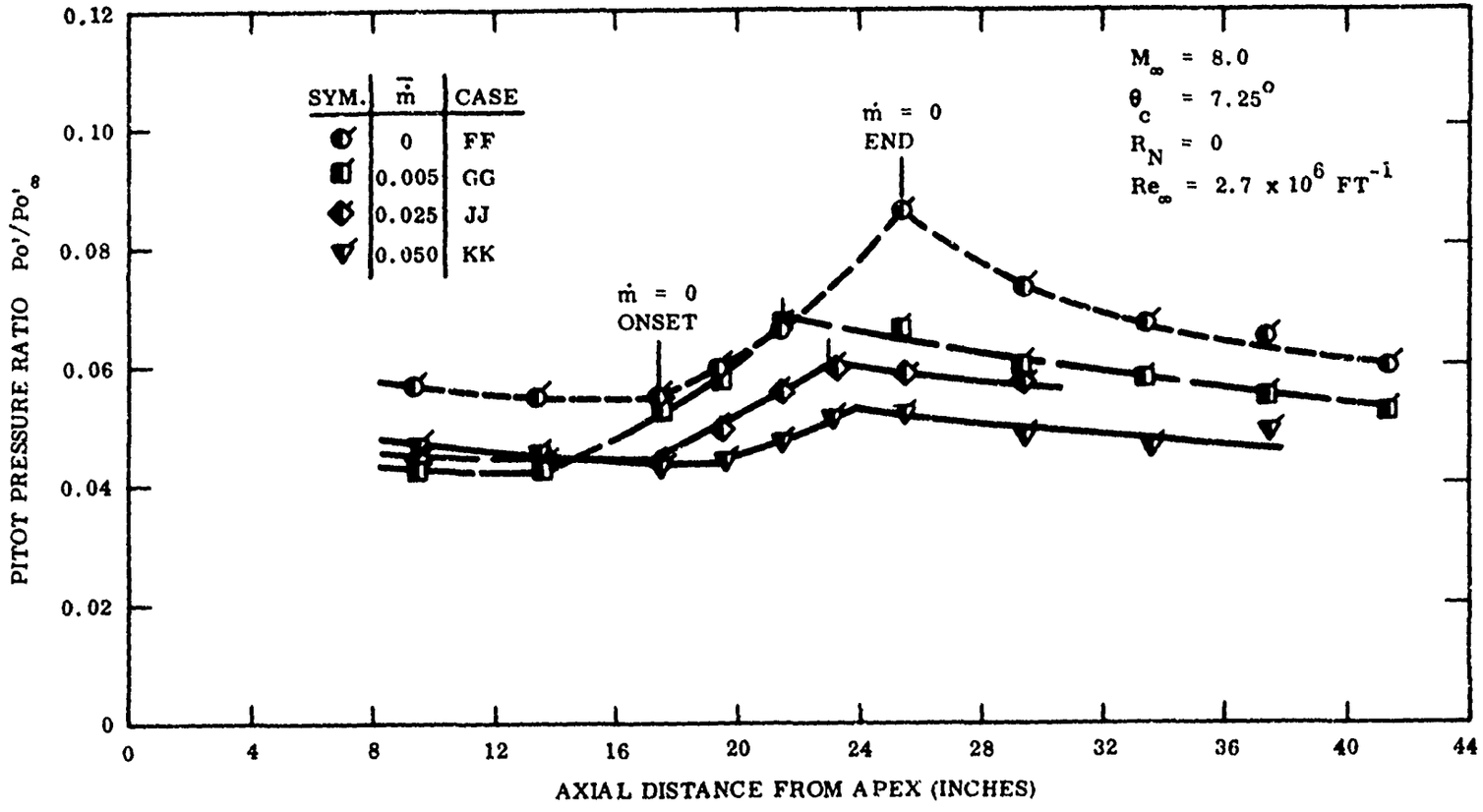

Figure 9. Transition Detection from Pitot Pressure Survey on Model Surface

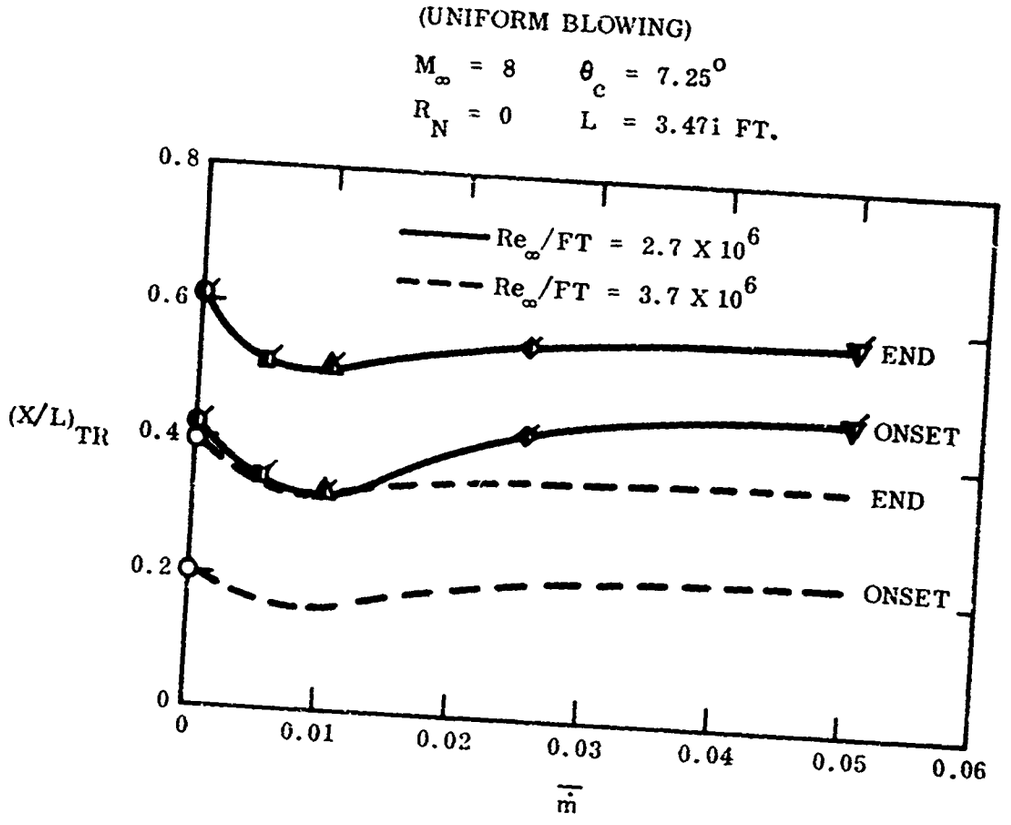

Figure 10. Transition Location vs Mass Addition Rate

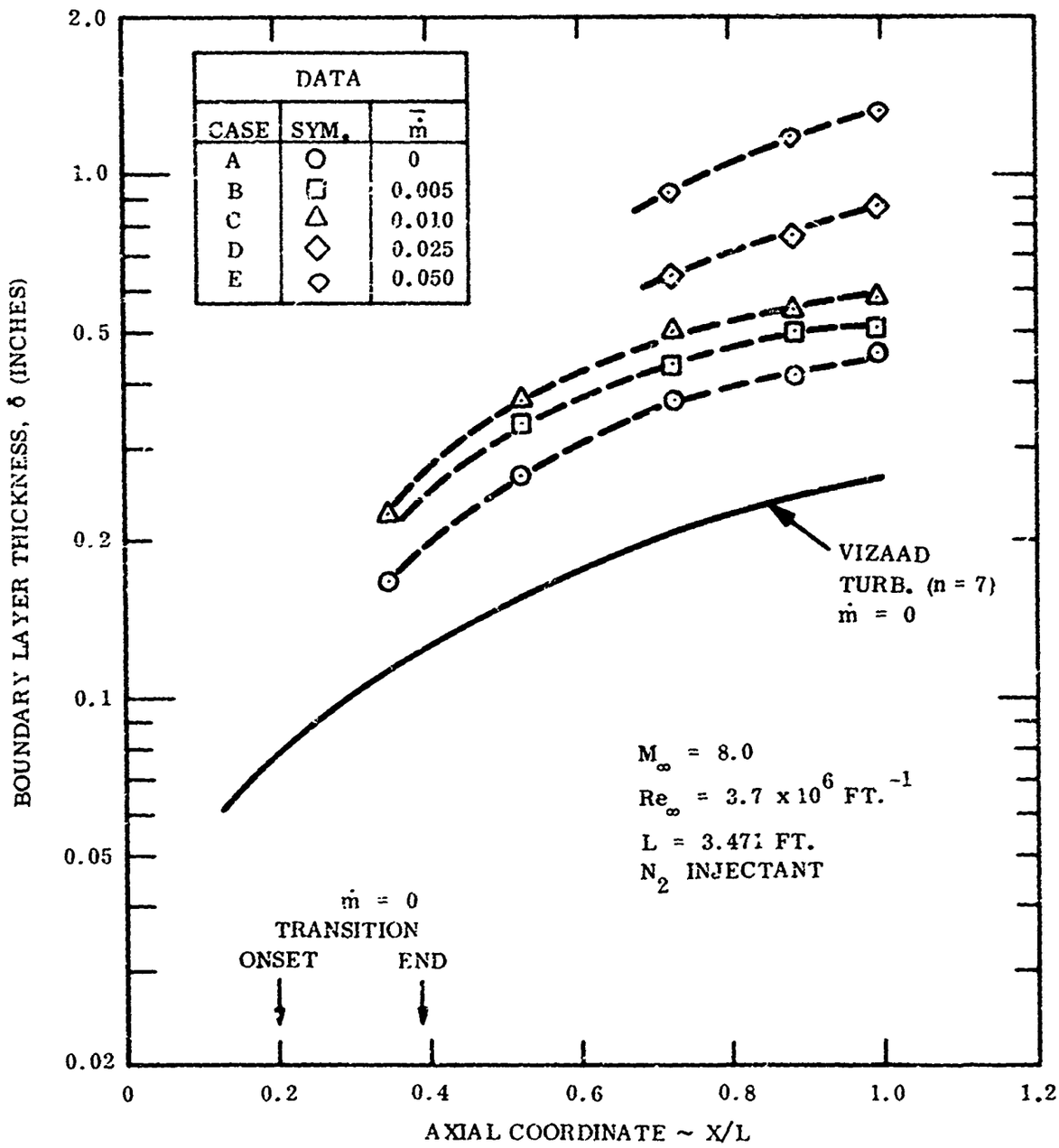

Figure 11. Effect of Mass Addition on the Boundary Layer Thickness of a Sharp 7.25° Half Angle Cone ($Re_\infty = 3.7 \times 10^6 ft^{-1}$)

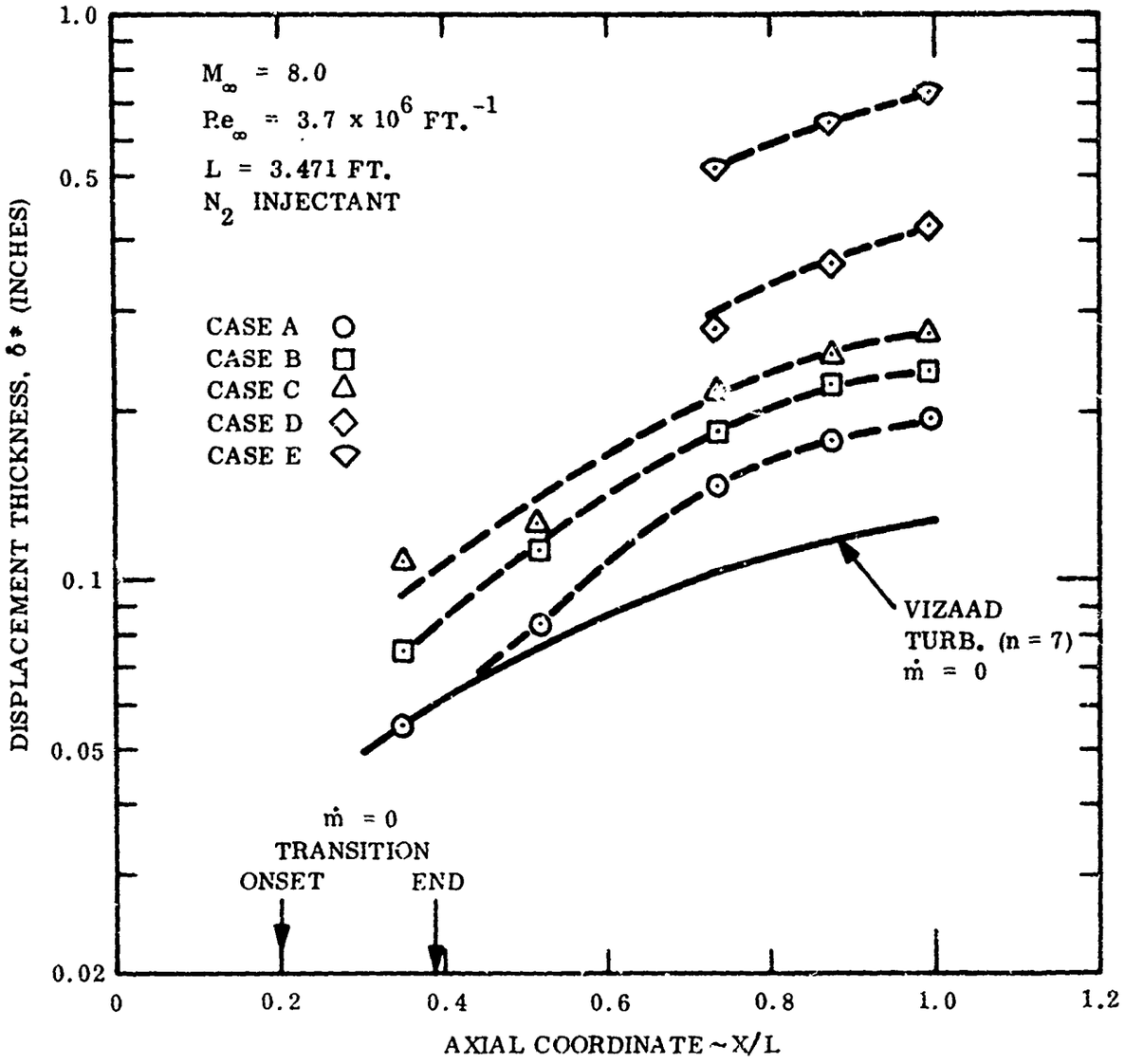

Figure 12. Effect of Mass Addition on the Displacement Thickness of a Sharp 7.25° Half Angle Cone (Re_∞ = 3.7 x 10^6 ft^{-1})

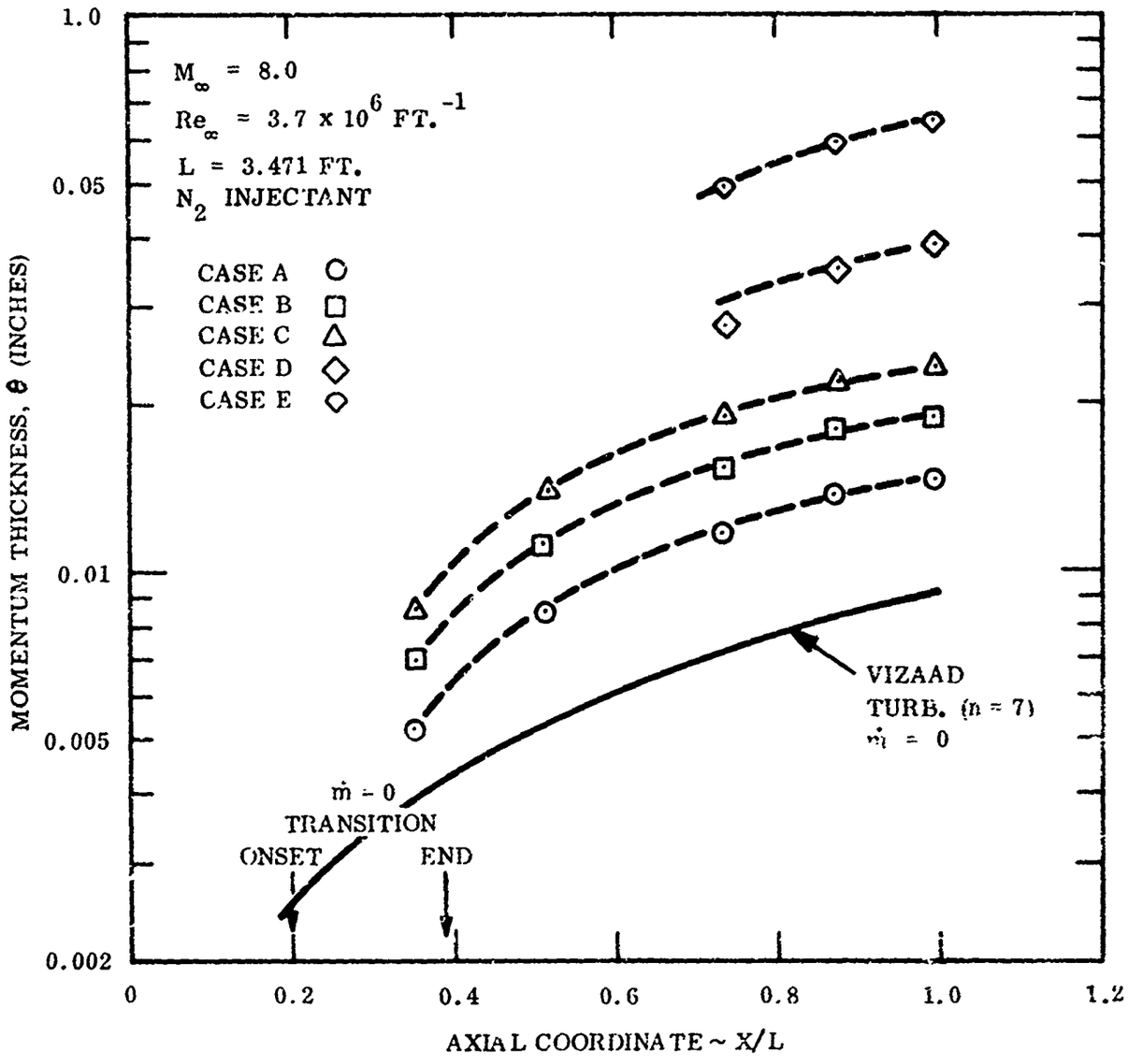

Figure 13. Effect of Mass Addition on the Momentum Thickness of a Sharp 7.25° Half Angle Cone (Re_∞ = 3.7 x 10^6 ft^{-1})

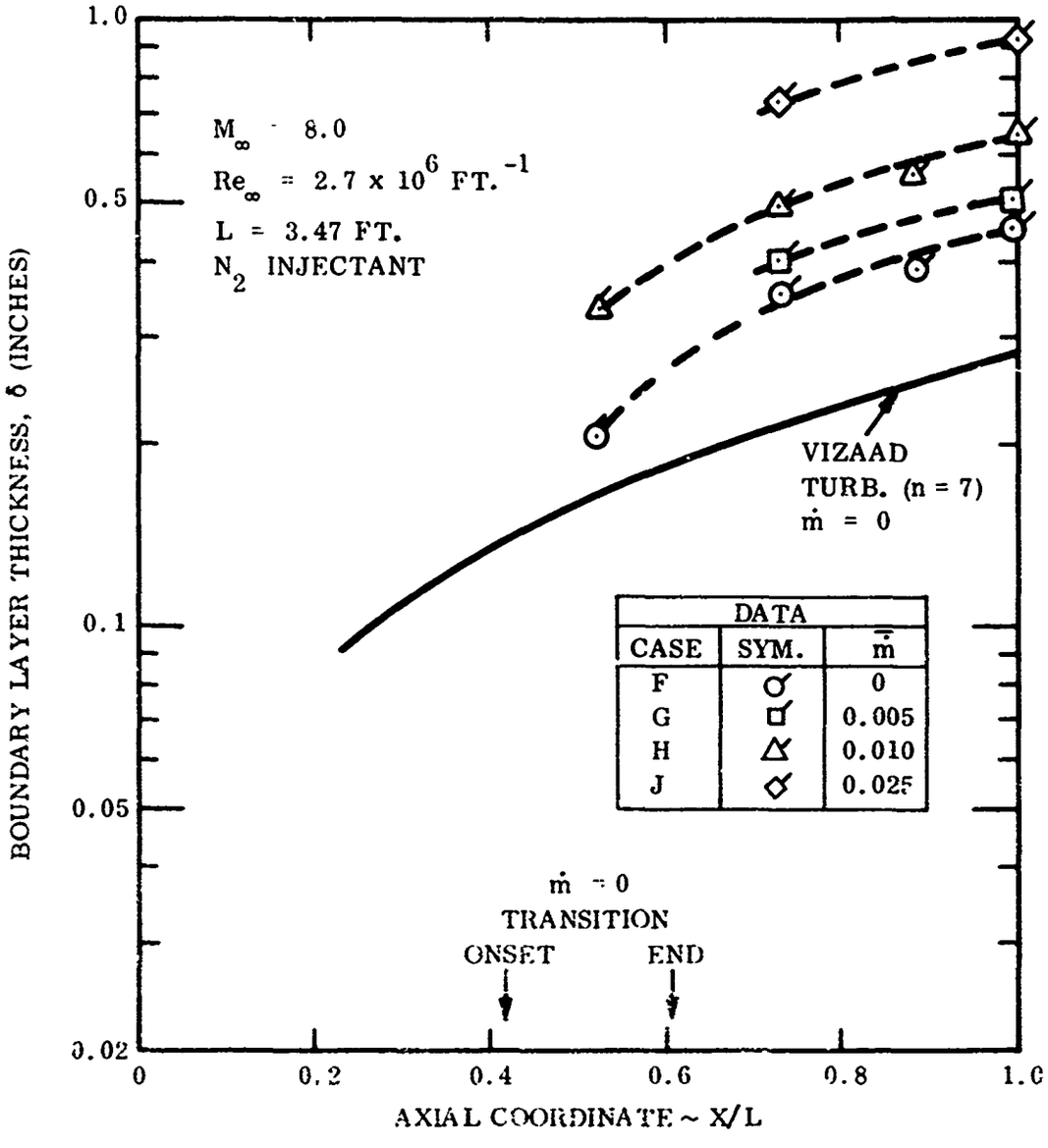

Figure 14. Effect of Mass Addition on the Boundary Layer Thickness of a Sharp 7.25° Half Angle Cone ($Re_\infty = 2.7 \times 10^6$ ft^{-1})

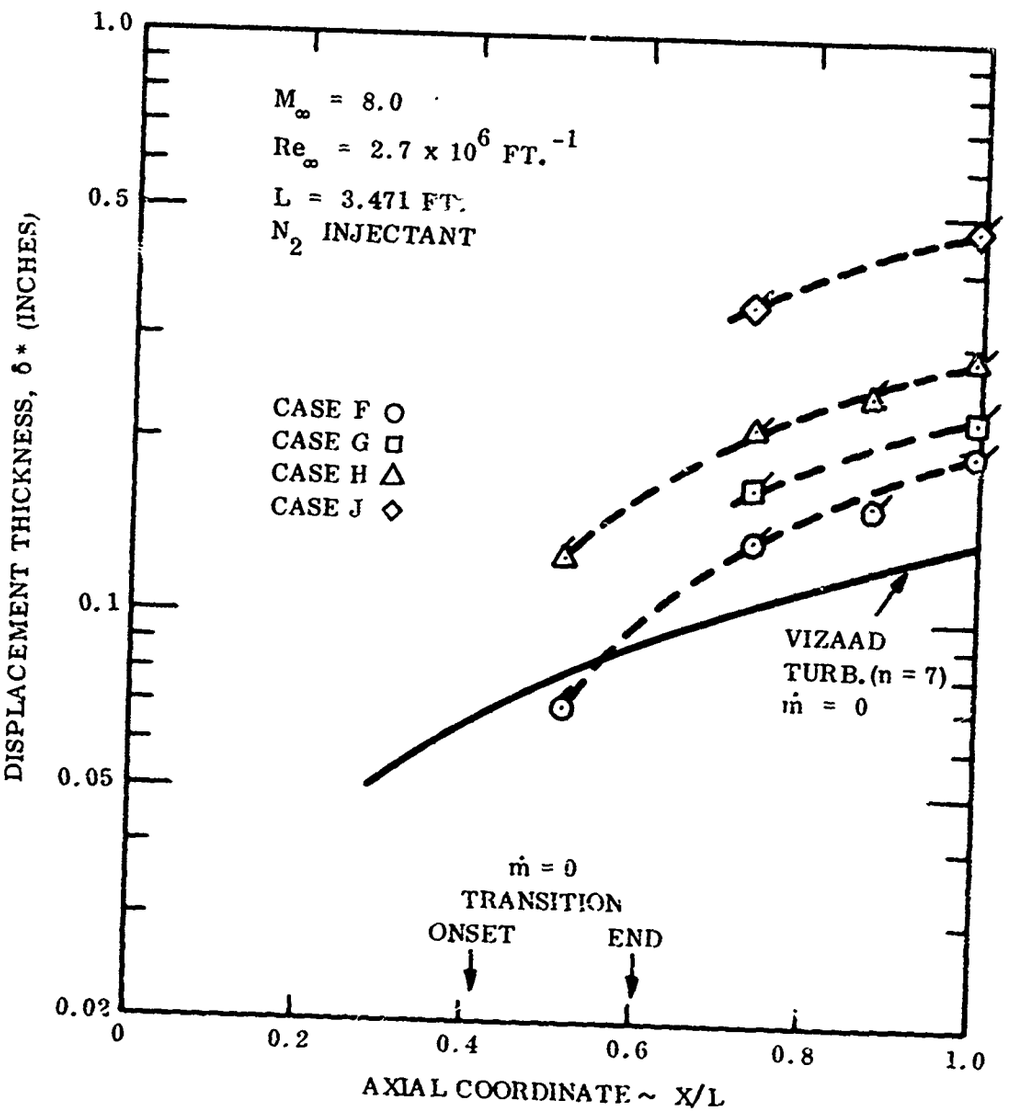

Figure 15. Effect of Mass Addition on the Displacement Thickness of a Sharp 7.25° Half Angle Cone (Re_∞ = 2.7 x 10^6 ft^{-1})

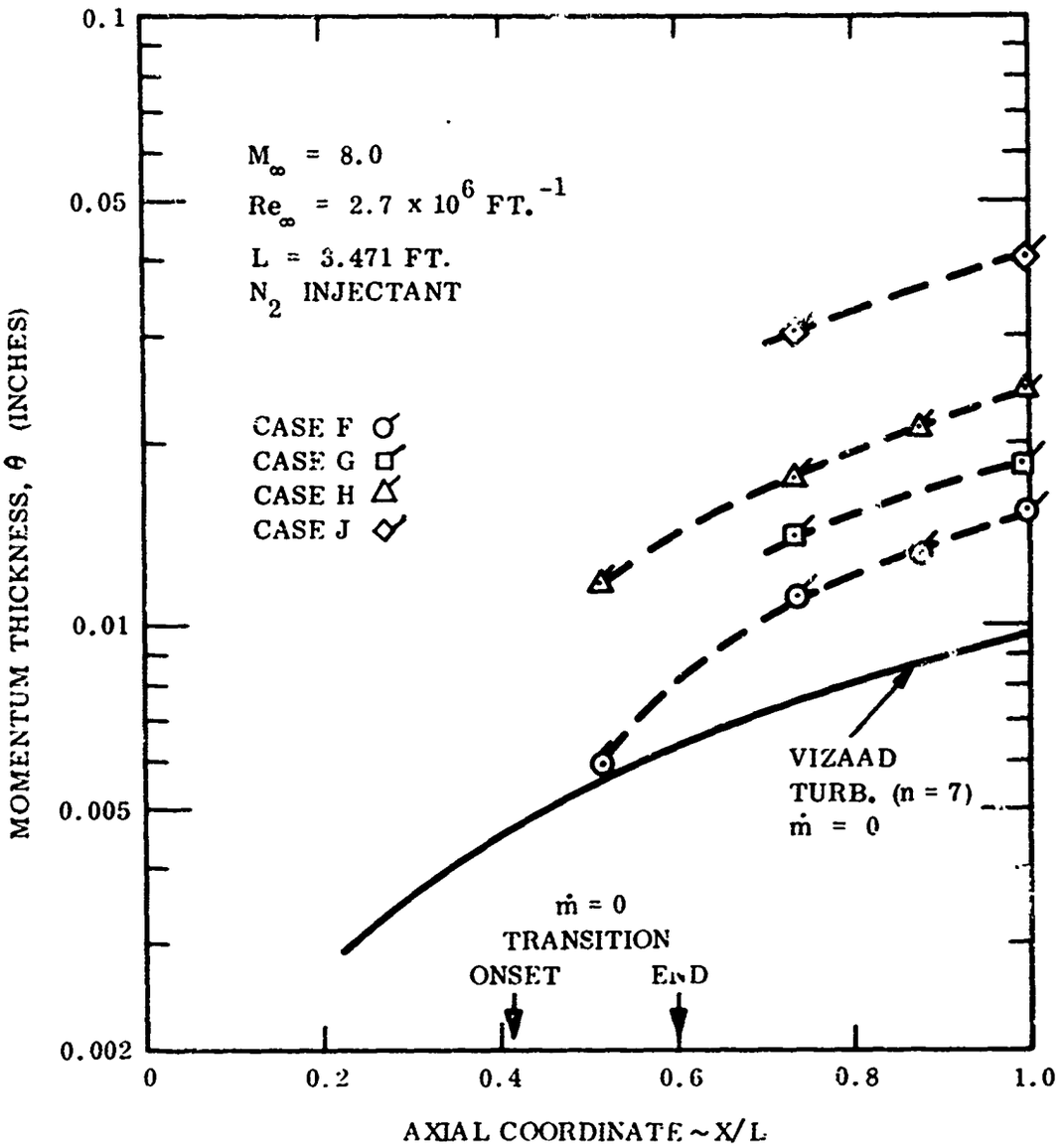

Figure 16. Effect of Mass Addition on the Momentum Thickness of a Sharp 7.25° Half Angle Cone ($Re_\infty = 2.7 \times 10^6$ ft^{-1})

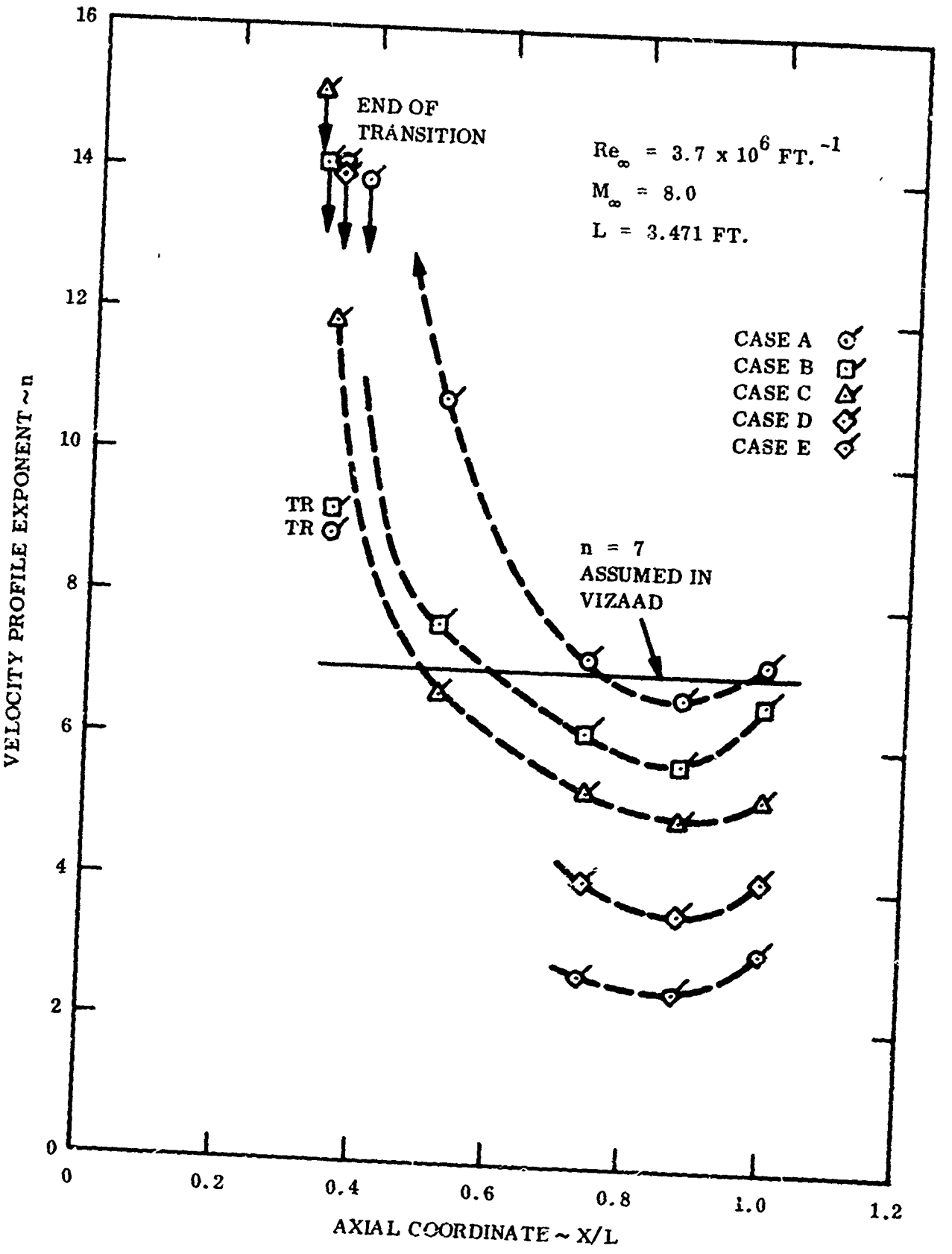

Figure 17. Effect of Mass Addition on Velocity Profile Exponent (Re_∞ = 3.7 x 10^6 ft^{-1})

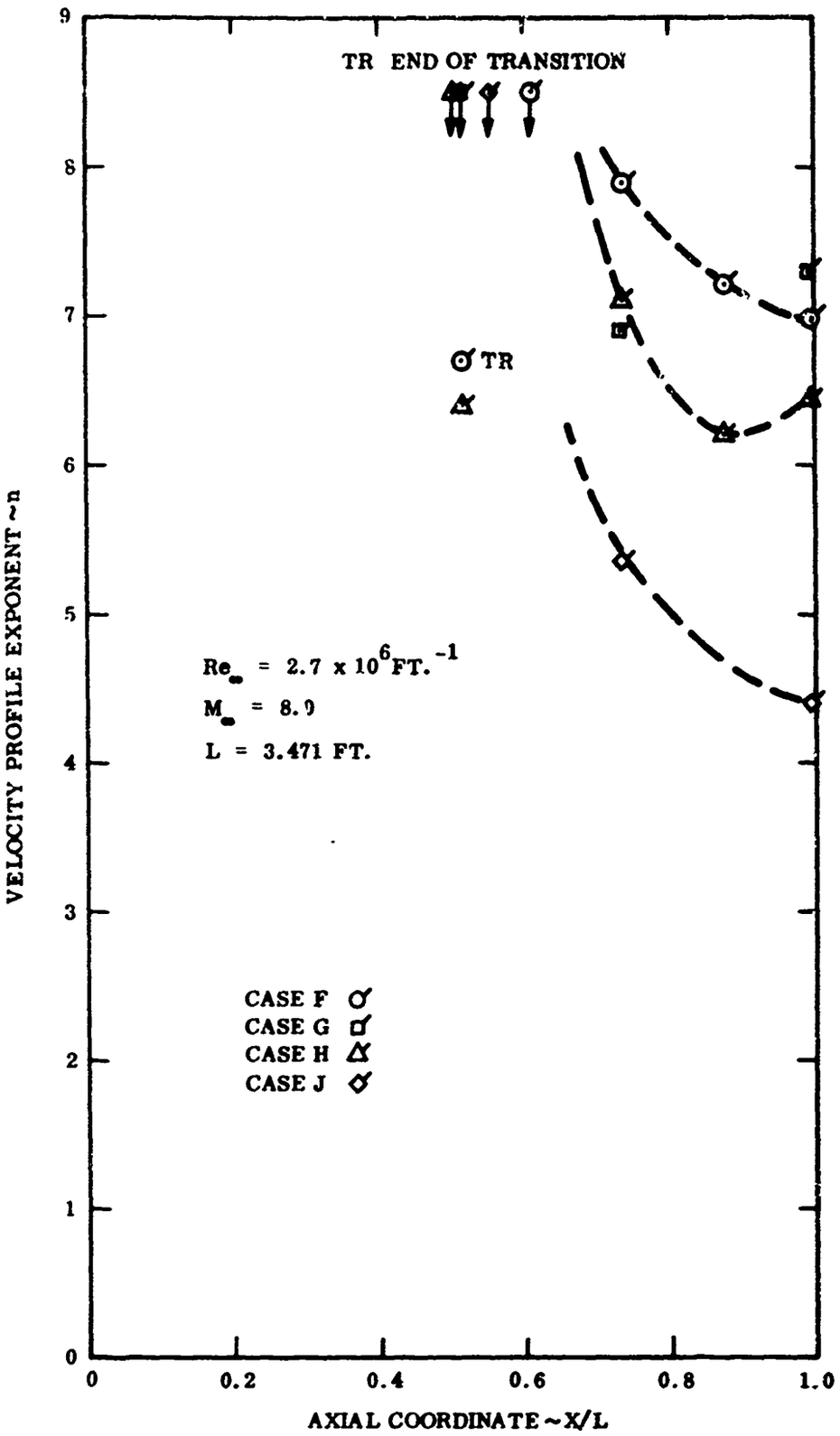

Figure 18. Effect of Mass Addition on Velocity Profile Exponent (Re_∞ = 2.7 x 10^6 ft^{-1})

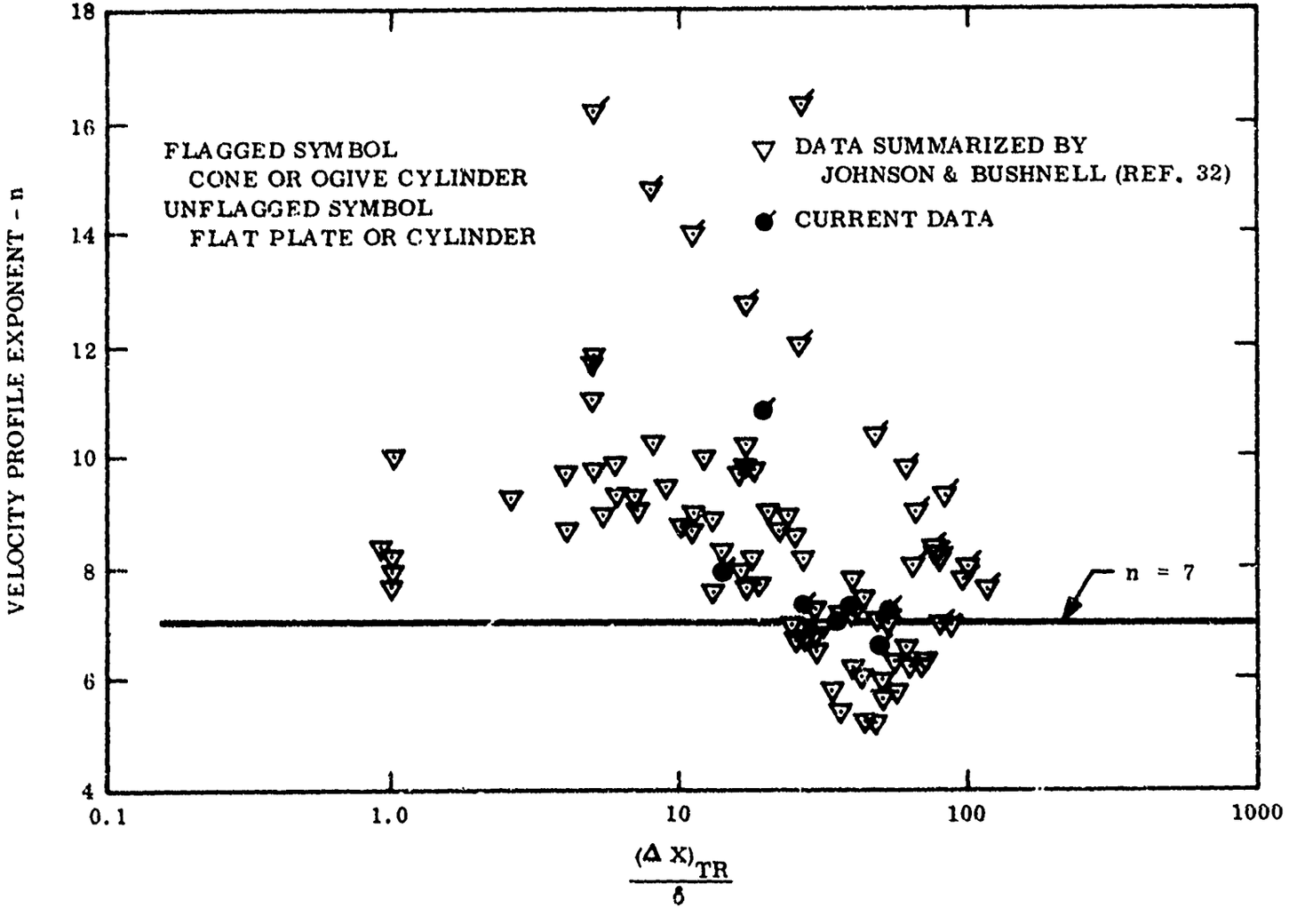

Figure 19. Variation of Velocity Profile Exponent with Normalized Length from End of Transition

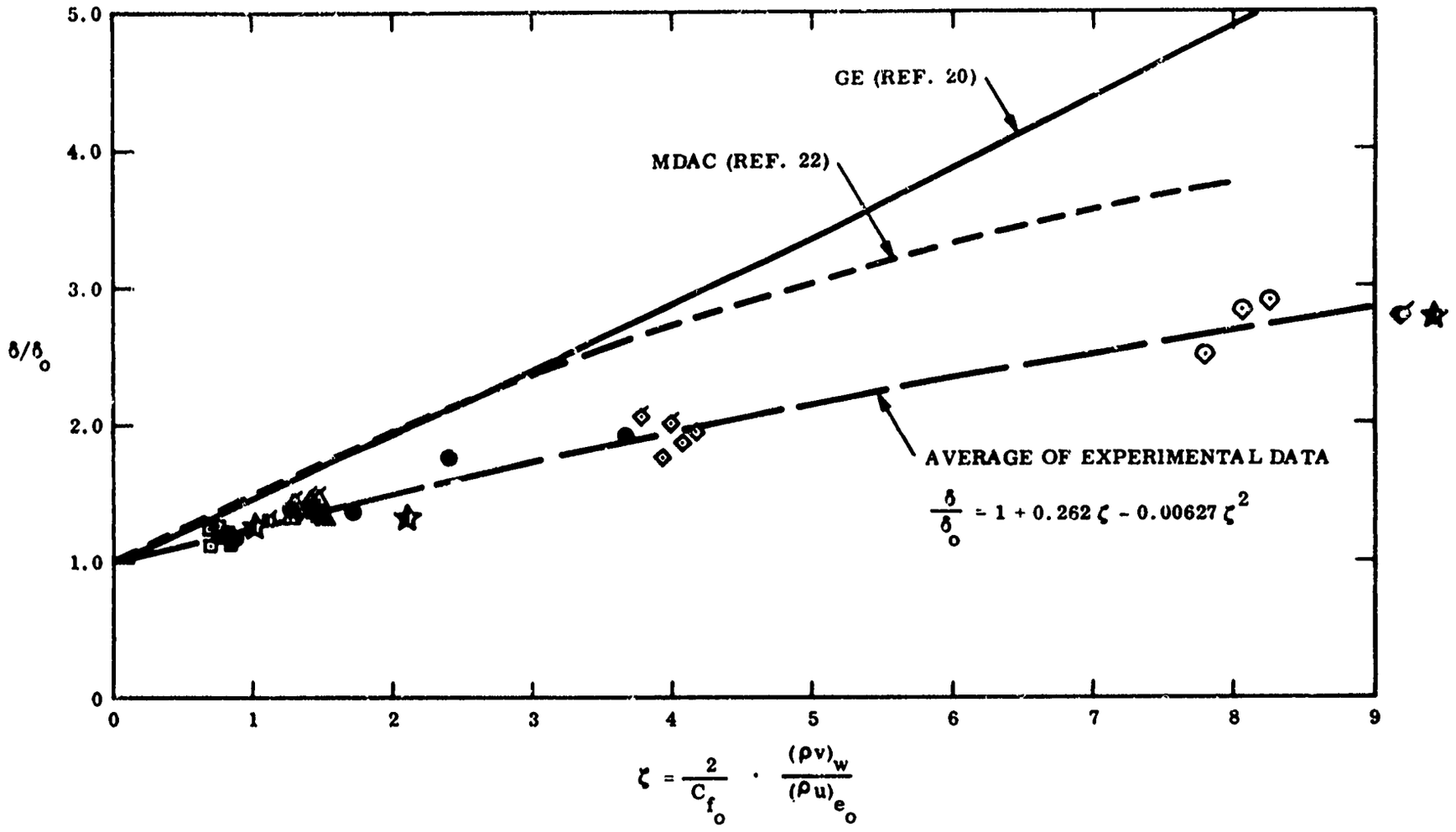

Figure 20. Effect of Mass Addition on Boundary Layer Thickness (Turbulent)

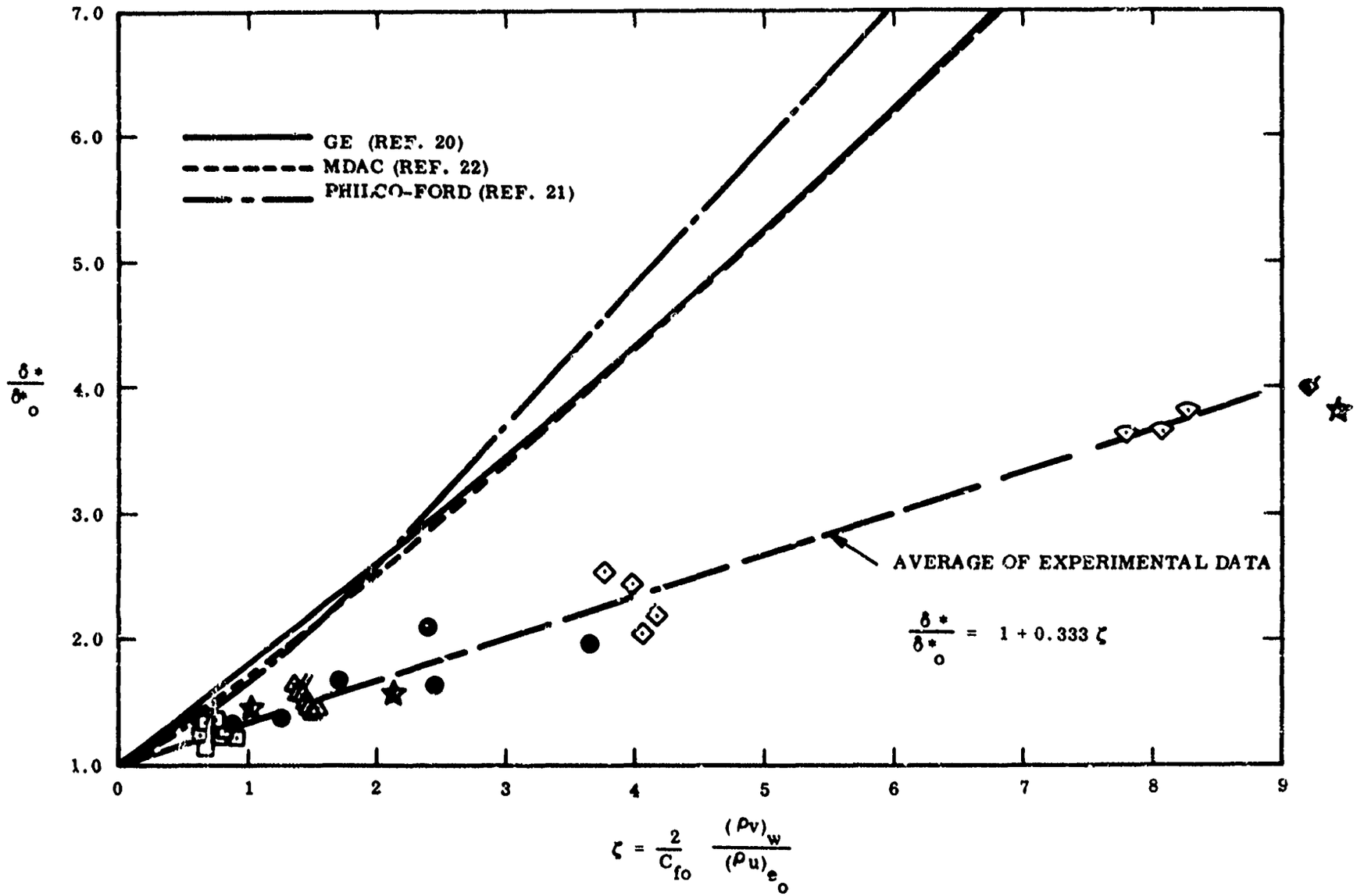

Figure 21. Effect of Mass Addition on Displacement Thickness (Turbulent)

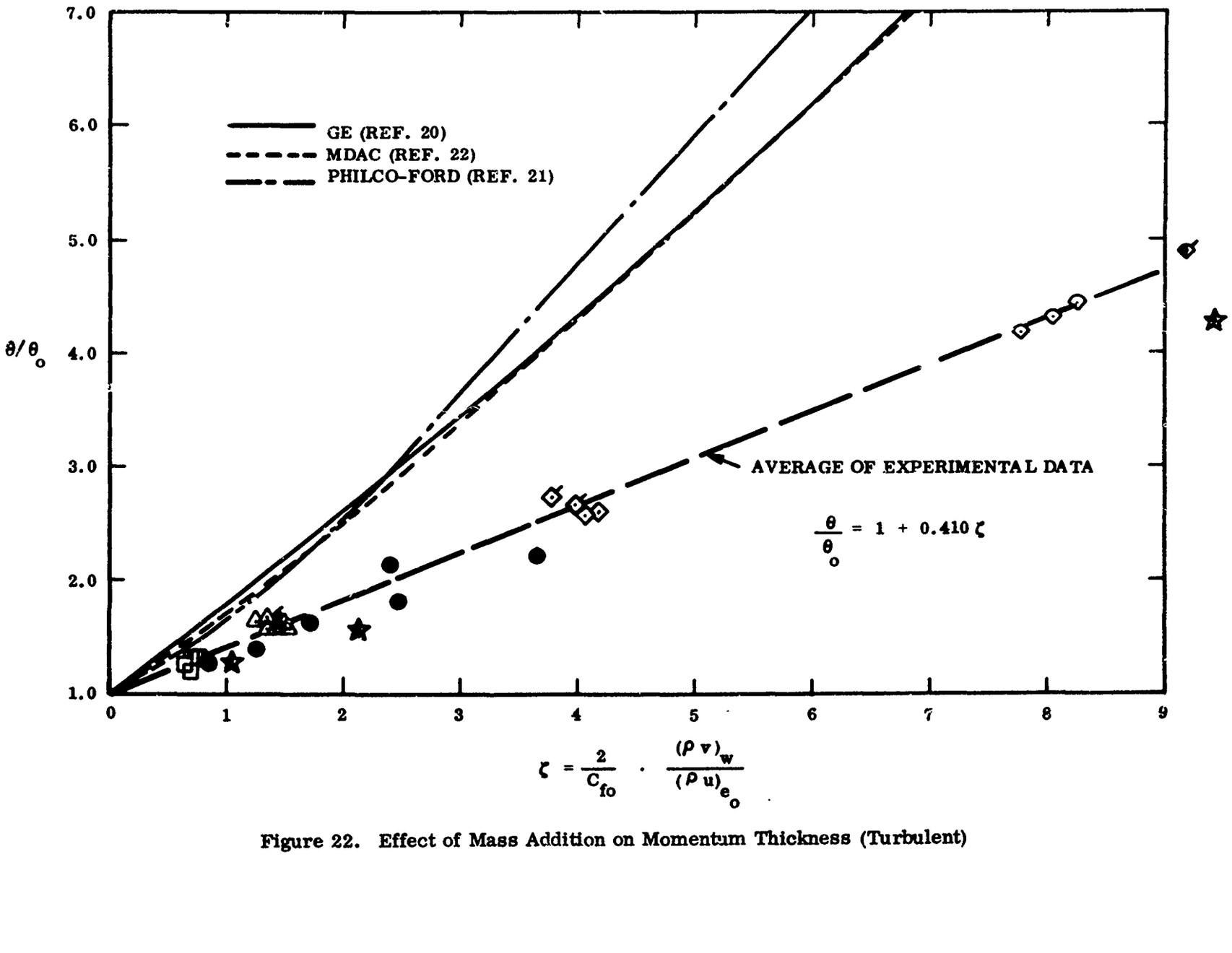

Figure 22. Effect of Mass Addition on Momentum Thickness (Turbulent)

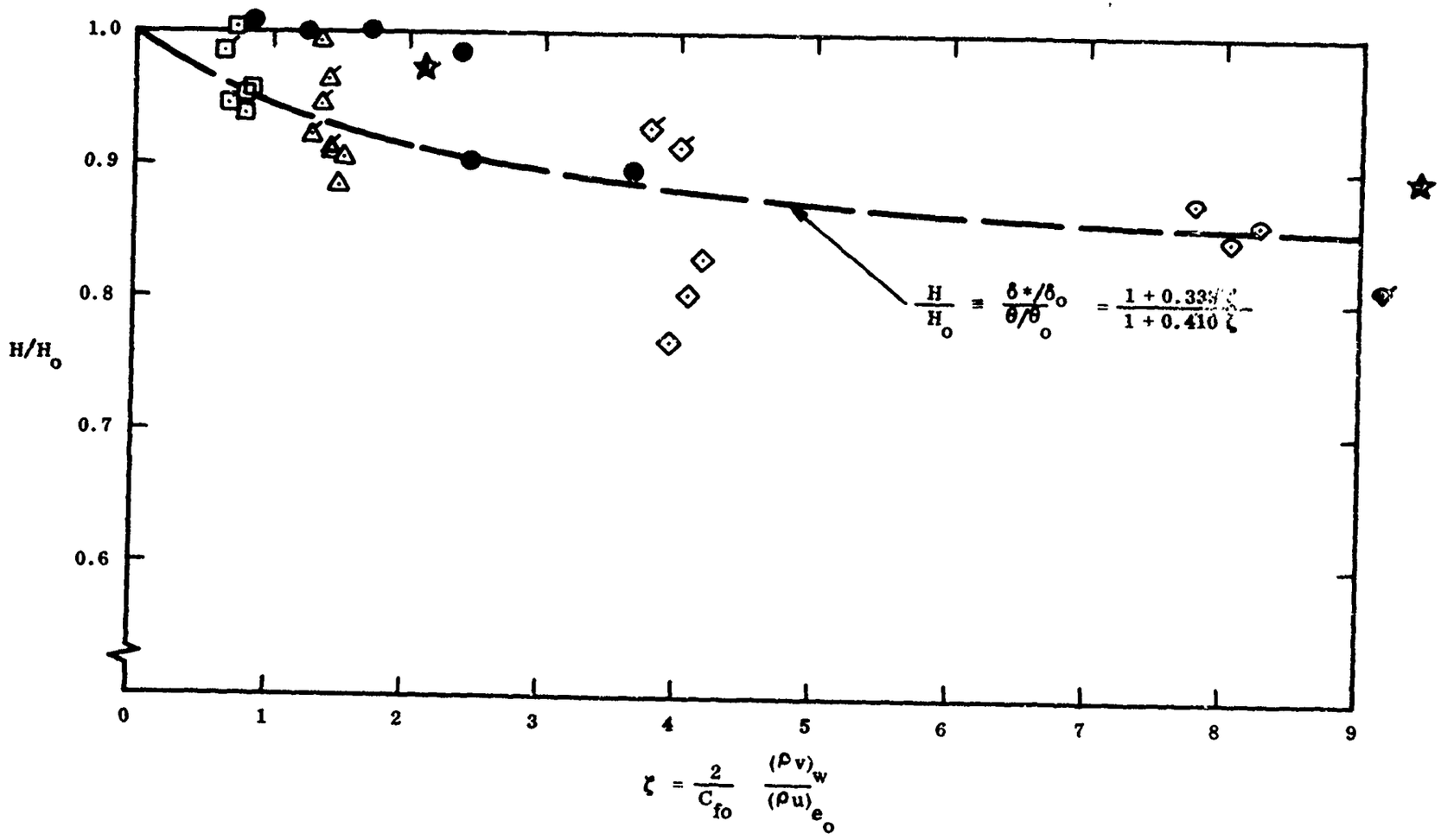

Figure 23. Effect of Mass Addition on the Form Factor - $H = \delta^*/\theta$ (Turbulent)

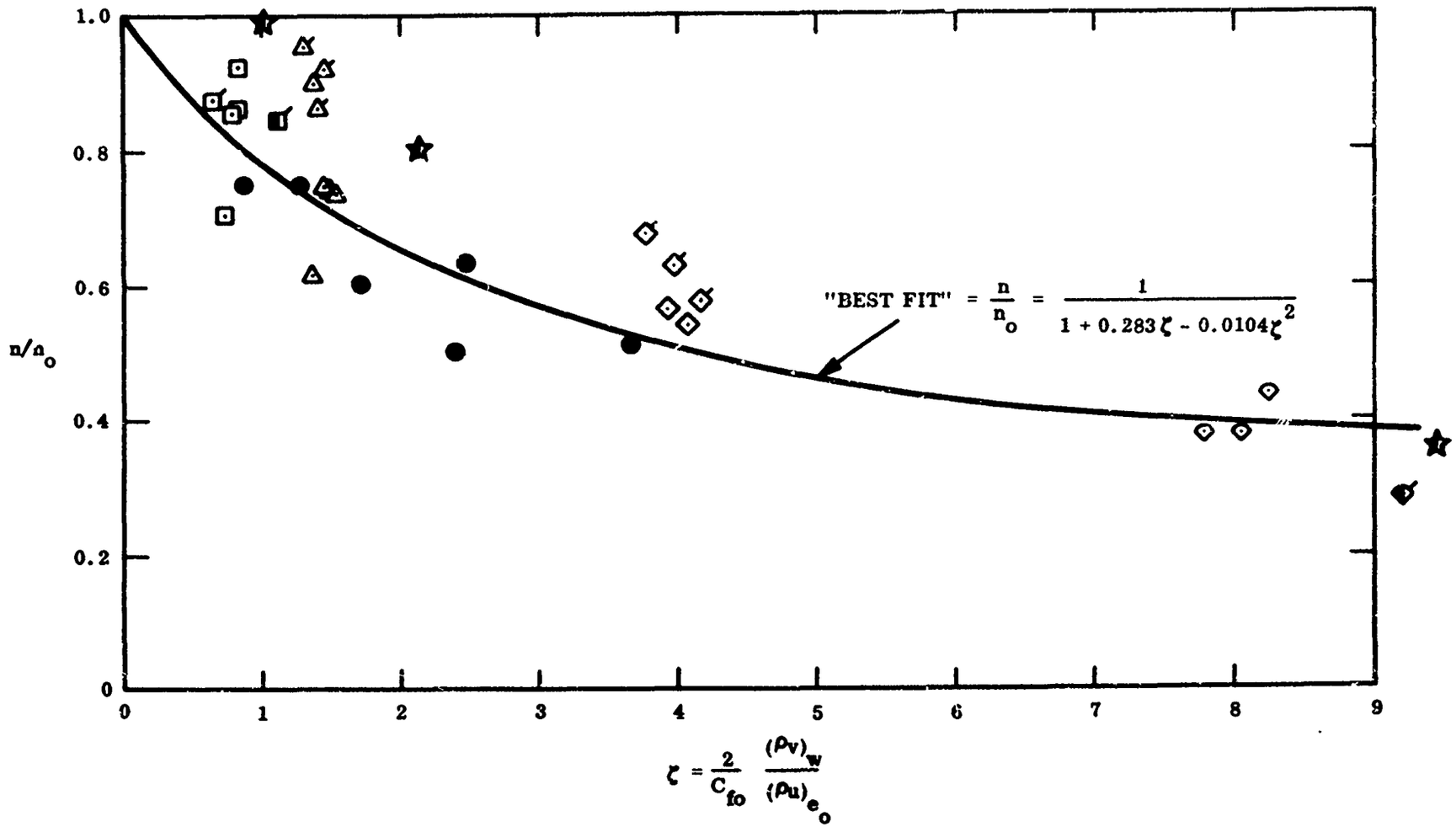

Figure 24. Effect of Mass Addition on Velocity Profile Exponent – n

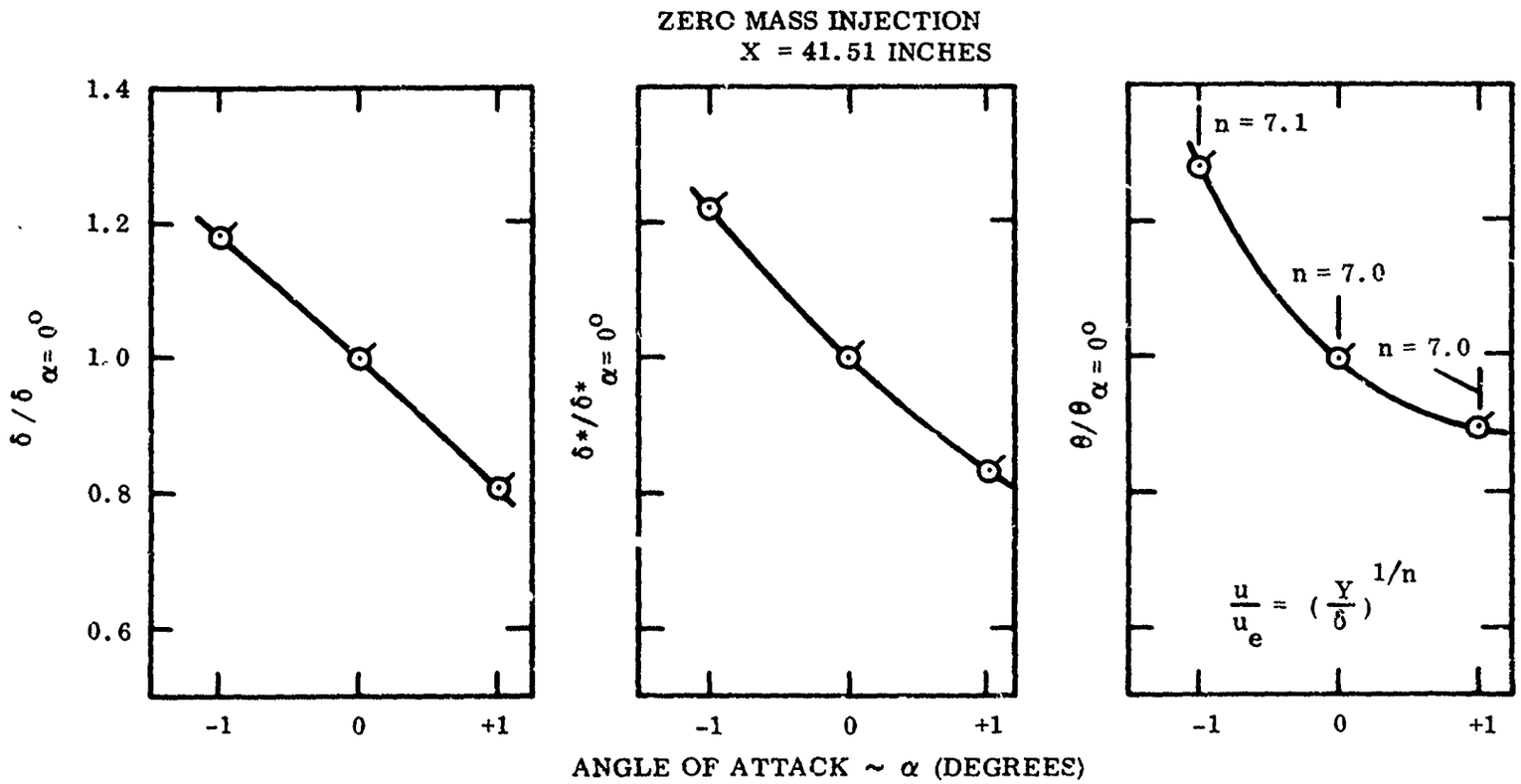

Figure 25. Effect of Angle of Attack on Viscous Layer Thickness

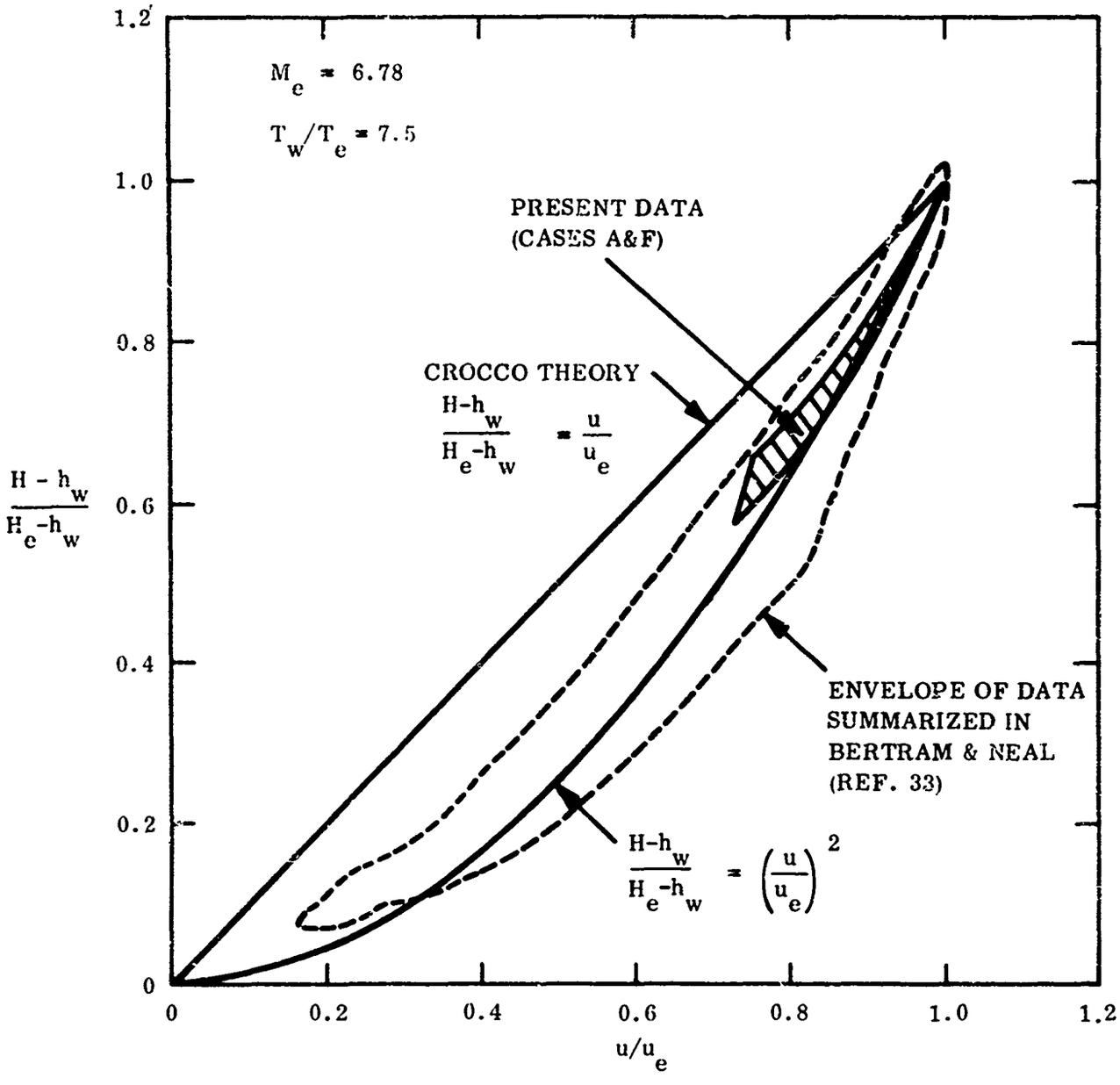

Figure 26. Comparison of Total Enthalpy Profile with Crocco Theory
(Zero Mass Injection)

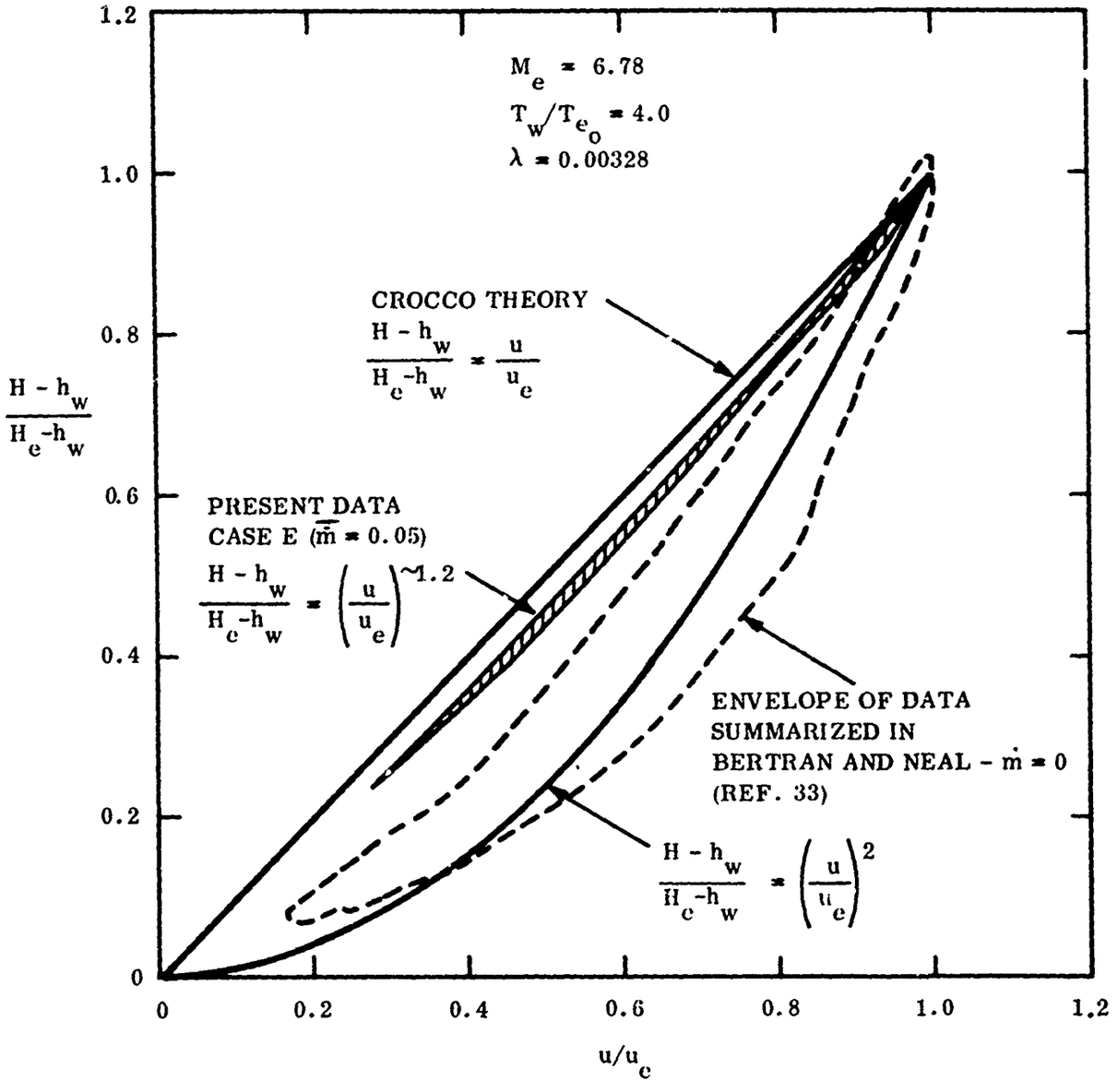

Figure 27. Comparison of Total Enthalpy Profile with Crocco Theory (Effect of Mass Injection)

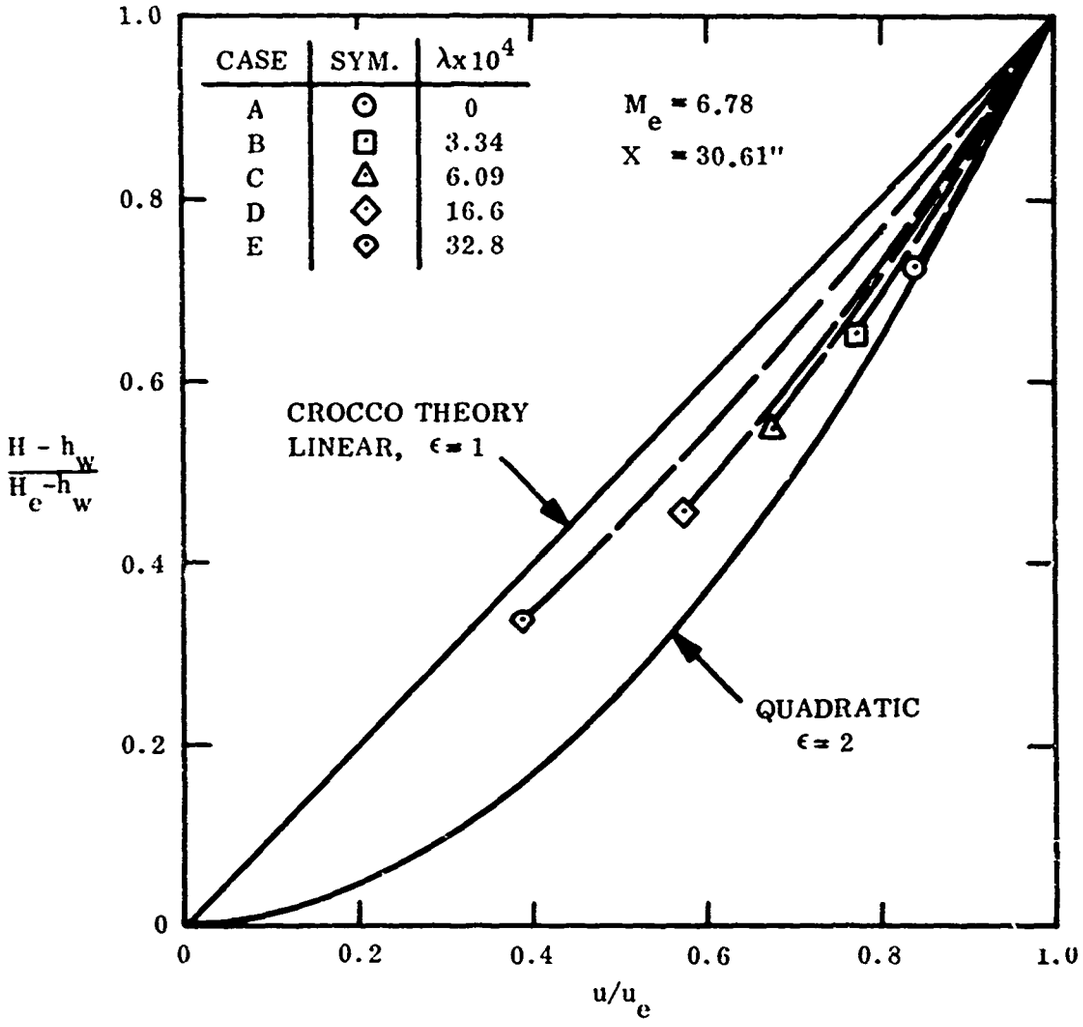

Figure 28. Effect of Mass Injection on Total Enthalpy Profile

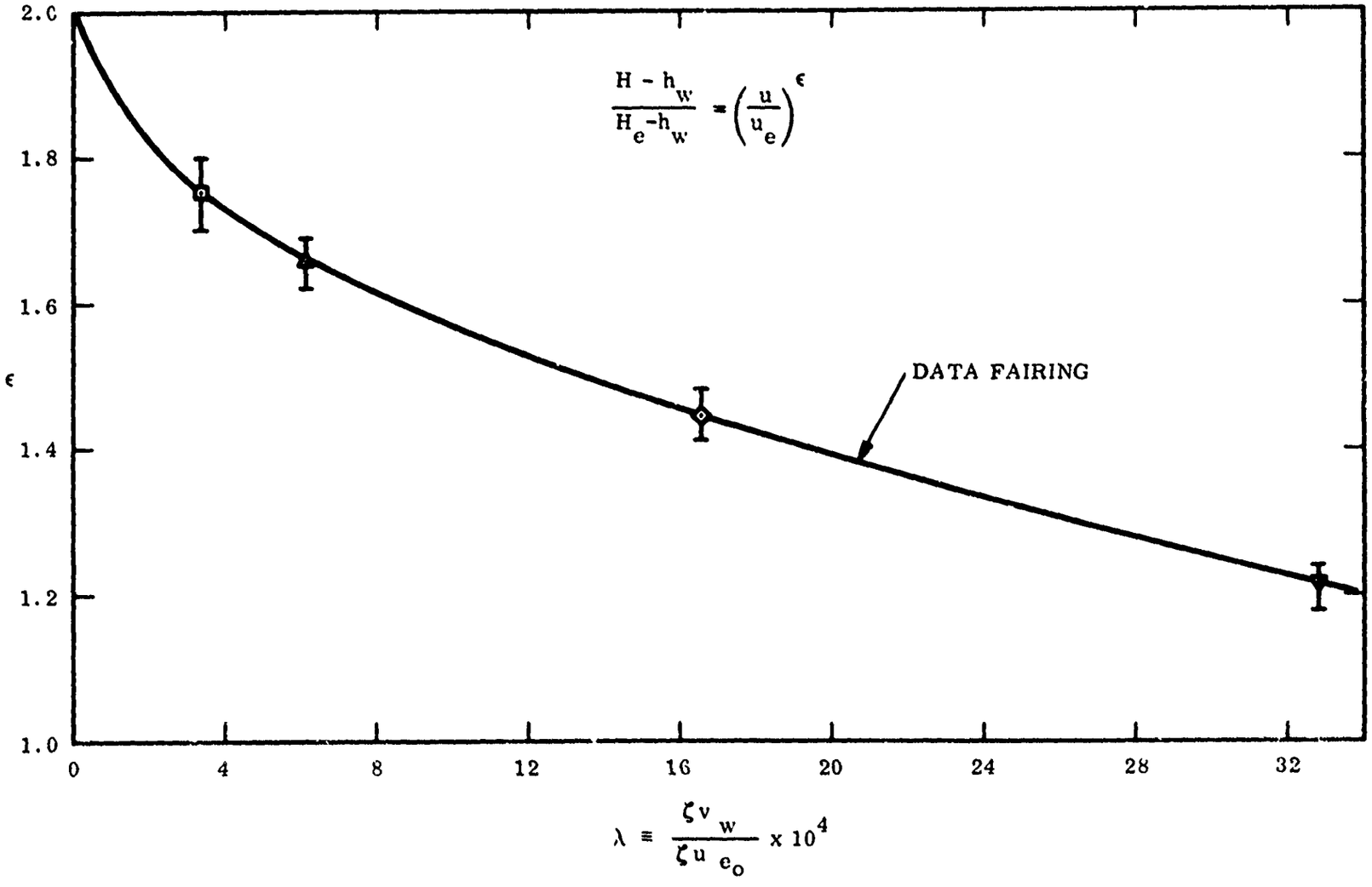

Figure 29. Effect of Mass Injection on Exponent in Total Enthalpy Relation

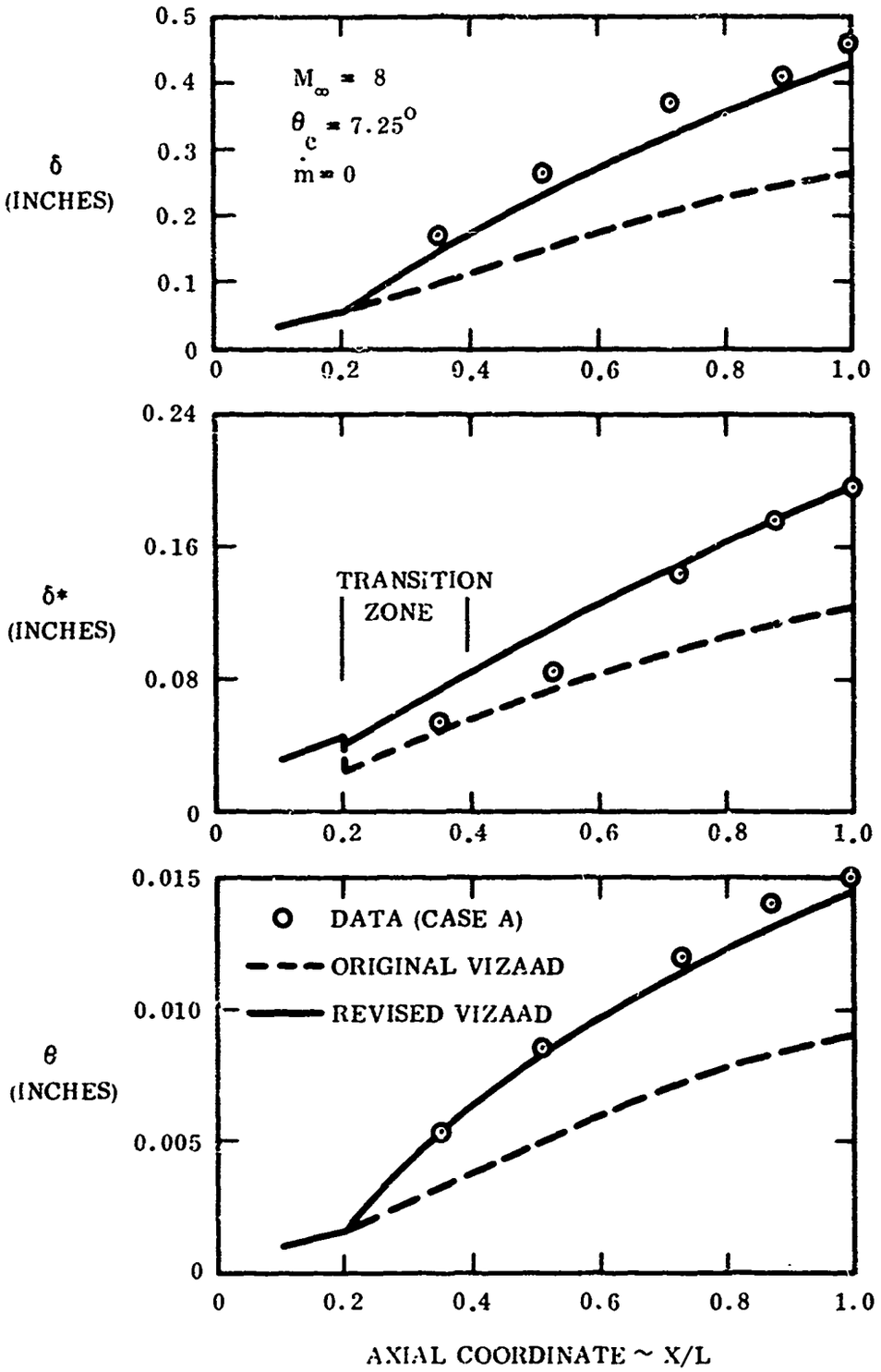

Figure 30. Comparison of Theory with Experimental Viscous Layer Thicknesses (Case A)

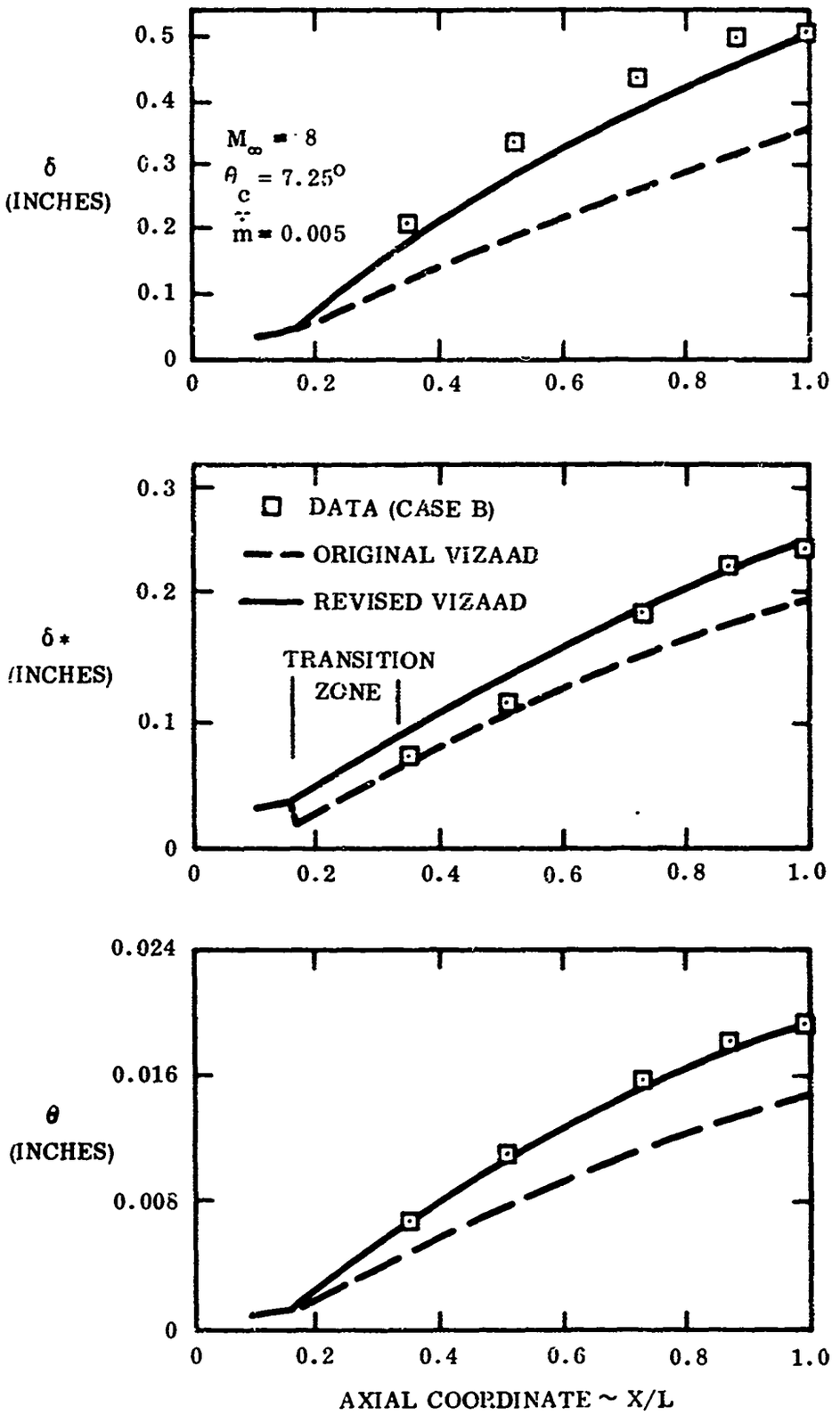

Figure 31. Comparison of Theory with Experimental Viscous Layer Thicknesses (Case B)

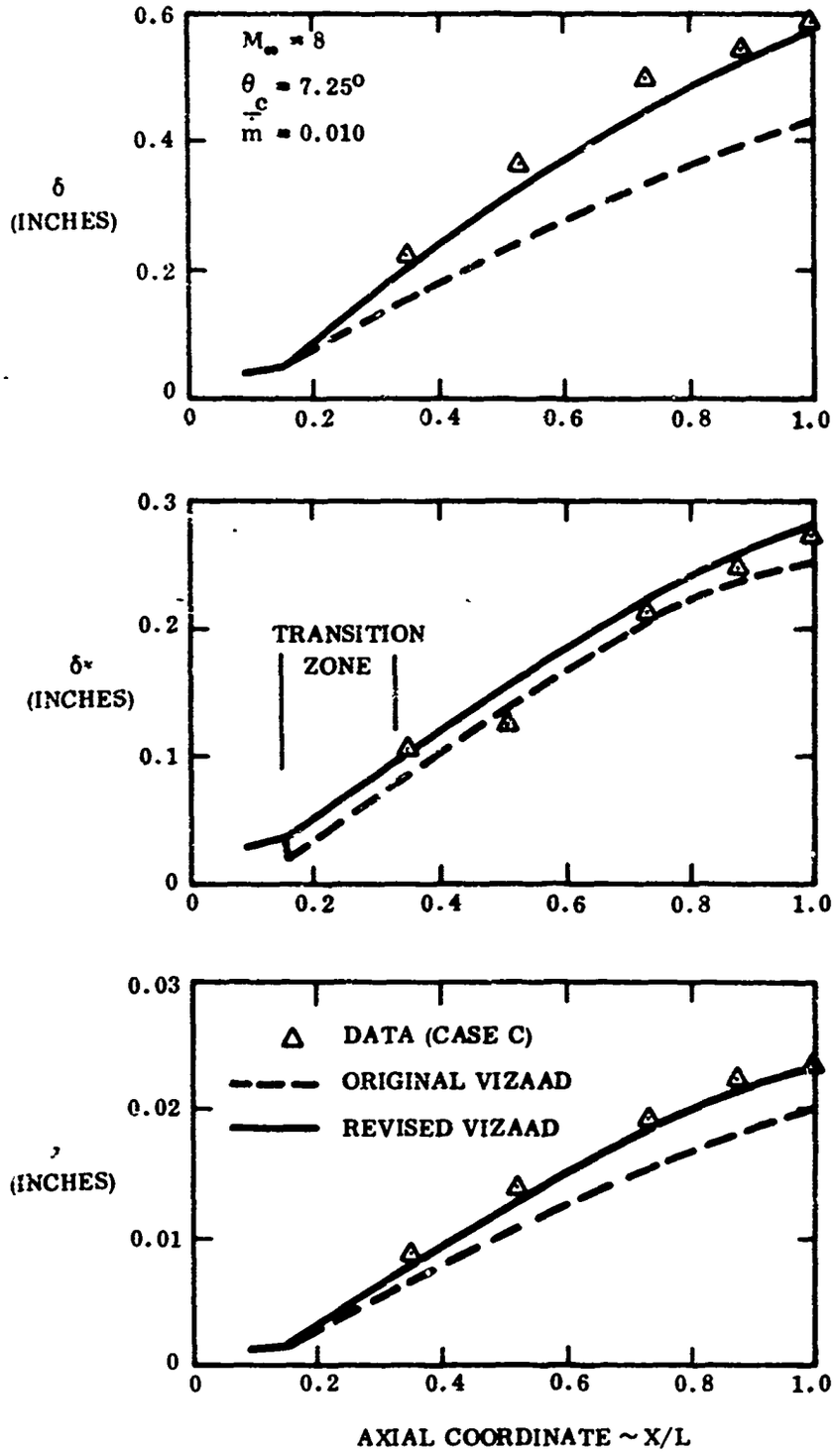

Figure 32. Comparison of Theory with Experimental Viscous Layer Thicknesses (Case C)

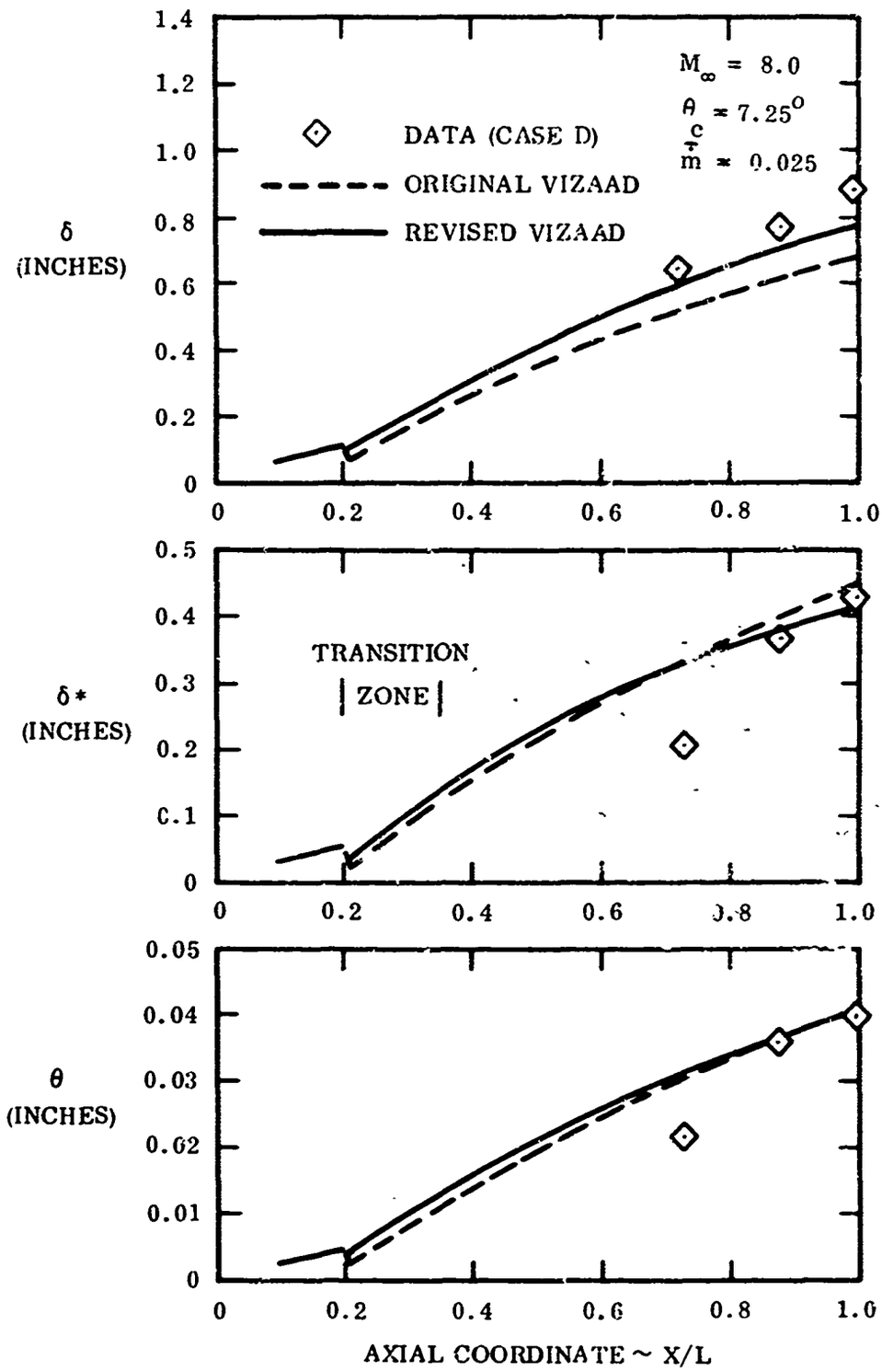

Figure 33. Comparison of Theory with Experimental Viscous Layer Thicknesses (Case D)

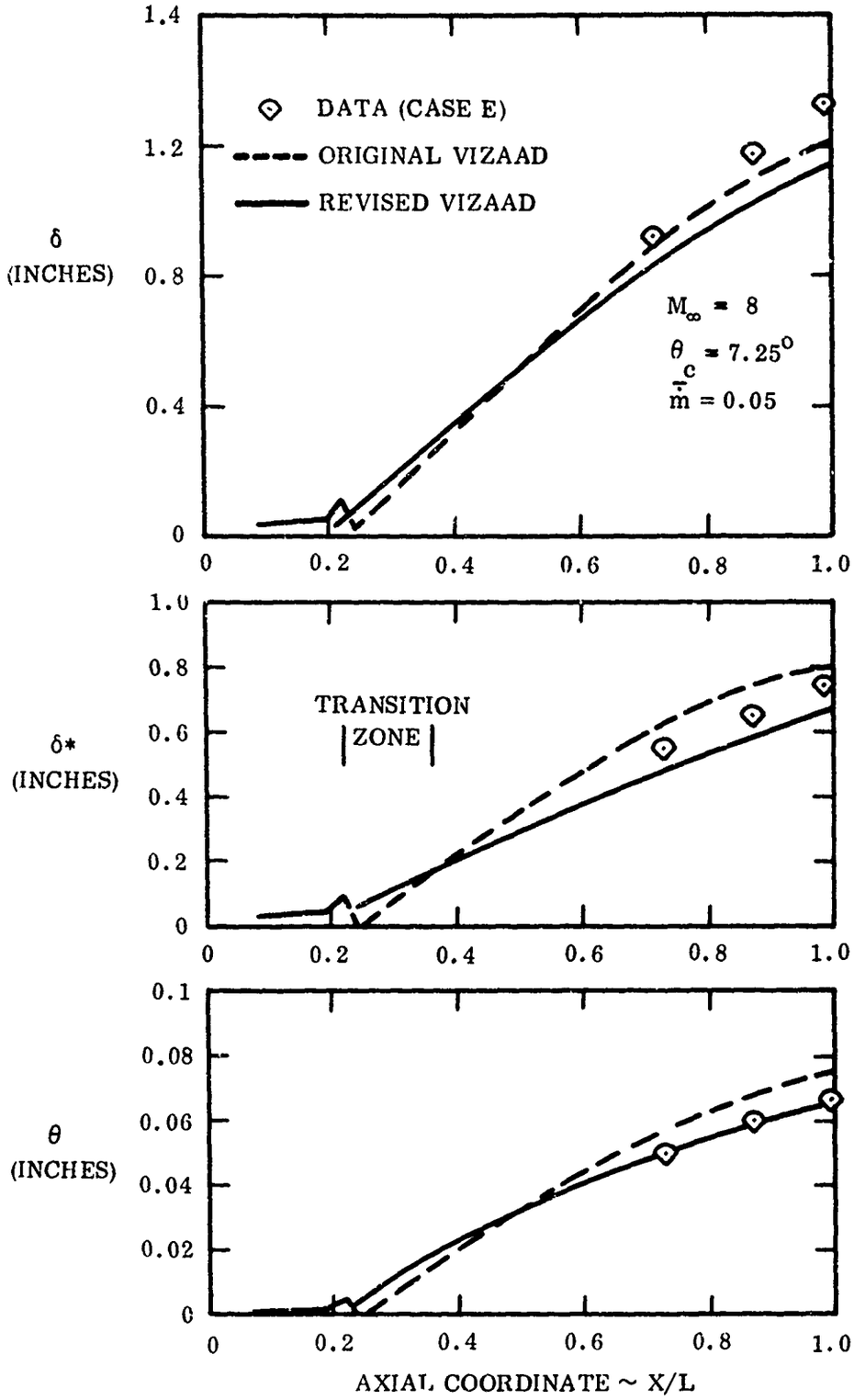

Figure 34. Comparison of Theory with Experimental Viscous Layer Thicknesses (Case E)

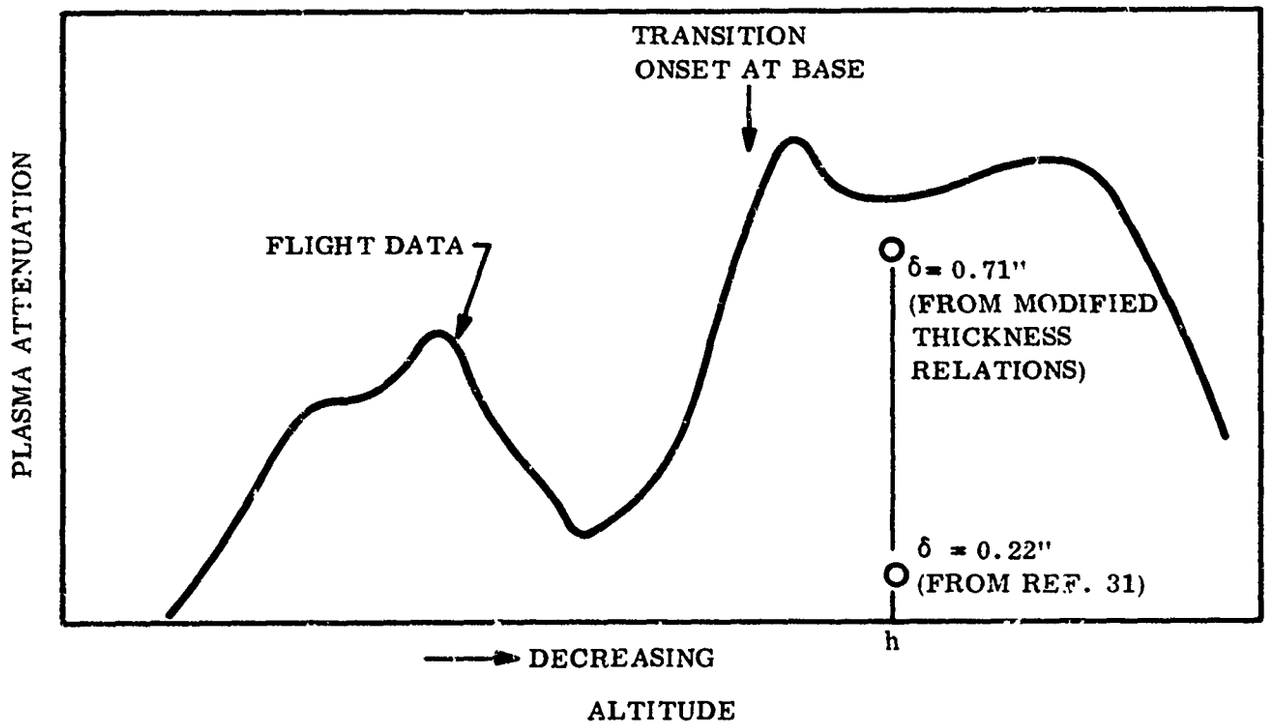

Figure 35. Slender (R/V) S Band Plasma Attenuation

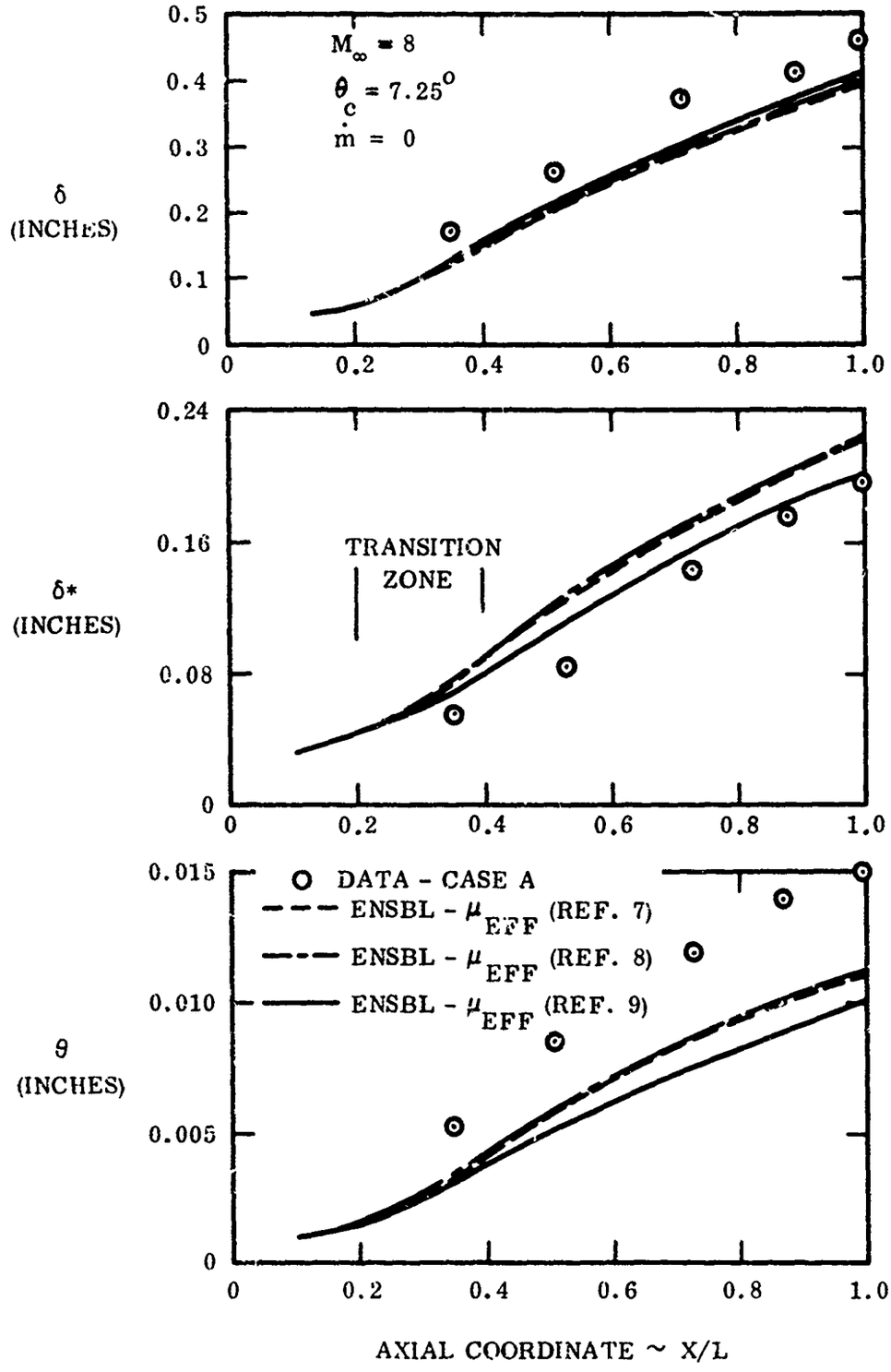

Figure 36. Comparison of ENSBL Program Results with Experimental Data

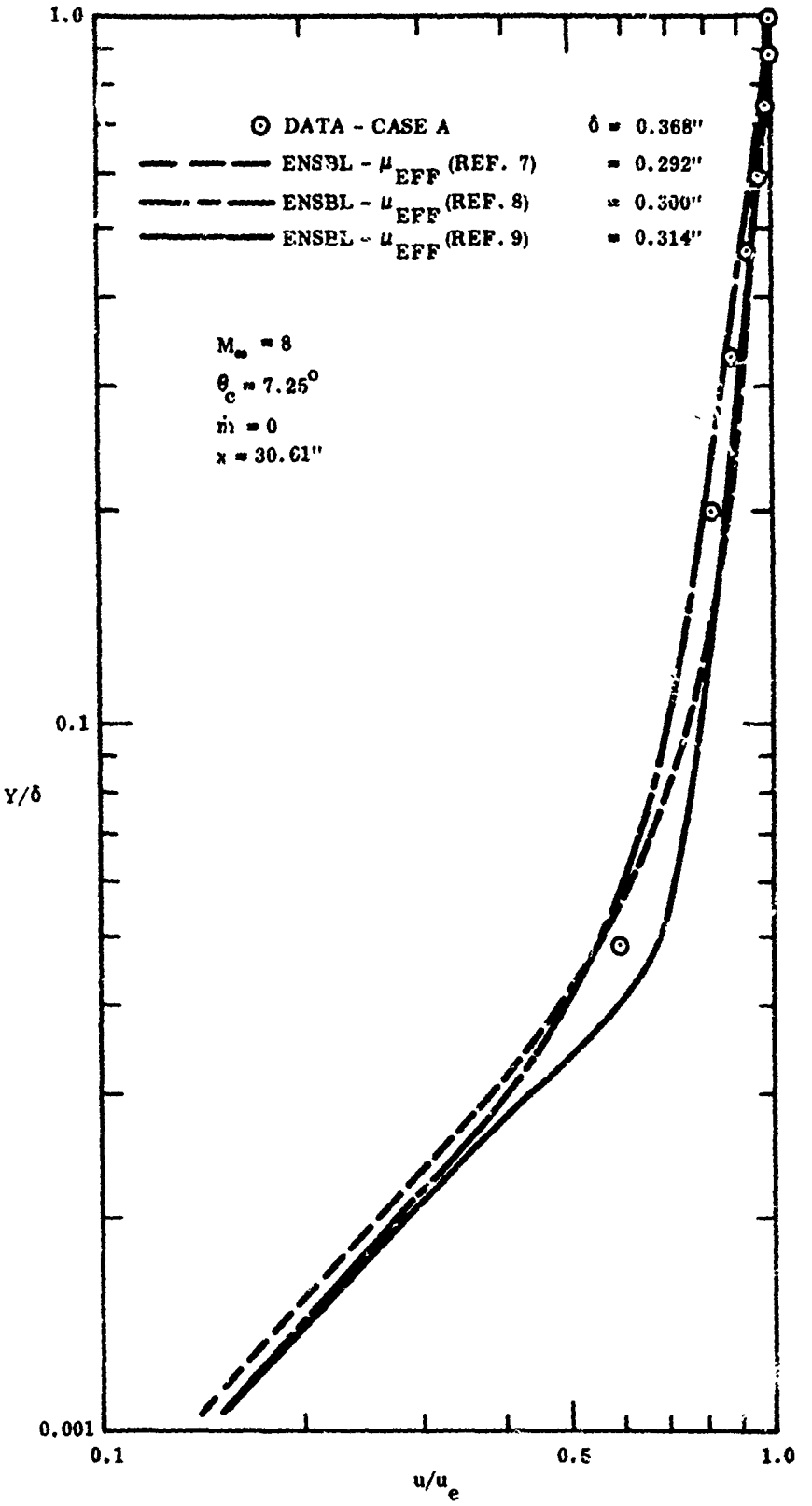

Figure 37. Profile Comparison of ENSBL Program Results with Data

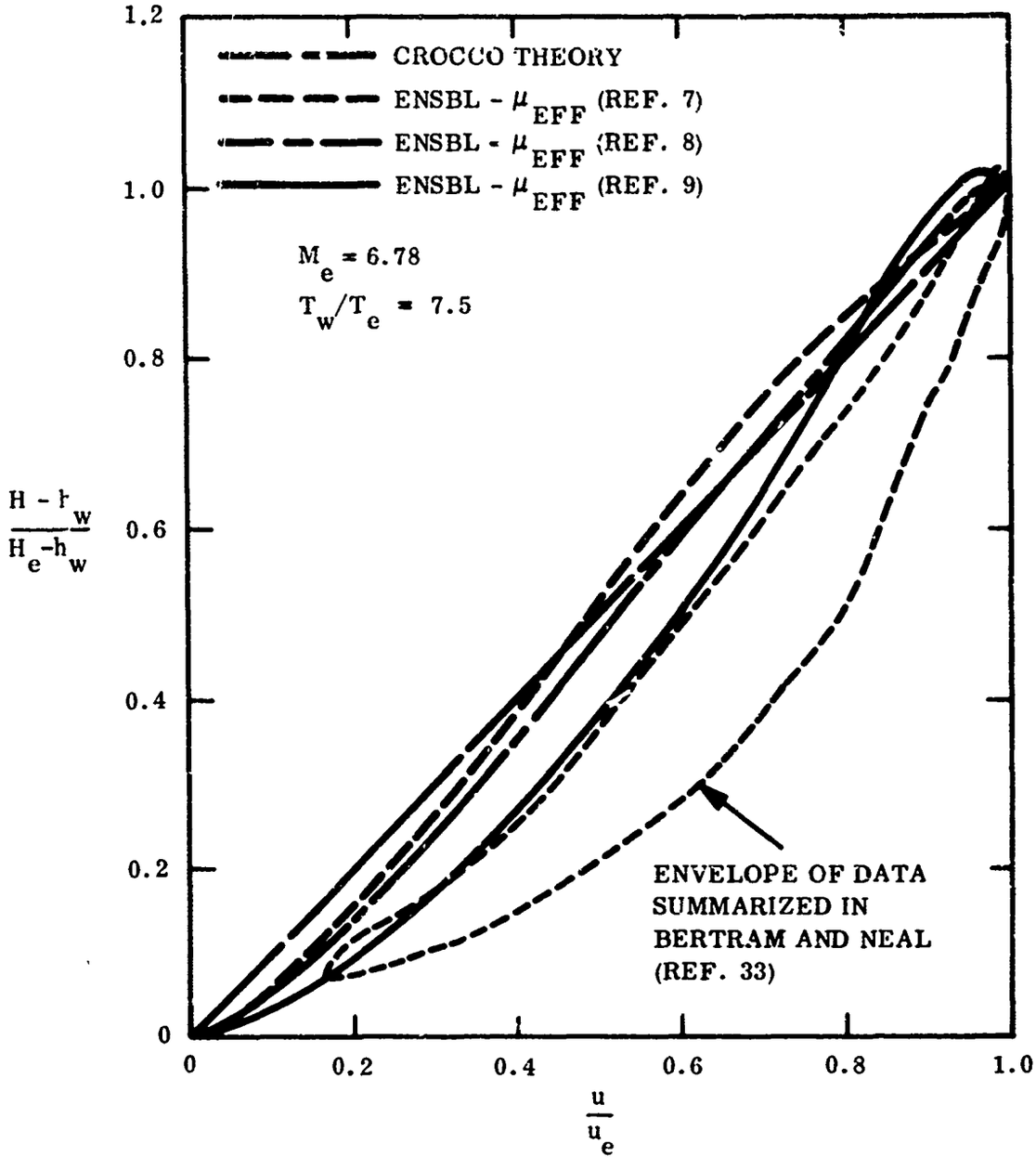

Figure 38. Comparison of Predicted Enthalpy Profiles with Crocco Theory and Data - Zero Mass Injection

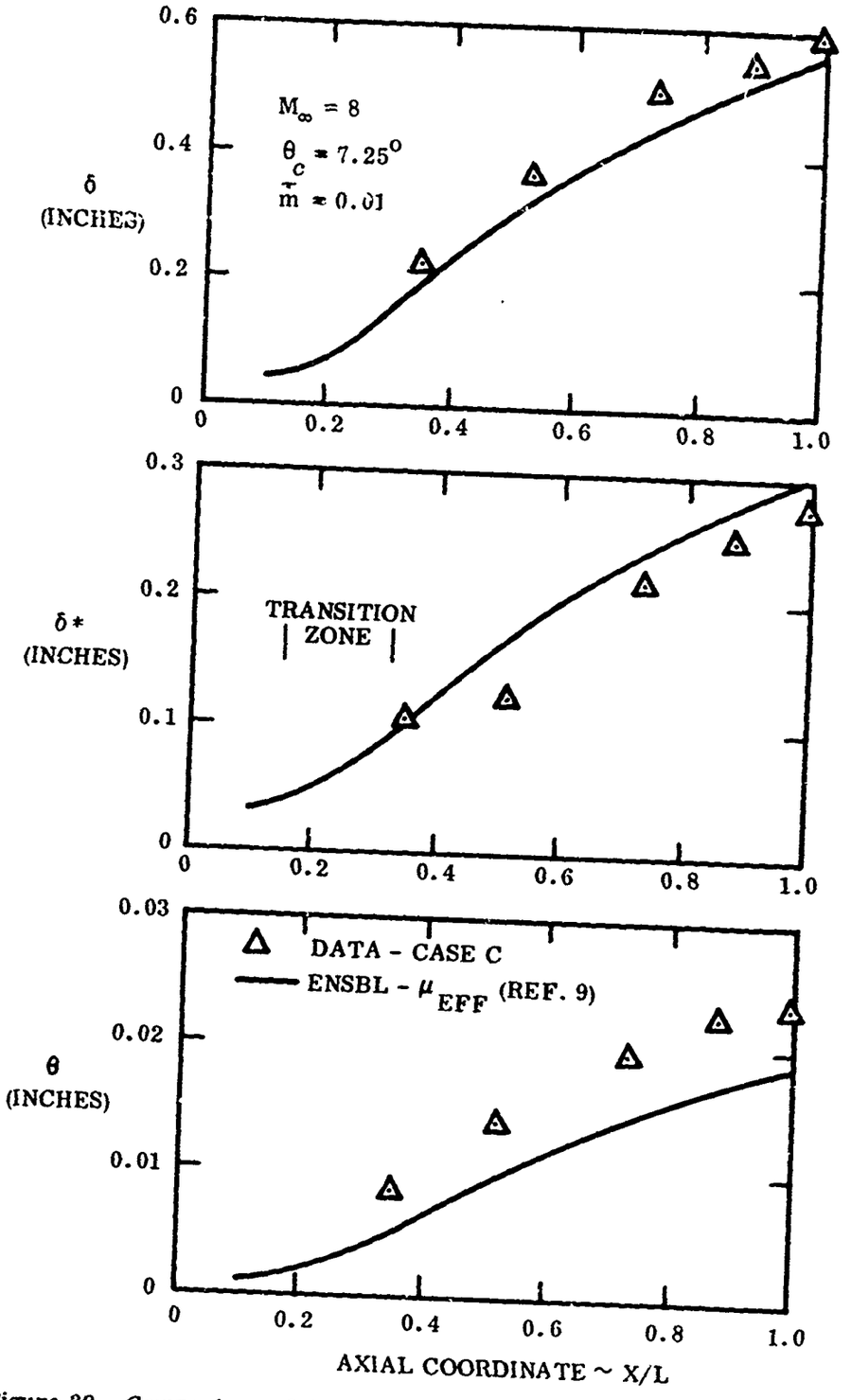

Figure 39. Comparison of ENSBL Program Results with Experimental Data

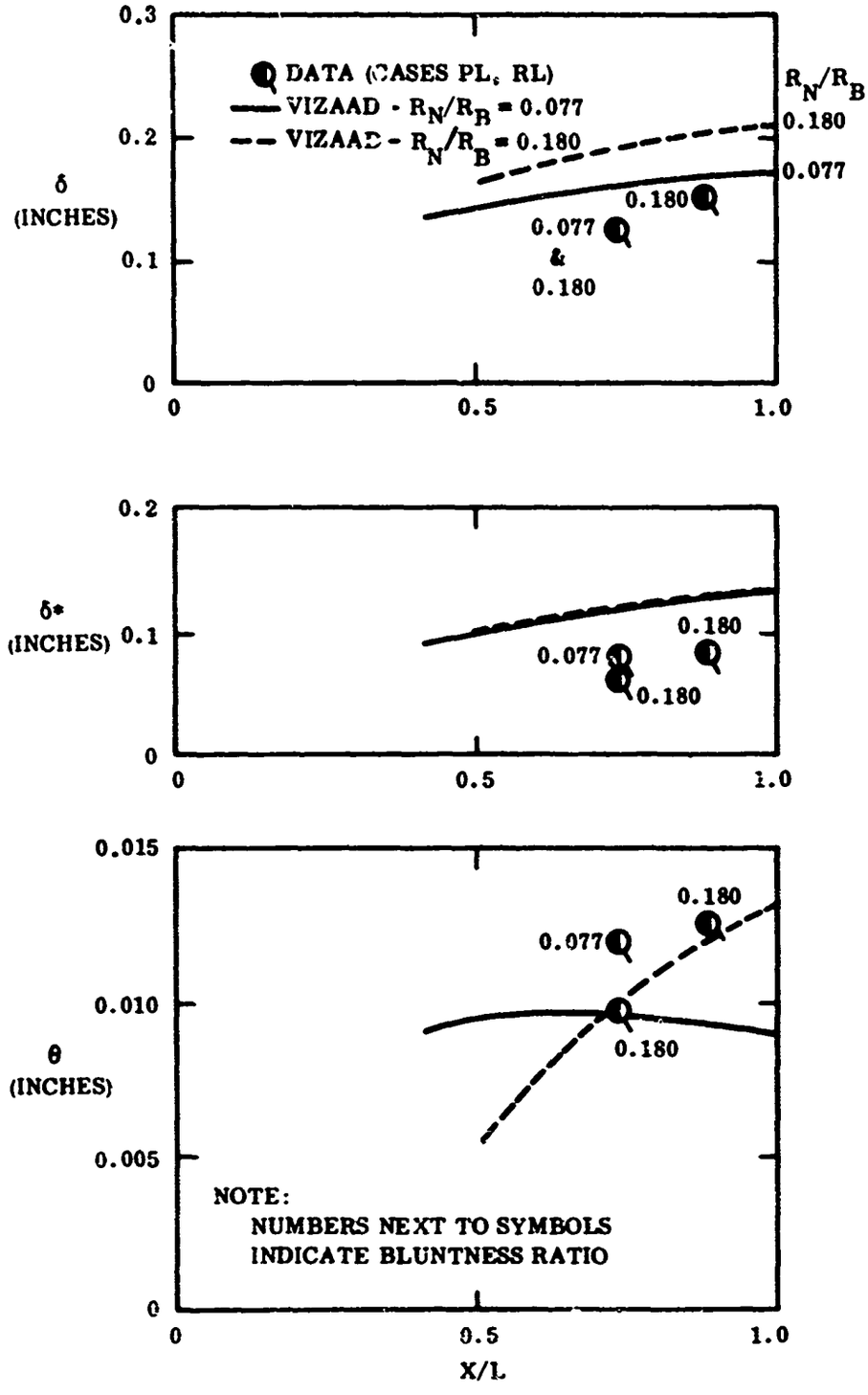

Figure 40. Comparison of Theory with Experimental Viscous Layer Thicknesses (Laminar)

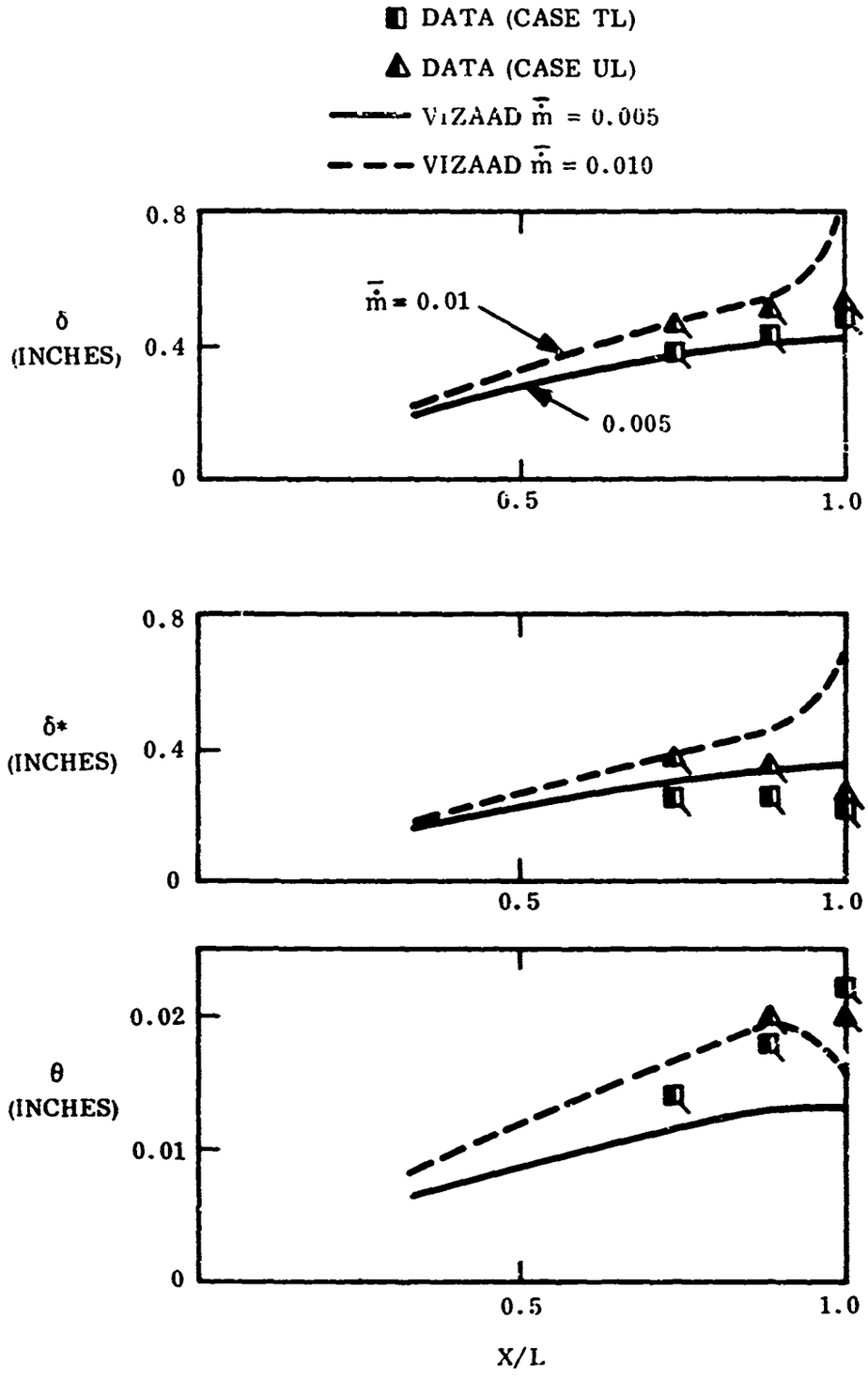

Figure 41. Comparison of Theory with Experimental Viscous Layer Thicknesses (Laminar)

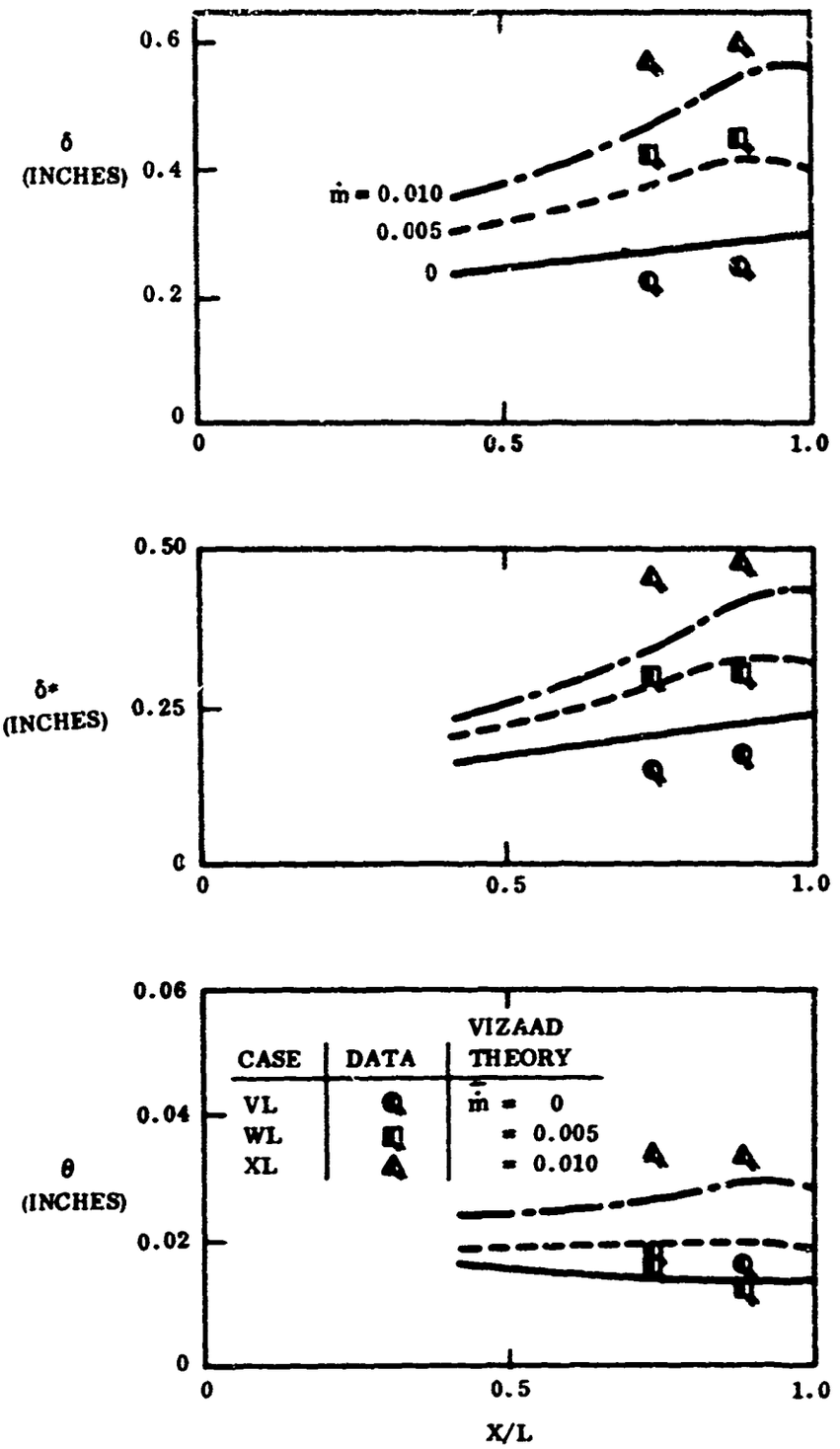

Figure 42. Comparison of Theory with Experimental Viscous Layer Thicknesses (Laminar)

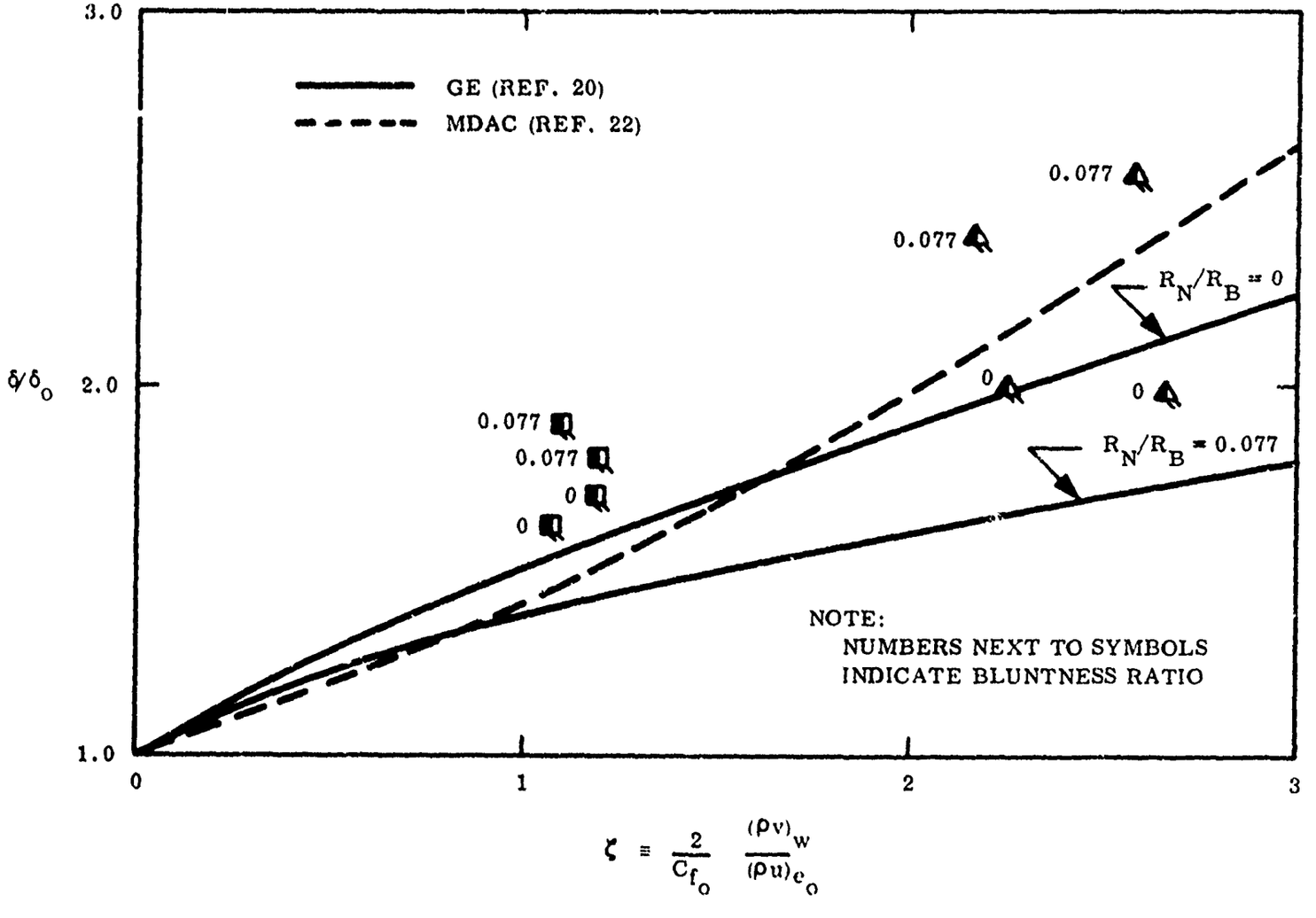

Figure 43. Effect of Mass Addition on Boundary Layer Thickness (Laminar)

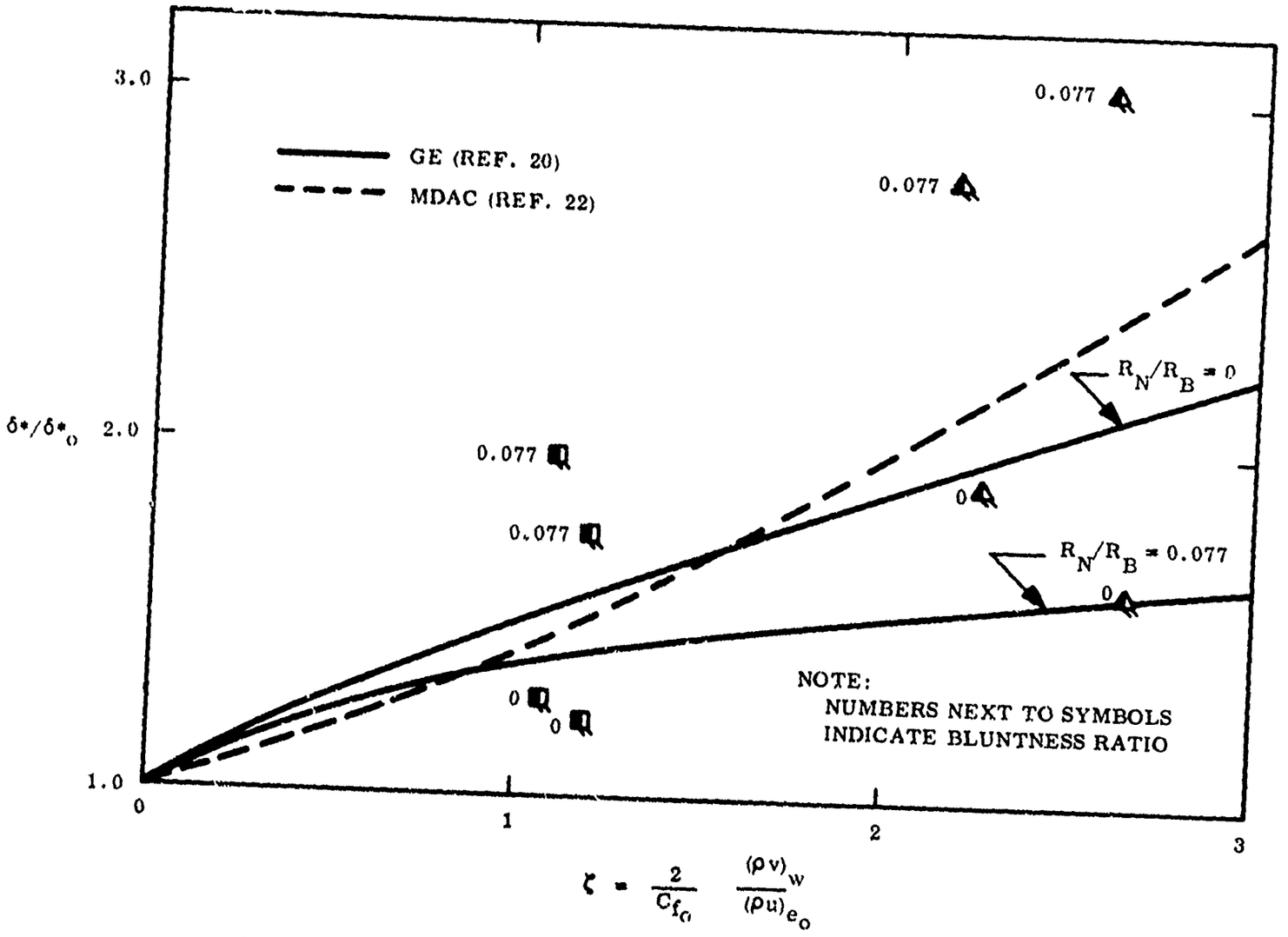

Figure 44. Effect of Mass Addition on Displacement Thickness (Laminar)

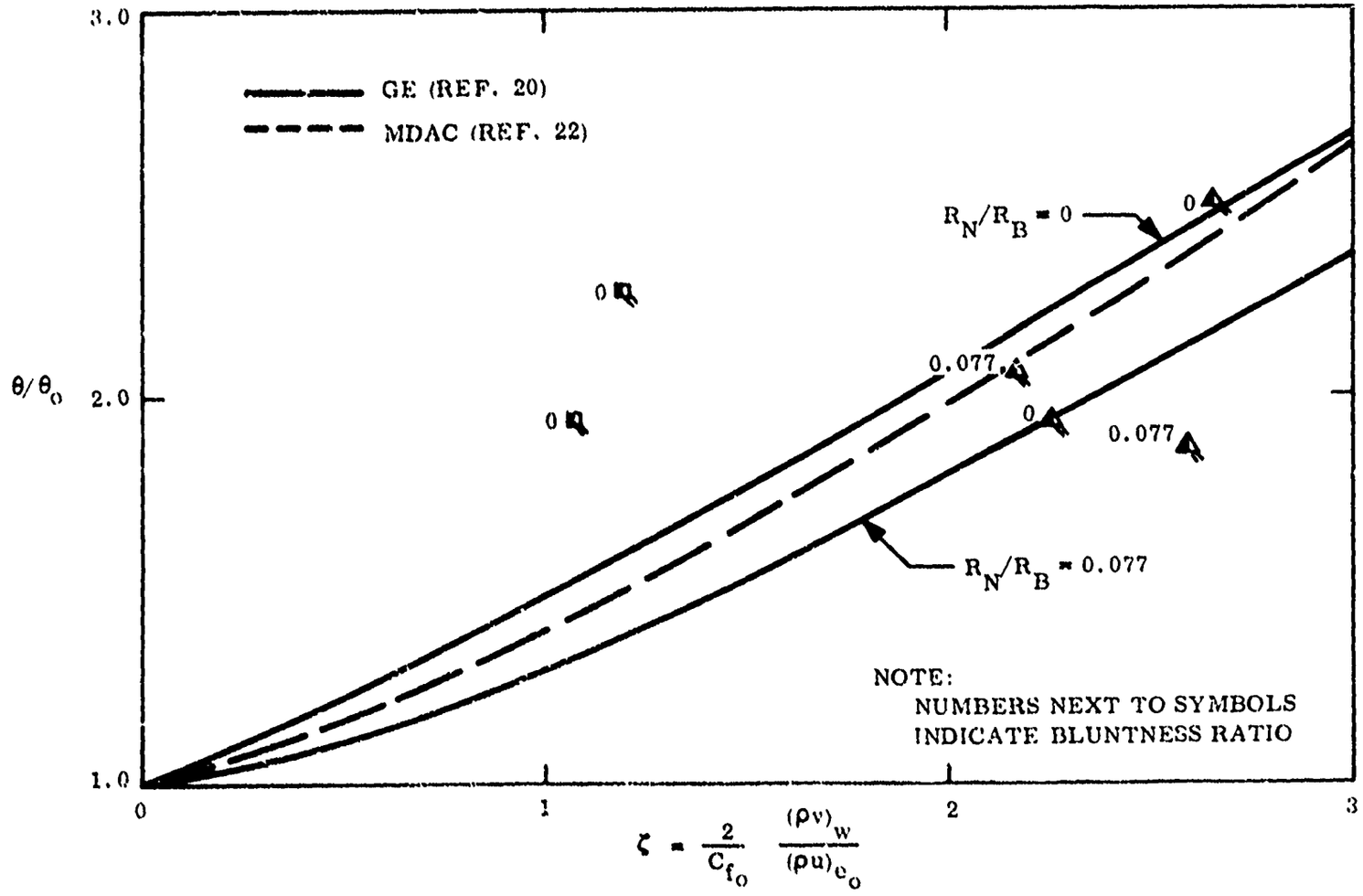

Figure 45. Effect of Mass Addition on Momentum Thickness (Laminar)

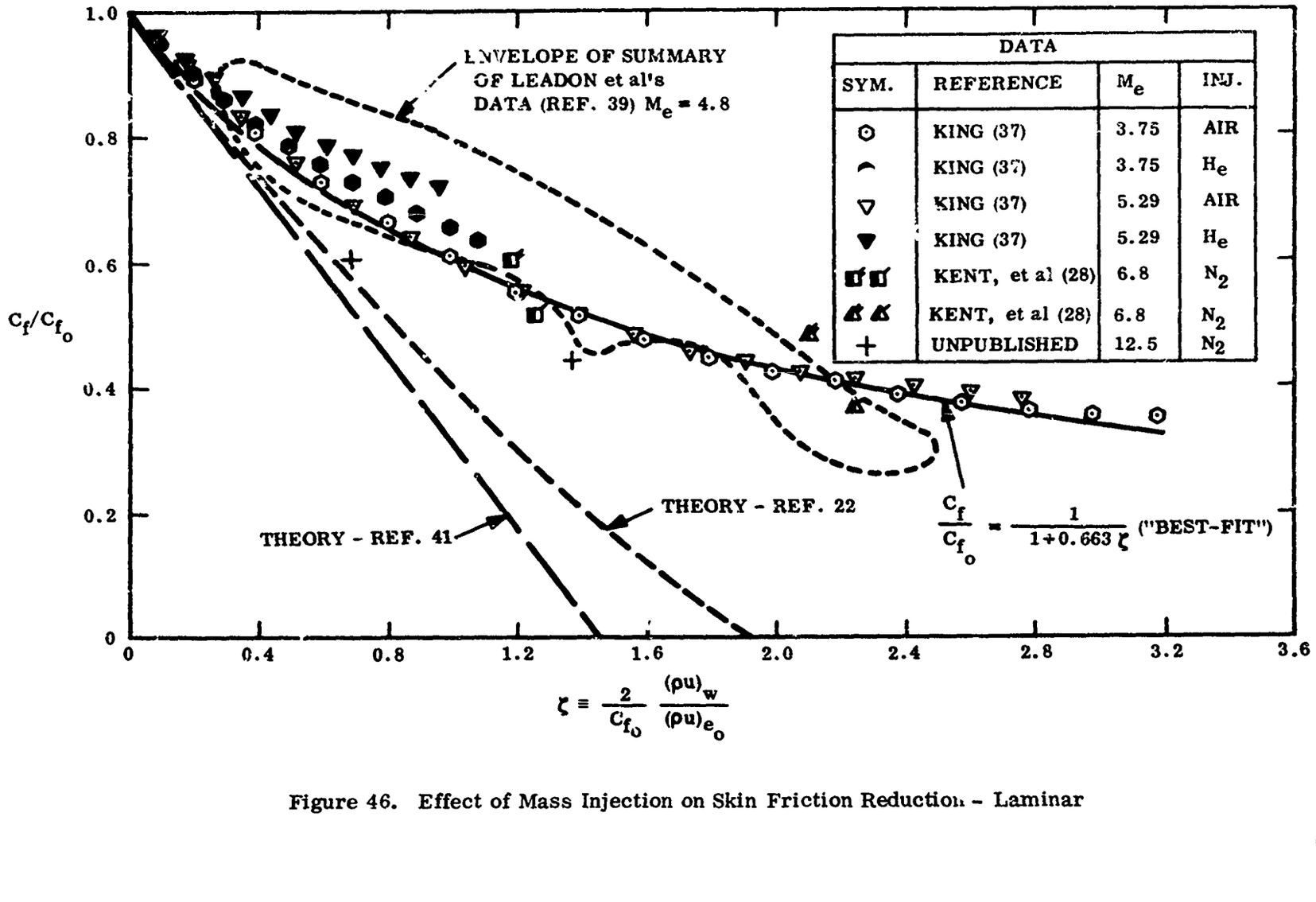

Figure 46. Effect of Mass Injection on Skin Friction Reduction – Laminar

APPENDIX A

TABULATED SUMMARY OF PROFILE DATA

BOUNDARY LAYER DATA DEDUCED FROM PROFILES

M_∞ = 8

θ_c = 7.25°

N_2 - Injectant

CASE A

	AXIAL STATION (INCHES)				
	14.61	21.61	30.61	36.61	41.51
$Re_s \times 10^{-6}$	6.63	9.24	13.3	16.0	18.2
$(\rho u)_{e_o}$ $\frac{LBM}{FT^2SEC}$	18.3	18.3	18.3	18.3	18.3
$(\rho v)_w$ $\frac{LBM}{FT^2SEC}$	0	0	0	0	0
$\lambda \equiv (\rho v)_w / (\rho u)_{e_o} \times 10^4$	0	0	0	0	0
C_{f_o}(THEOR.) $\times 10^3$	.9561	.8949	.8415	.8133	.7935
$\zeta = \frac{2\lambda}{C_{f_o}}$ (THEOR.)	0	0	0	0	0
δ_o (INCHES)	.173	.270	.368	.415	.455
δ_o^* (INCHES)	.0554	.0832	.148	.178	.194
θ_o (INCHES)	.00529	.00856	.0119	.0139	.0149
$H_o = \delta_o^* / \theta_c$	10.47	9.72	12.44	12.80	13.02
n_o (velocity profile exponent)	8.9	10.8	7.2	6.65	7.15
δ / δ_o					
δ^* / δ^*_o					
θ / θ_o					
H/H_o					
n/n_o					
T_w/Te_o	7.85	7.62	7.48	7.46	7.45
P_w/P_∞	2.80	3.00	2.80	2.86	2.81

BOUNDARY LAYER DATA DEDUCED FROM PROFILES

M_∞ = 8 CASE B

θ_c = 7.25°

N_2 - Injeccant

	AXIAL STATION (INCHES)				
	14.61	21.61	30.61	36.61	41.51
Re_s x 10^{-6}	6.63	9.24	13.3	16.0	18.2
$(\rho u)_{e_o}$ $\frac{LBM}{FT^2SEC}$	18.3	18.3	18.3	18.3	18.3
$(\rho v)_w$ $\frac{LBM}{FT^2SEC}$	.00612	.00612	.00612	.00612	.00612
$\lambda \equiv (\rho v)_w / (\rho u)_{e_o}$ x 10^4	3.344	3.344	3.344	3.344	3.344
Cf_o(THEOR.) x 10^3	.9561	.8949	.8415	.8133	.7935
$\zeta = \frac{2}{Cf_o}\lambda$ (THEOR.)	.700	.747	.795	.822	.843
δ (INCHES)	.216	.340	.440	.510	.515
δ^* (INCHES)	.0743	.112	.182	.223	.238
θ (INCHES)	.00701	.0112	.0156	.0183	.0191
$H = \delta^*/\theta$	10.60	10.00	11.67	12.19	12.46
n (velocity profile exponent)	9.25	7.65	6.15	5.75	6.60
δ / δ_o	1.25	1.26	1.195	1.23	1.132
δ^* / δ^*_o	1.341	1.346	1.230	1.253	1.227
θ / θ_o	1.325	1.308	1.311	1.317	1.282
H/H_o	1.014	1.03	.938	.952	.957
n/n_o	1.04	.708	.854	.865	.924
T_w/Te_o	7.44	7.12	6.85	6.75	6.73
P_w/P_∞	2.91	2.92	2.90	2.90	2.80

BOUNDARY LAYER DATA DEDUCED FROM PROFILES

M_∞ = 8

θ_c = 7.25°

N_2 - Injectant

CASE C

	AXIAL STATION (INCHES)				
	14.61	21.61	30.61	36.61	41.51
$Re_s \times 10^{-6}$	6.63	9.24	13.3	16.0	18.2
$(\rho u)_{e_o}$ $\frac{LBM}{FT^2SEC}$	18.3	18.3	18.3	18.3	18.3
$(\rho v)_w$ $\frac{LBM}{FT^2SEC}$	.01115	.01115	.01115	.01115	.01115
$\lambda \equiv (\rho v)_w / (\rho u)_{e_o} \times 10^4$	6.093	6.093	6.093	6.093	6.093
Cf_o(THEOR.) $\times 10^3$	.9561	.8949	.8415	.8133	.7935
$\zeta = \frac{2}{Cf_o}\lambda$ (THEOR.)	1.274	1.362	1.448	1.498	1.536
δ (INCHES)	.230	.378	.505	.558	.595
δ^* (INCHES)	.1085	.137	.218	.251	.277
θ (INCHES)	.00866	.0142	.0193	.0222	.0235
$H = \delta^*/\theta$	12.53	9.65	11.30	11.30	11.79
n (velocity profile exponent)	11.9	6.65	5.35	4.95	5.25
δ/δ_o	1.33	1.40	1.372	1.345	1.310
δ^*/δ^*_o	1.958	1.647	1.473	1.410	1.428
θ/θ_o	1.637	1.659	1.622	1.600	1.577
H/H_o	1.20	.993	.908	.883	.905
n/n_o	1.39	.615	.743	.745	.735
T_w/Te_o	7.02	6.70	6.42	6.31	6.27
P_w/P_∞	2.93	2.95	2.95	2.95	2.85

BOUNDARY LAYER DATA DEDUCED FROM PROFILES

M_∞ = 8

θ_c = 7.25°

N_2 - Injectant

CASE D

	AXIAL STATION (INCHES)				
	14.61	21.61	30.61	36.61	41.51
$Re_s \times 10^{-6}$	6.63	9.24	13.3	16.0	18.2
$(\rho u)_{e_o}$ $\frac{LBM}{FT^2SEC}$	18.3	18.3	18.3	18.3	18.3
$(\rho v)_w$ $\frac{LBM}{FT^2SEC}$	.0303	.0303	.0303	.0303	.0303
$\lambda \equiv (\rho v)_w / (\rho u)_{e_o} \times 10^4$	16.56	16.56	16.56	16.56	16.56
Cf_o(THEOR.) $\times 10^3$	.9561	.8949	.8415	.8133	.7935
$\zeta = \frac{2}{Cf_o}\lambda$ (THEOR.)	3.463	3.700	3.935	4.072	4.173
δ (INCHES)	-	-	.650	.775	.885
δ^* (INCHES)	-	-	.209	.365	.425
θ (INCHES)	-	-	.0219	.0355	.0393
$H = \delta^*/\theta$	-	-	9.54	10.28	10.8
n (velocity profile exponent)	-	..	4.05	3.6	4.1
δ/δ_o			1.766	1.87	1.945
δ^*/δ^*_o			1.412	2.051	2.190
θ/θ_o			1.840	2.554	2.640
H/H_o			.767	.803	.830
n/n_o			.563	.541	.573
T_w/Tc_o			5.12	5.01	4.96
P_w/P_∞			2.86	2.82	2.74

BOUNDARY LAYER DATA DEDUCED FROM PROFILES

M_∞ = 8

θ_c = 7.25°

N_2 - Injectant

CASE E

	AXIAL STATION (INCHES)				
	14.61	21.61	30.61	36.61	41.51
Re_s x 10^{-6}	6.63	9.24	13.3	16.0	18.2
$(\rho u)_{e_o}$ $\frac{LBM}{FT^2SEC}$	18.3	18.3	18.3	18.3	18.3
$(\rho v)_w$ $\frac{LBM}{FT^2SEC}$	.060	.060	.060	.060	.060
$\lambda \equiv (\rho v)_w / (\rho u)_{e_o}$ x 10^4	32.79	32.79	32.79	32.79	32.79
Cf_o(THEOR.) x 10^3	.9561	.8949	.8415	.8133	.7935
$\zeta = \frac{2}{C_{f_o}} \lambda$ (THEOR.)	6.858	7.327	7.792	8.063	8.264
δ (INCHES)	-	-	.925	1.175	1.32
δ^* (INCHES)	-	-	.535	.649	.737
θ (INCHES)	-	-	.0492	.0599	.0660
$H = \delta^*/\theta$	-	-	10.87	10.83	11.17
n (velocity profile exponent)	-	-	2.70	2.50	3.10
δ/δ_o			2.51	2.835	2.90
δ^*/δ_o^*			3.615	3.646	3.799
θ/θ_o			4.134	4.309	4.429
H/H_o			.874	.846	.858
n/n_o			.375	.376	.434
T_w/Te_o			4.04	3.99	3.94
P_w/P_∞			3.10	3.10	2.71

BOUNDARY LAYER DATA DEDUCED FROM PROFILES

M_∞ = 8

θ_c = 7.25°

N_2 - Injectant

CASE F

	AXIAL STATION (INCHES)				
	14.61	21.61	30.61	36.61	41.51
$Re_s \times 10^{-6}$		7.23	10.25	12.25	13.89
$(\rho u)_{e_o}$ $\frac{LBM}{FT^2SEC}$		13.21	13.21	13.21	13.21
$(\rho v)_w$ $\frac{LBM}{FT^2SEC}$		0	0	0	0
$\lambda \equiv (\rho u / (\rho u)_{e_o} \times 10^4$		0	0	0	0
Cf_o(THEOR.) $\times 10^3$		.9374	.8842	.8568	.8375
$\zeta = \frac{2}{Cf_o}\lambda$ (THEOR.)		0	0	0	0
δ_o (INCHES)		.208	.357	.393	.458
δ_o^* (INCHES)		.0698	.137	.158	.195
ϑ_o (INCHES)		.00593	.0112	.0131	.0153
$H_o = \delta_o^*/\theta_o$		11.77	12.23	12.06	12.74
n_o (velocity profile exponent)		6.7	7.9	7.2	7.0
δ / δ_o					
δ^* / δ_o^*					
θ / θ_o					
H/H_o					
n/n_o					
T_w/Te_o		7.93	7.72	7.65	7.61
P_w/P_∞		2.85	2.86	2.85	2.86

BOUNDARY LAYER DATA DEDUCED FROM PROFILES

M_∞ = 8

ϑ_c = 7.25°

N_2 - Injectant

CASE F α = -1° (Leeward)

	AXIAL STATION (INCHES)				
	14.61	21.61	30.61	36.61	41.51
Re_s x 10^{-6}					-
$(\rho u)_{e_o}$ $\frac{LBM}{FT^2SEC}$					-
$(\rho v)_w$ $\frac{LBM}{FT^2SEC}$					0
$\lambda \equiv (\rho v)_w / (\rho u)_{e_o}$ x 10^4					0
Cf_o(THEOR.) x 10^3					
$\zeta = \frac{2}{Cf_o}\lambda$ (THEOR.)					0
δ (INCHES)					.540
δ^* (INCHES)					.238
θ (INCHES)					.0196
$H = \delta^*/\theta$					12.12
n (velocity profile exponent)					7.1
$\delta/\delta_{\alpha=0}$					1.18
$\delta^*/\delta^*_{\alpha=0}$					1.22
$\theta/\theta_{\alpha=0}$					1.28
$H/H_{\alpha=0}$					0.950
$n/n_{\alpha=0}$					1.0
T_w/Te_o					.61
P_w/P_∞					2.60

BOUNDARY LAYER DATA DEDUCED FROM PROFILES

$M = 8$

$\theta_c = 7.25^\circ$

N_2 - Injectant

CASE F $\alpha = +1^\circ$ (Windward)

	AXIAL STATION (INCHES)				
	14.61	21.61	30.61	36.61	41.51
$Re_s \times 10^{-6}$					-
$(\rho u)_{e_o}$ $\frac{LBM}{FT^2SEC}$					-
$(\rho v)_w$ $\frac{LBM}{FT^2SEC}$					0
$\lambda \equiv (\rho v)_w / (\rho u)_{e_o} \times 10^4$					0
Cf_o(THEOR.) $\times 10^3$					-
$\zeta = \frac{2}{Cf_o}\lambda$ (THEOR.)					0
δ (INCHES)					.370
δ^* (INCHES)					.162
θ (INCHES)					.0137
$H = \delta^*/\theta$					11.78
n (velocity profile exponent)					7.0
$\delta / \delta_{\alpha=0}$					.809
$\delta^* / \delta^*_{\alpha=0}$					.830
$\theta / \theta_{\alpha=0}$					.895
$H/H_{\alpha=0}$					.923
$n/n_{\alpha=0}$					1.0
T_w/Te_o					7.61
P_w/P_∞					3.40

BOUNDARY LAYER DATA DEDUCED FROM PROFILES

M_∞ = 8

θ_c = 7.25°

N_2 - Injectant

CASE G

	AXIAL STATION (INCHES)				
	14.61	21.61	30.61	36.61	41.51
$Re_s \times 10^{-6}$		7.23	10.25	12.25	13.89
$(\rho u)_{e_o}$ $\frac{LBM}{FT^2SEC}$		13.21	13.21	13.21	13.21
$(\rho v)_w$ $\frac{LBM}{FT^2SEC}$		.00379	.00379	.00379	.00379
$\lambda \equiv (\rho v)_w / (\rho u)_{e_o} \times 10^4$		2.869	2.869	2.869	2.869
Cf_o(THEOR.) $\times 10^3$		-	.8842		.8375
$\zeta = \frac{2}{Cf_o}\lambda$ (THEOR.)			.649		.685
δ (INCHES)		-	.400	-	.505
δ^* (INCHES)		-	.169	-	.224
θ (INCHES)		-	.0140	-	.0186
$H = \delta^*/\theta$		-	12.05	-	12.04
n (velocity profile exponent)		-	6.9	-	7.3
δ / δ_o			1.12		1.105
δ^* / δ^*_o			1.233		1.149
θ / θ_o			1.250		1.216
H/H_o			.985		.945
n/n_o			.873		1.04
T_w/Te_o			7.33		7.24
P_w/P_∞			2.83		2.90

BOUNDARY LAYER DATA DEDUCED FROM PROFILES

M_∞ = 8 CASE H

θ_c = 7.25°

N_2 - Injectant

	AXIAL STATION (INCHES)				
	14.61	21.61	30.61	36.61	41.51
$Re_s \times 10^{-6}$		7.23	10.25	12.25	13.89
$(\rho u)_{e_o}$ $\frac{LBM}{FT^2SEC}$		13.21	13.21	13.21	13.21
$(\rho v)_w$ $\frac{LBM}{FT^2SEC}$		.00803	.00803	.00803	.00803
$\lambda \equiv (\rho v)_w / (\rho u)_{e_o} \times 10^4$		6.079	6.079	6.079	6.079
Cf_o(THEOR.) $\times 10^3$		.9374	.8842	.8568	.8375
$\zeta = \frac{2}{Cf_o}\lambda$ (THEOR.)		1.297	1.375	1.419	1.452
δ (INCHES)		.338	.500	.570	.658
δ^* (INCHES)		.128	.213	.245	.282
θ (INCHES)		.0118	.0175	.0211	.0243
$H = \delta^*/\theta$		10.85	12.17	11.61	11.60
n (velocity profile exponent)		6.4	7.1	6.2	6.45
δ / δ_o		1.425	1.40	1.45	1.445
δ^* / δ^*_o		1.834	1.555	1.551	1.446
θ / θ_o		1.990	1.563	1.611	1.588
H/H_o		.922	.945	.963	.910
n/n_o		.955	.898	.861	.921
T_w/Te_o		7.07	6.91	6.84	6.79
P_w/P_∞		2.90	2.80	2.84	2.68

BOUNDARY LAYER DATA DEDUCED FROM PROFILES

M_∞ = 8

θ_c = 7.25°

N_2 - Injectant

CASE J

	AXIAL STATION (INCHES)				
	14.61	21.61	30.61	36.61	41.51
Re_s x 10^{-6}		7.23	10.25	12.25	13.89
$(\rho u)_{e_o}$ $\frac{LBM}{FT^2SEC}$		13.21	13.21	13.21	13.21
$(\rho v)_w$ $\frac{LBM}{FT^2SEC}$		.02206	.02206	.02206	.02206
$\lambda \equiv (\rho v)_w / (\rho u)_{e_o}$ x 10^4		16.70	16.70	16.70	16.70
Cf_o(THEOR.) x 10^3		.9374	.8842	.8568	.8375
$\zeta = \frac{2}{Cf_o}\lambda$ (THEOR.)			3.777		3.988
δ (INCHES)		-	.735	-	.925
δ^* (INCHES)		-	.348	-	.476
θ (INCHES)		-	.0306	-	.0409
$H = \delta^*/\theta$		-	11.35	-	11.64
n (velocity profile exponent)		-	5.35	-	4.40
δ / δ_o			2.06		2.02
δ^* / δ^*_o			2.54		2.441
θ / θ_o			2.73		2.673
H/H_o			.928		.914
n/n_o			.677		.629
T_w/Te_o			5.71		5.66
P_w/P_∞			2.90		2.85

BOUNDARY LAYER DATA DEDUCED FROM PROFILES

M_∞ = 8

θ_c = 7.25°

N_2 - Injectant

CASE M

	AXIAL STATION (INCHES)				
	14.61	21.61	30.61	36.61	41.51
Re_s x 10^{-6}		7.23	10.25	12.25	13.89
$(\rho u)_{e_o}$ $\frac{LBM}{FT^2SEC}$		13.21	13.21	13.21	13.21
$(\rho v)_w$ $\frac{LBM}{FT^2SEC}$		.00422	.00422	.01265	.01265
$\lambda \cong (\rho v)_w / (\rho u)_{e_o}$ x 10^4		3.195	3.195	9.576	9.576
Cf_o(THEOR.) x 10^3		.9374	.8842	.8568	.8375
$\zeta = \frac{2}{Cf_o}\lambda$ (THEOR.)		.682	.723	2.235	2.287
δ (INCHES)		.290	.445	.505	.590
δ^* (INCHES)		.0943	.175	.232	.281
ϑ (INCHES)		.00978	.0153	.0199	.0237
$H = \delta^*/\theta$		9.64	11.44	11.66	11.86
n (velocity profile exponent)		6.8 7.15	7.10	4.95	5.30
δ / δ_o		1.395	1.245	1.285	1.29
δ^* / δ^*_o		1.350	1.277	1.468	1.441
θ / θ_o		1.650	1.366	1.519	1.549
H/H_o		.819	.935	.967	.931
n/n_o		1.015 1.067	.900	.688	.757
T_w/Te_o		7.47	7.30	6.37	6.33
P_w/P_∞		2.80	2.78	3.20	2.93

BOUNDARY LAYER DATA DEDUCED FROM PROFILES

M_∞ = 8

θ_c = 7.25°

N_2 - Injectant

CASE N

	AXIAL STATION (INCHES)				
	14.61	21.61	30.61	36.61	41.51
Re_s x 10^{-6}		7.23	10.25	12.25	13.89
$(\rho u)_{e_o}$ $\frac{LBM}{FT^2SEC}$		13.21	13.21	13.21	13.21
$(\rho v)_w$ $\frac{LBM}{FT^2SEC}$		.01158	.01158	.03474	.03474
$\lambda \equiv (\rho v)_w / (\rho u)_{e_o}$ x 10^4		8.766	8.766	26.30	26.30
Cf_o(THEOR.) x 10^3		.9374	.8842	.8568	.8375
$\zeta = \frac{2}{Cf_o}\lambda$ (THEOR.)			1.983		6.280
δ (INCHES)		-	.608	-	.925
δ^* (INCHES)		-	.240	-	.506
θ (INCHES)		-	.0227	-	.0398
$H = \delta^*/\theta$		-	10.57	-	12.71
n (velocity profile exponent)		-	6.4	-	3.15
δ / δ_o			1.705	-	2.02
δ^* / δ^*_o			1.752		2.595
θ / θ_o			2.027		2.601
H/H_o			.864		.998
n/n_o			.810		.450
T_w/Te_o			6.59		4.92
P_w/P_∞			2.75		3.25

BOUNDARY LAYER DATA DEDUCED FROM PROFILES

$M_\infty = 8$

$\theta_c = 7.25^\circ$

CO_2 - Injectant

CASE BB

	AXIAL STATION (INCHES)				
	14.61	21.61	30.61	36.61	41.51
$Re_s \times 10^{-6}$				16.0	
$(\rho u)_{e_o}$ $\frac{LBM}{FT^2SEC}$				18.3	
$(\rho v)_w$ $\frac{LBM}{FT^2SEC}$				.00771	
$\lambda \equiv (\rho v)_w / (\rho u)_{e_o} \times 10^4$				4.213	
Cf_o(THEOR.) $\times 10^3$				.8133	
$\zeta = \frac{2}{Cf_o} \lambda$ (THEOR.)				1.035	
δ (INCHES)				.525	
δ^* (INCHES)				.257	
θ (INCHES)				.0174	
$H = \delta^*/\theta$				14.76	
n (velocity profile exponent)				6.9	
δ / δ_o				1.265	
δ^* / δ^*_o				1.440	
θ / θ_o				1.250	
H/H_o				1.150	
n/n_o				1.04	
T_w/Te_o				6.73	
P_w/P_∞				2.54	

BOUNDARY LAYER DATA DEDUCED FROM PROFILES

M_∞ = 8

θ_c = 7.25°

N_2 - Injectant

CASE CC

	AXIAL STATION (INCHES)				
	14.61	21.61	30.61	36.61	41.51
Re_s x 10^{-6}				16.0	
$(\rho u)_{e_o}$ $\frac{LBM}{FT^2SEC}$				18.3	
$(\rho v)_w$ $\frac{LBM}{FT^2SEC}$				.01585	
$\lambda \equiv (\rho v)_w / (\rho u)_{e_o} \times 10^4$				8.661	
Cf_o(THEOR.) x 10^3				.8133	
$\zeta = \frac{2}{Cf_o} \lambda$ (THEOR.)				2.13	
δ (INCHES)				.550	
δ^* (INCHES)				.277	
θ (INCHES)				.0216	
$H = \delta^*/\theta$				12.81	
n (velocity profile exponent)				5.35	
δ / δ_o				1.325	
δ^* / δ^*_o				1.555	
θ / θ_o				1.555	
H/H_o				1.00	
n/n_o				.805	
T_w/Te_o				6.02	
P_w/P_∞				2.68	

BOUNDARY LAYER DATA DEDUCED FROM PROFILES

M_∞ = 8

θ_c = 7.25°

CO_2 - Injectant

CASE EE

	AXIAL STATION (INCHES)				
	14.61	21.61	30.61	36.61	41.51
Re_s x 10^{-6}				16.0	
$(\rho u)_{e_o}$ $\frac{LBM}{FT^2SEC}$				18.3	
$(\rho v)_w$ $\frac{LBM}{FT^2SEC}$				.0708	
$\lambda \equiv (\rho v)_w / (\rho u)_{e_o} \times 10^4$				38.67	
Cf_o(THEOR.) x 10^3				.8133	
$\zeta = \frac{2}{Cf_o} \lambda$ (THEOR.)				9.52	
δ (INCHES)				1.150	
δ^* (INCHES)				.673	
θ (INCHES)				.0587	
$H = \delta^*/\theta$				11.45	
n (velocity profile exponent)				2.35	
δ / δ_o				2.79	
δ^* / δ^*_o				3.70	
θ / θ_o				4.22	
H/H_o				.894	
n/n_o				..354	
T_w/Te_o				3.85	
P_w/P_∞				3.22	

BOUNDARY LAYER DATA DEDUCED FROM PROFILES

$M_\infty = 8$

$\theta_c = 7.25°$

N_2 - Injectant

CASE FF

	AXIAL STATION (INCHES)				
	14.61	21.61	30.61	36.61	41.51
$Re_\delta \times 10^{-6}$			10.25	12.25	13.89
$(\rho u)_{e_o}$ $\frac{LBM}{FT^2SEC}$			13.21	13.21	13.21
$(\rho v)_w$ $\frac{LBM}{FT^2SEC}$			0	0	0
$\lambda \equiv (\rho v)_w / (\rho u)_{e_o} \times 10^4$			0	0	0
Cf_o(THEOR.) $\times 10^3$			.8842	.8568	.8375
$\zeta = \frac{2}{Cf_o}\lambda$ (THEOR.)			0	0	0
δ (INCHES)			.325	.370	.425
δ^* (INCHES)			.124	.164	.197
θ (INCHES)			.00689	.00937	.0137
$H = \delta^*/\theta$			18.02	17.53	14.35
n (velocity profile exponent)			11.2	8.2	7.9
δ/δ_o					
δ^*/δ^*_o					
θ/θ_o					
H/H_o					
n/n_o					
T_w/Te_o			7.65	7.60	7.63
P_w/P_∞			2.84	2.77	2.82

BOUNDARY LAYER DATA DEDUCED FROM PROFILES

M_∞ = 8

θ_c = 7.25°

N_2 - Injectant

CASE GG

	AXIAL STATION (INCHES)				
	14.61	21.61	30.61	36.61	41.51
$Re_s \times 10^{-6}$				11.98	13.58
$(\rho u)_{e_o}$ LBM/FT²SEC				12.92	12.92
$(\rho v)_w$ LBM/FT²SEC				.00614	.00595
$\lambda \equiv (\rho v)_w / (\rho u)_{e_o} \times 10^4$				4.752	0
C_{f_o}(THEOR.) $\times 10^3$				.8568	.8375
$\zeta = \frac{2}{C_{f_o}} \lambda$ (THEOR.)				1.110	0
δ (INCHES)				.510	.550
δ^* (INCHES)				-	.133
θ (INCHES)				-	.0120
$H = \delta^*/\theta$				-	11.07
n (velocity profile exponent)				-	6.8
δ/δ_o				-	1.200
δ^*/δ^*_o					
θ/θ_o					
H/H_o					
n/n_o					
T_w/Te_o				7.08	7.03
P_w/P_∞				2.71	2.61

BOUNDARY LAYER DATA DEDUCED FROM PROFILES

M_∞ = 8

θ_c = 7.25°

N_2 - Injectant

CASE KK

	AXIAL STATION (INCHES)				
	14.61	21.61	30.61	36.61	41.51
$Re_s \times 10^{-6}$				12.25	
$(\rho u)_{e_o}$ $\frac{LBM}{FT^2SEC}$				13.21	
$(\rho v)_w$ $\frac{LBM}{FT^2SEC}$				.0519	
$\lambda \equiv (\rho v)_w / (\rho u)_{e_o} \times 10^4$				39.29	
Cf_o(THEOR.) $\times 10^3$				.8568	
$\zeta = \frac{2}{Cf_o} \lambda$ (THEOR.)				9.18	
δ (INCHES)				1.10	
δ^* (INCHES)				.624	
θ (INCHES)				.0638	
$H = \delta^*/\theta$				9.781	
n (velocity profile exponent)				2.05	
δ / δ_o				2.80	
δ^* / δ^*_o				3.95	
θ / θ_o				4.87	
H/H_o				.811	
n/n_o				.285	
T_w/Te_o				4.45	
P_w/P_∞				3.20	

BOUNDARY LAYER DATA DEDUCED FROM PROFILES

M_∞ = 8

θ_c = 7.25°

N_2 - Injectant

CASE PL

	AXIAL STATION (INCHES)				
	14.61	21.61	30.61	36.61	41.51
Re_s x 10^{-6}			1.684	2.645	
$(\rho u)_{e_o}$ $\frac{LBM}{FT^2SEC}$			5.24	6.07	
$(\rho v)_w$ $\frac{LBM}{FT^2SEC}$			0	0	
$\lambda \equiv (\rho v)_w / (\rho u)_{e_o} \times 10^4$			0	0	
Cf_o(THEOR.) x 10^3			.831	.664	
$\zeta = \frac{2}{Cf_o}\lambda$ (THEOR.)			0	0	
δ (INCHES)			.125	.150	
δ^* (INCHES)			.0789	.0199	
θ (INCHES)			.0119	.00254	
$H = \delta^*/\theta$			6.611	7.827	
n (velocity profile exponent)			—	—	
δ/δ_o					
δ^*/δ^*_o					
θ/θ_o					
H/H_o					
n/n_o					
T_w/Te_o			9.39	8.88	
P_w/P_∞			2.62	2.68	

BOUNDARY LAYER DATA DEDUCED FROM PROFILES

M_∞ = 8

θ_c = 7.25°

N_2 - Injectant

CASE 9L

	AXIAL STATION (INCHES)				
	14.61	21.61	30.61	36.61	41.51
Re_δ x 10^{-6}				2.645	
$(\rho u)_{e_o}$ $\frac{LBM}{FT^2SEC}$				6.07	
$(\rho v)_w$ $\frac{LBM}{FT^2SEC}$				.0584	
$\lambda \equiv (\rho v)_w / (\rho u)_{e_o} \times 10^4$				96.2	
Cf_o(THEOR.) x 10^3				.664	
$\zeta = \frac{2}{Cf_o}\lambda$ (THEOR.)				28.98	
δ (INCHES)				1.250	
δ^* (INCHES)				.893	
θ (INCHES)				.0512	
$H = \delta^*/\theta$				17.45	
n (velocity profile exponent)				-	
δ / δ_o				8.34	
δ^* / δ^*_o				44.0	
θ / θ_o				19.7	
H/H_o				2.235	
n/n_o				-	
T_w/Te_o				5.51	
P_w/P_∞				3.20	

BOUNDARY LAYER DATA DEDUCED FROM PROFILES

M_∞ = 8

θ_c = 7.25°

N_2 - Injectant

CASE RL

	AXIAL STATION (INCHES)				
	14.61	21.61	30.61	36.61	41.51
Re_δ x 10^{-6}			.576	.798	
$(\rho u)_{e_o}$ $\frac{LBM}{FT^2SEC}$			2.835	3.093	
$(\rho v)_w$ $\frac{LBM}{FT^2SEC}$			0	0	
$\lambda \equiv (\rho v)_w / (\rho u)_{e_o} \times 10^4$			0	0	
Cf_o(THEOR.) x 10^3			1.318	1.169	
$\zeta = \frac{2}{Cf_o}\lambda$ (THEOR.)			0	0	
δ (INCHES)			.125	.150	
δ^* (INCHES)			.0580	.0821	
θ (INCHES)			.00966	.0125	
$H = \delta^*/\theta$			6.01	6.55	
n (velocity profile exponent)			—	—	
δ/δ_o					
δ^*/δ^*_o					
θ/θ_o					
μ/μ_o					
n/n_o					
T_w/Te_o			7.86	7.65	
P_w/P_∞			2.22	2.32	

BOUNDARY LAYER DATA DEDUCED FROM PROFILES

$M_\infty = 8$

$\theta_c = 7.25^\circ$

N_2 - Injectant

CASE SL

	AXIAL STATION (INCHES)				
	14.61	21.61	30.61	36.61	41.51
$Re_s \times 10^{-6}$				.798	
$(\rho u)_{e_o}$ $\frac{LBM}{FT^2SEC}$				3.093	
$(\rho v)_w$ $\frac{LBM}{FT^2SEC}$				.0573	
$\lambda \equiv (\rho v)_w / (\rho u)_{e_o} \times 10^4$				185.3	
Cf_o(THEOR.) $\times 10^3$				1.169	
$\zeta = \frac{2}{Cf_o}\lambda$ (THEOR.)				31.7	
δ (INCHES)				1.550	
δ^* (INCHES)				1.028	
θ (INCHES)				.0991	
$H = \delta^*/\theta$				10.37	
n (velocity profile exponent)				-	
δ / δ_o				10.33	
δ^* / δ^*_o				12.52	
θ / θ_o				7.93	
H/H_o				1.58	
n/n_o				-	
T_w/Te_o				5.51	
P_w/P_∞				2.94	

BOUNDARY LAYER DATA DEDUCED FROM PROFILES

M_∞ = 8

θ_c = 7.25°

N_2 - Injectant

CASE TL

	AXIAL STATION (INCHES)				
	14.61	21.61	30.61	36.61	41.51
Re_δ x 10^{-6}			2.619	3.217	3.55
$(\rho u)_{e_o}$ $\frac{LBM}{FT^2SEC}$			3.056	3.056	3.056
$(\rho v)_w$ $\frac{LBM}{FT^2SEC}$			.00116	.00118	0
$\lambda \equiv (\rho v)_w / (\rho u)_{e_o}$ x 10^4			3.796	3.861	0
Cf_o(THEOR.) x 10^3			.711	.650	.610
$\zeta = \frac{2}{Cf_o}\lambda$ (THEOR.)			1.068	1.188	0
δ (INCHES)			.375	.430	.488
δ^* (INCHES)			.249	.259	.210
θ (INCHES)			.0141	.0180	.0221
$H = \delta^*/\theta$			17.63	14.40	9.46
n (velocity profile exponent)			-	-	-
δ/δ_o			1.62	1.70	1.82
δ^*/δ^*_o			1.28	1.22	.928
θ/θ_o			1.94	2.27	2.62
H/H_o			.657	.537	.353
n/n_o			-	-	-
T_w/Te_o			7.14	7.65	7.14
P_w/P_∞			2.68	2.58	2.51

BOUNDARY LAYER DATA DEDUCED FROM PROFILES

M_∞ = 8

θ_c = 7.25°

N_2 - Injectant

CASE UL

	AXIAL STATION (INCHES)				
	14.61	21.61	30.61	36.61	41.51
Re_s x 10^{-6}			2.619	3.217	3.55
$(\rho u)_{e_o}$ $\frac{LBM}{FT^2SEC}$			3.056	3.056	3.056
$(\rho v)_w$ $\frac{LBM}{FT^2SEC}$			.00245	.00264	0
$\lambda \equiv (\rho v)_w / (\rho u)_{e_o} \times 10^4$			8.017	8.639	0
Cf_o(THEOR.) x 10^3			.711	.650	.610
$\zeta = \frac{2}{Cf_o}\lambda$ (THEOR.)			2.255	2.658	0
δ (INCHES)			.460	.500	.525
δ^* (INCHES)			.371	.342	.264
θ (INCHES)			.0141	.0198	.0198
$H = \delta^*/\theta$			26.41	17.27	13.35
n (velocity profile exponent)			-	-	-
δ / δ_o			1.99	1.98	1.95
δ^* / δ^*_o			1.90	1.61	1.17
θ / θ_o			1.94	2.50	2.35
H/H_o			.984	.644	.498
n/n_o			-	-	-
T_w/Te_o			5.20	7.35	7.14
P_w/P_∞			2.91	2.77	2.53

BOUNDARY LAYER DATA DEDUCED FROM PROFILES

M_∞ = 8

θ_c = 7.25°

N_2 - Injectant

CASE VL

	AXIAL STATION (INCHES)				
	14.61	21.61	30.61	36.61	41.51
Re_s x 10^{-6}			.842	1.277	
$(\rho u)_{e_o}$ $\frac{LBM}{FT^2SEC}$			1.668	1.952	
$(\rho v)_w$ $\frac{LBM}{FT^2SEC}$			0	0	
$\lambda \equiv (\rho v)_w / (\rho u)_{e_o} \times 10^4$			0	0	
Cf_o(THEOR.) x 10^3			1.221	.994	
$\zeta = \frac{2}{Cf_o}\lambda$ (THEOR.)			0	0	
δ (INCHES)			.225	.250	
δ^* (INCHES)			.150	.172	
θ (INCHES)			.0183	.0163	
$H = \delta^*/\theta$			8.20	10.59	
n (velocity profile exponent)			-	-	
δ / δ_o					
δ^* / δ^*_o					
θ / θ_o					
H/H_o					
n/n_o					
T_w/Te_o			6.94	6.94	
P_w/P_∞			2.80	2.59	

BOUNDARY LAYER DATA DEDUCED FROM PROFILES

M_∞ = 8

θ_c = 7.25°

N_2 - Injectant

CASE WL

	AXIAL STATION (INCHES)				
	14.61	21.61	30.61	36.61	41.51
$Re_s \times 10^{-6}$			.842	1.277	
$(\rho u)_{e_o}$ $\frac{LBM}{FT^2SEC}$			1.668	1.952	
$(\rho v)_w$ $\frac{LBM}{FT^2SEC}$			.00112	.00116	
$\lambda \equiv (\rho v)_w / (\rho u)_{e_o} \times 10^4$			6.715	5.943	
Cf_o(THEOR.) $\times 10^3$			1.221	.994	
$\zeta = \frac{2}{Cf_o} \lambda$ (THEOR.)			1.100	1.196	
δ (INCHES)			.425	.450	
δ^* (INCHES)			.295	.301	
θ (INCHES)			.0163	.0124	
$H = \delta^*/\theta$			18.04	24.22	
n (velocity profile exponent)			-	-	
δ / δ_o			1.89	1.80	
δ^* / δ^*_o			1.97	1.75	
ϑ / θ_o			.891	.761	
H/H_o			2.20	2.29	
n/n_o			-	-	
T_w/Te_o			6.22	6.22	
P_w/P_∞			2.48	2.44	

BOUNDARY LAYER DATA DEDUCED FROM PROFILES

M_∞ = 8

θ_c = 7.25°

N_2 - Injectant

CASE XL

	AXIAL STATION (INCHES)				
	14.61	21.61	30.61	36.61	41.51
$Re_s \times 10^{-6}$			.842	1.277	
$(\rho u)_{e_o}$ LBM/FT²SEC			1.668	1.952	
$(\rho v)_w$ LBM/FT²SEC			.00263	.00210	
$\lambda \equiv (\rho v)_w / (\rho u)_{e_o} \times 10^4$			15.77	10.76	
Cf_o(THEOR.) $\times 10^3$			1.221	.994	
$\zeta = \frac{2}{Cf_o}\lambda$ (THEOR.)			2.583	2.165	
δ (INCHES)			.575	.600	
δ^* (INCHES)			.455	.476	
θ (INCHES)			.0342	.0336	
$H = \delta^*/\theta$			13.31	14.15	
n (velocity profile exponent)			-	-	
δ / δ_o			2.56	2.40	
δ^* / δ^*_o			3.03	2.77	
θ / θ_o			1.87	2.06	
H/H_o			1.62	1.34	
n/n_o			-	-	
T_w/Te_o			5.10	4.90	
P_w/P_∞			2.81	2.48	

BOUNDARY LAYER DATA DEDUCED FROM PROFILES

M_∞ = 8

θ_c = 7.25°

N_2 - Injectant

CASE –

$\dot{m}$ = 0 Case Corresponding to UL, TL (VIZAAD)

	AXIAL STATION (INCHES)				
	14.61	21.61	30.61	36.61	41.51
$Re_s \times 10^{-6}$			2.66	3.16	3.60
$(\rho u)_{e_o}$ $\frac{LBM}{FT^2SEC}$			3.115	3.105	3.105
$(\rho v)_w$ $\frac{LBM}{FT^2SEC}$			0	0	0
$\lambda \equiv (\rho v)_w / (\rho u)_{e_o} \times 10^4$			0	0	0
Cf_o(THEOR.) $\times 10^3$			.701	.644	.604
$\zeta = \frac{2}{Cf_o}\lambda$ (THEOR.)			0	0	0
δ (INCHES)			.231	.252	.269
δ^* (INCHES)			.195	.212	.226
θ (INCHES)			.00726	.00792	.00844
$H = \delta^*/\theta$			26.84	26.83	26.82
n (velocity profile exponent)			-	-	-
δ / δ_o					
δ^* / δ^*_o					
θ / θ_o					
H/H_o					
n/n_o					
T_w/Te_o			7.28	7.28	7.28
P_w/P_∞					